Laser-Assisted Dynamics on Metallic Surfaces using Ultrafast X-Rays

by

Luis Miaja Avila

B.S., Tecnológico de Monterrey, 2002

A thesis submitted to the

Faculty of the Graduate School of the

University of Colorado in partial fulfillment

of the requirements for the degree of

Doctor of Philosophy

Department of Physics

2009

This thesis entitled:
Laser-Assisted Dynamics on Metallic Surfaces using Ultrafast X-Rays
written by Luis Miaja Avila
has been approved for the Department of Physics

Prof. Henry C. Kapteyn

Prof. Margaret M. Murnane

Date

The final copy of this thesis has been examined by the signatories, and we find that both the content and the form meet acceptable presentation standards of scholarly work in the above mentioned discipline.

Miaja Avila, Luis (Ph.D., Physics)

Laser-Assisted Dynamics on Metallic Surfaces using Ultrafast X-Rays

Thesis directed by Prof. Margaret M. Murnane and Prof. Henry C. Kapteyn

Time-resolved photoelectron spectroscopy is a powerful technique for the study of real-time electron dynamics on metallic surfaces. These studies are performed in pump-probe geometries, where a pump pulse excites a dynamic process and a time-delayed probe monitors changes in the system. Furthermore, recent progress in ultrafast lasers and high-harmonic generation has opened up a new area of surface science, where these two light sources are the standard tools for the study of ultrafast surface dynamics. Another critical discovery that has made it possible to study high-energy and femtosecond time-scale atomic dynamics is the laser-assisted photoelectric effect. However, until 2005 this effect had only been observed in gas-phase atomic systems, limiting its applicability to the study of isolated atoms or molecules.

Using time-resolved photoelectron spectroscopy, this thesis presents work demonstrating that the physics of the laser-assisted photoelectric effect can be expanded to solid-state systems. This result represents the laser-assisted version of the original manifestation of the photoelectric effect. This thesis also presents experimental data showing that laser-assisted photoemission from surfaces can be distinguished from other laser-surface interaction phenomena, such as hot electron excitation, above-threshold photoemission, and space-charge acceleration.

Additionally, by using surface laser-assisted photoemission and laser-assisted Auger decay, a direct measurement of the lifetime of core-excited states of an atom adsorbed onto a surface is presented. Finally, this research demonstrates that using a dressing laser at longer wavelengths dramatically reduces above-threshold photoemission and space-charge effects while enhancing the surface laser-assisted photoemission signal.

Dedication

Para mi amá y mi apá.

Para mi mejor amiga y esposa Tamra.

Acknowledgements

During the last six and a half years I've had the fortune to work with so many wonderful people to whom I'll be always grateful. First of all I would like to thank my advisors, Henry Kapteyn and Margaret Murnane. Their guidance and support were fundamental for the development of this work. It has been my honor to work for them. It has also been a pleasure to work and learn from Martin Aeschlimann, my third advisor and life coach. His support and passion for science sparked my interest in surface science. I also give my acknowledgment to John Gland, another great advisor and friend to whom I owe all the chemistry I know, and Michael Bauer, a great scientist I wish I had worked with more closely. Also, I would like to thank Dan Dessau and Jim and Lorrie Shepard for their friendship, support, and encouragement to come to Boulder for grad school.

I would also like to thank the two amazing post-docs with whom I worked, Tim Lei and Guido Saathoff. Thanks to Tim for introducing me to surface science, for teaching me how to run the experiments, and for always being patient with me. Thanks to Guido for showing me that patience and optimism are fundamental to make things happen, and for all his help and suggestions to get these experiments to work. I will always be amazed with his incredible understanding of science.

I would also like to acknowledge Ra'anan Tobey, Dave Gaudiosi, Ariel Paul and Amy Lytle, four great grad students and friends from whom I've learned a lot. Stefan Mathias is another great friend and coworker who helped me get these experiments

running. I want to thank all the KM group members who made the lab a fun place to work: Mark Siemens, Richard Sandberg, Jing Yin, Mike Grisham, Etienne Gagnon, Erez Gershgoren, Steffen Hädrich, Jim Holtsnider, Daisy Raymondson, Chan La-o-vorakiat, Arvinder Sandhu, Xibin Zhou, Robynne Lock, Oren Cohen, Nick Wagner, Andrea Wüest, Scott Hoch, Rachael and Matt Tearle, Tenio Popmintchev, Alon Bahabad, Qing Li, Paul Arpin, Mike Gerrity, Ethan Townsend, Matt Seaberg, Craig Hogle, Kim Reid. From KM Labs I would like to acknowledge: Sterling Backus, Hsiao-hua Liu, Neil Anderson, Dirk Mueller, and Kendall Read. I also want to thank other friends from JILA: my best friend Manuel Castellanos Beltrán, Javier von Stecher, Nathan Flowers-Jacobs, Konrad Lehnert, and many others I may have forgotten.

And of course I must acknowledge the fantastic staff at JILA: Todd Asnicar, Hans Green, Blaine Horner, Tom Foote, Kim Hagen, Tracy Keep, James Fung-A-Fat, Dave Alchenberger, Leslie Czaia, Pam Leland, Lisa Roos, Randall Holliness, Brian and Agnes Lynch, Dave Erickson, Jeff Sauter, Mike Paige, J. R. Raith, Ed Holliness, Joel Frahm, Jim McKown, Carl Sauer, David Tegart, Julie Phillips, Lynn Hogan, Sam Jarvis, Andy Hytjan, Doug Hogoboom, Peter Ruprecht, Corinne Hammond.

Finally I would like to pay the greatest tribute to my family. To my parents and siblings for being a great source of motivation and inspiration. And to my wife Tamra for her smile, love, and eternal support.

Contents

Chapter

Figures

Figure

Chapter 1

Introduction

An important motivation for the study of surfaces is the fundamental understanding of heterogeneous catalysis. The idea that the presence of a solid could accelerate a chemical reaction without modifying the solid was what triggered the development of the field of surface science. Since then, the goal of surface science has been to build an understanding of electronic, atomic and molecular dynamics on surfaces. Over the years, different experimental techniques have been developed to better explore the interaction between adsorbates (atoms or molecules) and surfaces. These techniques include low-energy electron diffraction (LEED), used for the determination of surface structure; inverse photoemission spectroscopy (IPS), which studies the unoccupied electronic structure of surfaces, thin films, and adsorbates; Auger electron spectroscopy (AES), used for the characterization of surface adsorbates; and ultraviolet and x-ray photoelectron spectroscopies (UPS and XPS, respectively), which measure the elemental composition and electronic state of the solid. These last two techniques have been extensively applied in surface science because of their excellent surface sensitivity. Surface sensitivity in UPS and XPS arises from the idea that emitted electrons usually have energies ranging from 20 eV to 2 keV, and at these values, electrons have a short mean free path in a solid. The escape depth of electrons [12] is therefore localized to within a few nanometers of the target surface, thus probing only the first few layers of the solid.

However, techniques that can directly observe the dynamics of adsorbates on sur-

faces were not developed until later. The main difficulty in resolving these processes comes from the characteristically short time scale, between femtoseconds and picoseconds, for an adsorbate to vibrate, rotate or translate. Typical light sources for XPS emit photons with "long" pulse durations of several tens of picoseconds, while UPS helium lamps emit photons continuously. Therefore, conventional UPS and XPS techniques cannot be utilized in this case. The development of femtosecond Ti:Sapphire laser systems was crucial for the improved understanding of surface processes. The ultrashort pulse duration delivered by these laser systems allowed the real-time study of dynamic surface processes through pump-probe techniques such as time-resolved two-photon photoemission (TR-2PPE), see figure 1.1.

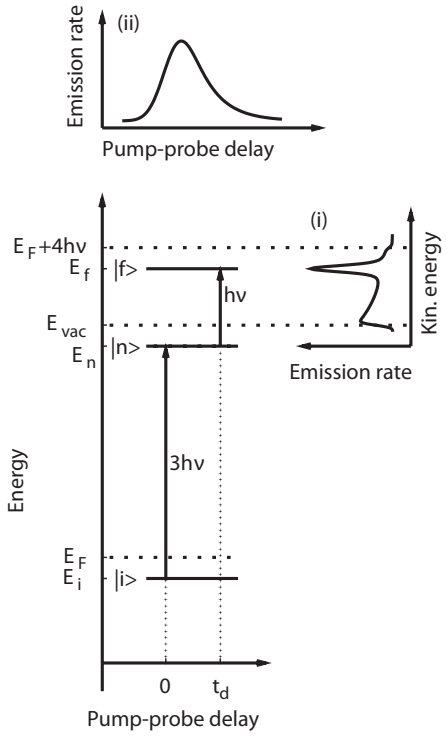

Figure 1.1: Schematic representation of bichromatic 2PPE. The electron is excited from the occupied initial state $|i\rangle$ to the intermediate state $|n\rangle$ and final state $|f\rangle$ by the pump ($3h\nu$) and probe ($h\nu$) laser pulses. (i) Electrons are detected as a function of kinetic energy for fixed delay t_d between pump and probe pulses or (ii) for a fixed kinetic energy as a function of the time delay between pump and probe pulses. Adapted from reference [1].

Two-photon photoemission (2PPE) [13,14] spectroscopy has the unique capability of directly observing electrons with specific energy and momentum within the skin-depth of a surface. In addition, 2PPE combines characteristics of traditional photoemission and inverse photoemission spectroscopies, which makes it the method of choice for the study of ultrafast electron dynamics at surfaces. Initial experiments with picosecond time-resolution focused on the electron-phonon scattering in metals [15] and the dynamics of thermalized band-edge carriers in semiconductors [16]. Improvements in energy and time resolution allowed the study of unoccupied bands and surface states in metals [13]. With the further development of ultrafast lasers, time-resolved two-photon photoemission became a powerful tool to analyze the dynamics of non-thermalized electrons ("hot electrons") and unoccupied surface states directly in the time domain [17]. The first applications of TR-2PPE on femtosecond time scales included measurements of electron-electron scattering rates in metals [17–19] and image-potential-state lifetimes on metallic surfaces [20]. Further applications of ultrafast lasers in TR-2PPE led to the discovery of a novel mechanism of adsorbate desorption from metal surfaces in the femtosecond time regime, mediated by direct charge transfer of "hot electrons" [21, 22]. This opened a new pathway in photochemical reactions.

The photon energy used in these TR-2PPE experiments must be lower than the work function of the substrate, thus below 5 - 6 eV. In this energy regime, TR-2PPE experiments only probe a relatively restricted bandwidth of the surface electronic states, specifically those unoccupied states located a few electronvolts around the Fermi edge. Nevertheless, the study of deeper electron levels is also important because these levels contain information on the surface structure and the chemical and magnetic state of the surface. In order to perform these studies, the ultrafast photon sources need to extend their excitation energies into the extreme-ultraviolet (EUV) and x-ray regions of the spectrum (see figure 1.2).

In the late eighties, Rhodes [23], Manus [24] and coworkers described for the first

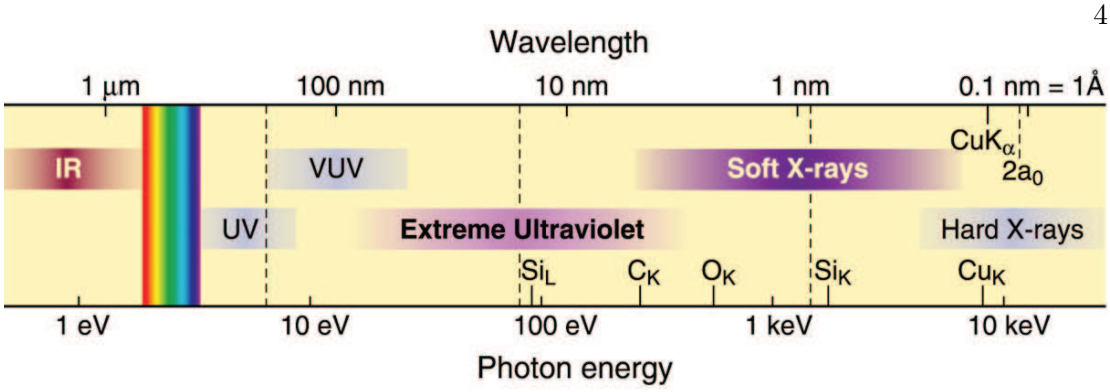

Figure 1.2: Electromagnetic spectrum with emphasis on the extreme ultraviolet and soft x-ray portions.

time the generation of high-order harmonics (HHG) and reported the conversion of the Ti:Sapphire amplifier output to ultrashort coherent light pulses in the VUV, EUV and x-ray regions of the spectrum. So far, HHG photon energies on the order of 1 keV [25–28] and pulse durations as short as 80 attoseconds [29–31] have been observed. It is this latter property that makes HHG a unique tool for the study of dynamic processes when high temporal resolution is required. Therefore, using a high-order harmonic source in a surface science PE experiment within a pump-probe scheme provides exciting insights into dynamic surface processes on extremely short time scales. Haight *et al.*, pioneered the use of HHG in surface science by demonstrating that HHG can be used as a light source for valence- and core-level photoelectron spectroscopy [32]. They recognized the two main advantages of an HHG light source compared to conventional, short-wavelength light sources. Namely, that the harmonic source is both small-scale (table-top) and tunable, and that the short pulse structure is capable of real-time experiments on a femtosecond scale.

To date, high harmonic generation has been successfully used to study electron relaxation in materials [33–36], surface adsorbate dynamics [37, 38], photoacoustic dynamics [39], and molecular dissociation [40]. More recently, high harmonics have been

used as a pump beam to study x-ray-induced molecular dynamics [41]. Although photon energies > 1 keV can be generated using high harmonic emission, the photon flux is too low above 100 eV to be employed routinely in experiments.

Time-resolved experiments using ultrafast high-harmonic light have also been greatly expanded by the application of laser-assisted, strong-field dynamic processes. When an electron is photoejected in the presence of an intense laser field of 10^{11} W/cm^2, the electron is accelerated by the laser field. If the interaction occurs continuously over several optical cycles, the electron undergoes oscillations. This leads to ponderomotive energy shifts, and, in the presence of atomic nuclei or solids that can absorb momentum, to the generation of sidebands in the photoelectron spectrum. These sidebands correspond to the absorption and stimulated emission of photons from the laser field.

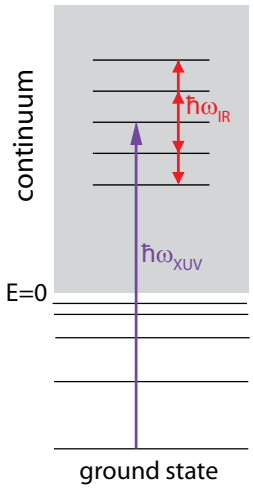

Figure 1.3: The principle behind the laser-assisted photoemission process for atoms in the "soft photon" limit. LAPE is described in two steps. First, the ground state electron is photoemitted into an excited state in the continuum by the XUV pulse, neglecting the influence of the IR field. Then, the photoemitted electron evolves as a free electron in the IR field, unaffected by the atomic potential. This results in a redistribution of the electrons in the continuum by absorption and stimulated emission of IR photons.

This laser-assisted photoeffect (figure 1.3) is considered to result from "dressing" of the free-electron wave function; i.e., the electron evolves in a state where the free

electron is driven by the IR laser field. These dressed states are known as Volkov waves. Laser-assisted electron dynamics were first observed in electron-atom scattering in the presence of a strong CO_2 laser field [42]. Later, this process was applied to time-resolved measurements of laser-assisted Auger decay (LAAD) [43], using ultrashort-pulse, soft x-ray plasma sources [44]. Laser-assisted photoemission (LAPE) was first observed by Glover et al. [2], using high harmonic sources. In these experiments, atoms were simultaneously irradiated by XUV and intense infrared (IR) light. The presence of the IR laser modifies the XUV photoelectron spectrum. In both cases, LAAD and LAPE, the observation of laser-assisted dynamics indicates the emission time of the photoelectrons or Auger electrons. By varying the time delay between the XUV and IR pulses, the LAPE signal provides an exact timing synchronization between the pulses, as well as providing a cross-correlation between the laser and XUV fields.

More recently, LAPE and LAAD have been combined to measure ultrafast, core-level dynamics in Krypton atoms [3]. In this experiment, LAPE provides time zero while LAAD yields the emission-time behavior of the delayed Auger electrons. In this way, the lifetime of an M-shell vacancy in Krypton could be measured directly in the time domain. Figure 1.4 contains a compilation of experimental results of LAPE from atoms. It has also been shown that with XUV pulse durations in the sub-optical cycle domain, LAPE becomes sensitive to the IR electric field rather than the intensity envelope, giving rise to sub-femtosecond resolution in time-resolved experiments [29, 30, 45–47]. Recently, LAPE has been successfully demonstrated with femtosecond XUV pulses from the free-electron laser FLASH at DESY in Hamburg [4].

However until 2006, laser-assisted photoemission and laser-assisted Auger decay had only been observed in gas-phase atomic systems. This limits the applicability of the physics of laser-assisted dynamics to the study of isolated atoms or molecules. Furthermore, this constraint also represents a practical limit to the use of LAPE for XUV pulse characterization, since both atomic photoionization cross-sections and the

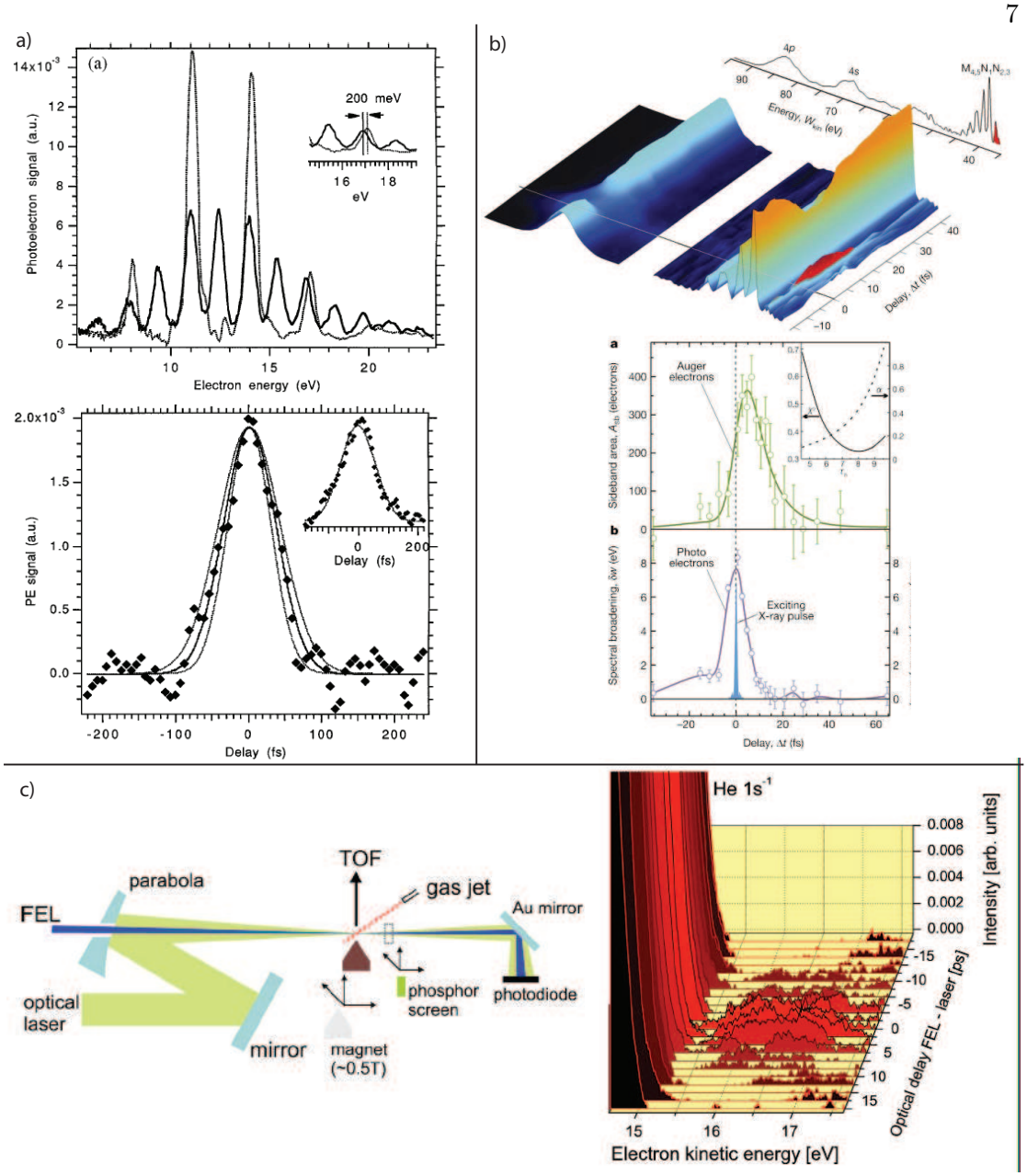

Figure 1.4: Compilation of experiments that studied LAPE from atoms. a) Upper: HHG photoelectron spectra of He obtained in the presence (solid line) and absence (dashed line) of the laser pulse. Notice the appearance of sidebands in the presence of the laser pulse. Lower: Height of the 11 eV PE peak as a function of delay. Gaussian fit (FWHM = 138 fs) to the data is shown as a solid curve and indicates a soft x-ray pulse duration of 120 fs. From reference [2]. b) Upper: Temporal evolution of Kr photoelectron spectra following core excitation. Note the manifestation of sidebands at both the $4p$ and Auger peaks. Lower: Temporal evolution of the $4p$ and Auger sideband heights. The lifetime of the Kr core hole can be obtained from these data. Adapted from reference [3]. c) Left: Experimental setup for the observation LAPE using the FEL and an optical laser. Right: Part of the photoelectron spectrum in the region of the He $1s^{-1}$ main line and the high-energy sideband. From reference [4].

obtainable photon flux from high-harmonic sources decrease rapidly with increasing photon energy. The result has been that, due to the low target densities in the gas phase, current XUV pulse duration measurements are limited to photon energies below 100 eV. Other approaches for characterizing ultrashort XUV pulses, such as the autocorrelation using two-photon absorption [48, 49], are even more experimentally challenging at very high photon energies. To date, these techniques have only been demonstrated at photon energies lower than 50 eV.

Our group reported the first observation of the laser-assisted photoelectric effect in solid-state systems [50]. In our work, a clean Pt(111) single crystal was used as the solid surface, since it exhibits a large density of d-states at the Fermi edge, with a characteristic peak-like structure in the XUV photoelectron spectrum. In the presence of an intense laser field, sidebands appeared in the Pt(111) photoemission spectrum. We showed that the modification of the photoelectron spectrum by LAPE can be distinguished from simple heating of the electrons by the IR beam in three ways: *i*) by varying the laser polarization, *ii*) by measuring the mean energy of the photo-ejected electrons and verifying that it does not change, and *iii*) by successfully fitting the photoelectron spectrum to theory. We also demonstrated that surface LAPE can be used to measure the pulse duration of XUV pulses. Since then, surface LAPE has been successfully combined with attosecond soft x-ray pulses [51] and with femtosecond XUV pulses from the FLASH free-electron laser [52]. Recently, we reported the first direct time-resolved observation of core-level relaxation dynamics in a complex surface-adsorbate system by combining surface LAPE and LAAD [53].

This thesis presents a detailed description of the above mentioned experimental results. The work presented here is organized as follows: Chapter 2 discusses the theory of high-harmonic generation and laser-assisted photoemission. Chapter 3 presents a detailed overview of the experimental setup used for the observation of surface LAPE. Chapter 4 reports the first experimental observation of surface LAPE and distinguishes

surface LAPE form other laser-surface interaction phenomena. The results presented in chapter 4 agree with the atomic-based model presented in chapter 2. By combining surface LAPE and laser-assisted Auger decay, chapter 5 presents the direct time-resolved measurement of a core-excited state lifetime of an atom adsorbed onto a surface. This result is fundamental for the understanding of charge-transfer processes between substrates and adsorbates. Chapter 6 shows that using a dressing laser at longer wavelengths dramatically reduces undesirable laser-surface phenomena while enhancing the signal from surface LAPE. These results enable ultrafast studies of surface-adsorbate systems and attosecond electron dynamics over a wider energy range. Chapter 7 proposes future experiments for the study of electron dynamics on surfaces. This chapter places special emphasis on future modifications to the experimental setup that will allow the parallel detection of energy and momentum of the photoemitted electrons. Finally, chapter 8 summarizes the experimental results presented in this thesis.

Chapter 2

Theory

2.1 High-Harmonic Generation

2.1.1 Introduction

The last two decades have been a revolutionary period in the development of ultrashort light sources in the extreme-ultraviolet (EUV) and soft x-ray (SXR) regions of the electromagnetic spectrum. This has happened in part due to the improvement of a new generation of ultrafast lasers [54,55], which can generate pulses with durations of $\leq$ 10 fs. When these intense femtosecond laser pulses are focused into a gas, the interaction between the light pulse and the electrons of the atoms in the gas is so strongly nonlinear that high harmonics of the laser frequency are radiated. The high-energy photons from this process extend into the soft x-ray region of the spectrum [5,28]. Since all the atoms experience a similar coherent light field, the x-ray emissions from individual atoms are coherent. Therefore, a coherent x-ray beam is emitted in the forward direction, colinear with the fundamental laser light.

Because of the ultrashort pulse duration at short wavelengths of the light pulses generated through high-harmonic generation (HHG), a new window through which to observe nature is available. Due to the short wavelength, HHG light allows the imaging of small features, since the resolution of an optical system is proportional to the wavelength of the light [56]. Analogously, HHG light sources allow for the writing of small

patterns via photolithography. Furthermore, ultrafast x-ray pulses have the potential to directly monitor atomic motion in chemical and material reactions [36, 37, 40, 41, 57].

Over the last several years, high-harmonic generation has progressed from a novel nonlinear process to a robust table-top source of ultrafast high-energy photons. A fundamental part of this improvement was based on the better understanding of this process. In the next section the theoretical treatment of HHG will be reviewed.

2.1.2 Theoretical treatment

As mentioned before, high-harmonic generation is a term used to describe the nonlinear interaction between an intense laser pulse and a medium (usually a gas) that results in the generation of harmonics of the driving laser field. This process can be distinguished from low-order harmonics in that it cannot be described by perturbation theory. Some of the unique characteristics of high-harmonic generation are:

- A sharp cutoff where the high-harmonics signal drops rapidly.
- A long plateau of harmonics with similar intensities.
- Intense low-order harmonics, whose intensities follow perturbation theory.

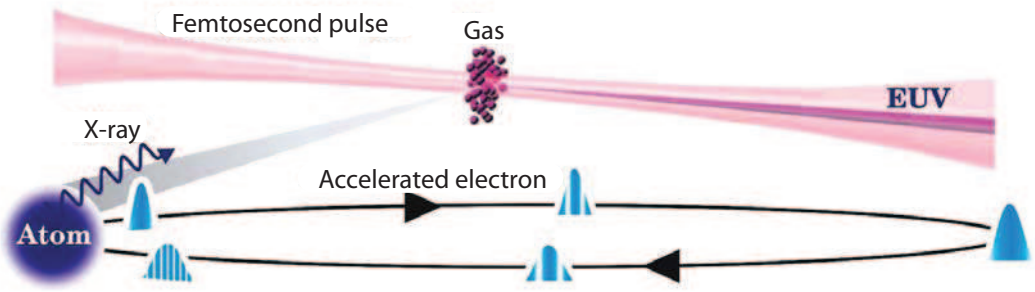

Figure 2.1: Pictorial representation of the three-step model. From reference [5].

The theory of HHG has been the subject of extensive investigation over the last two decades. An intuitive physical interpretation of HHG has been developed, primarily

by Ken Kulander, Paul Corkum, and co-workers, that explains HHG as a three-step "rescattering" process [58, 59]:

(1) Ionization of the atom.

(2) Classical acceleration of the free electron by the laser field.

(3) Recombination of the electron with the parent ion.

The first step in the HHG process occurs when the electric field of the driving laser is sufficient to ionize the target atom. There are three ways to ionize an atom: multiphoton, tunnel, and above barrier ionization (see figure 2.2). The Keldysh parameter, γ, is the common yardstick used to determine which of these various ionization processes occurs [60]. It is defined as the ratio of the laser frequency to the tunneling frequency.

$$\gamma = \frac{\omega_{\text{laser}}}{\omega_{\text{tunnel}}} = \sqrt{\frac{I_p}{2U_p}}, \tag{2.1}$$

where I_p is the ionization potential of the atom, and U_p is the ponderomotive potential or the energy gained by the electron in an oscillating field (see Appendix A). In terms of the laser intensity I in W/cm^2 and the wavelength λ in μm, the ponderomotive potential, in electronvolts, is given by:

$$U_p \approx 9.33 \times 10^{-14} I \lambda^2, \tag{2.2}$$

If the laser intensity is small ($\gamma \gg 1$), then multiphoton ionization is dominant. In this regime, the effective potential is only slightly modified from the Coulomb potential by the laser field and ionization occurs by the absorption of N photons (figure 2.2(a)). In this case, the ionization can be treated as a perturbative process. Tunnel ionization becomes the dominant process at larger laser intensities, where $\gamma < 1$ (figure 2.2(b)). In this regime, the effective potential is severly distorted by the laser field, allowing the

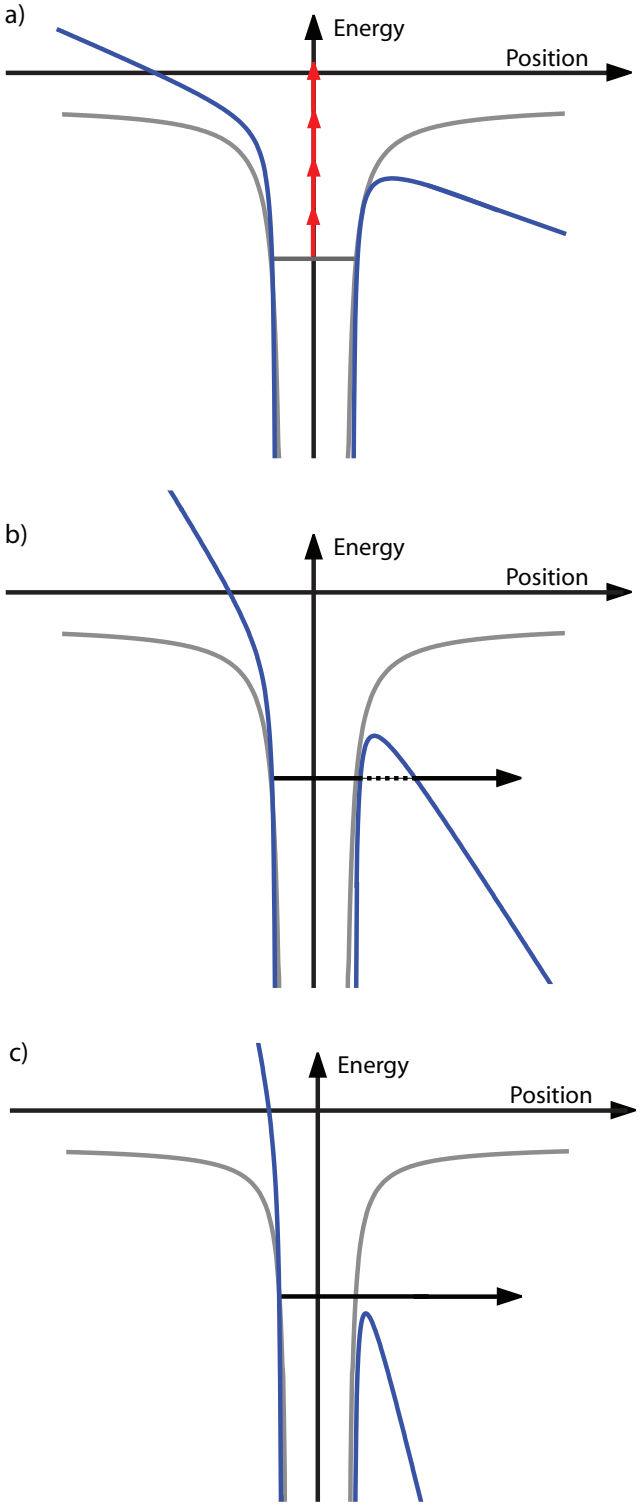

Figure 2.2: Photoionization processes for different laser intensities: a) multiphoton absorption ($\gamma \gg 1$), b) tunneling ($\gamma < 1$), and c) above barrier ionization ($\gamma \ll 1$). The gray line corresponds to the Coulomb potential, while the blue line corresponds to the Coulomb potential modified by the laser field.

electron to tunnel through the atom. An expression for the tunnel ionization probability of an atom in an oscillating field, which is known as ADK ionization rate, was developed by Ammosov, Delone, and Krainov [61]. For the typical situation of neutral Argon ($I_p = 15.76$ eV) interacting with an 800 nm laser pulse, tunnel ionization becomes the dominant mechanism for intensities $I_p > 10^{14}$ W/cm^2. Tyical intensities in HHG experiments are $> 10^{14}-10^{16}$ W/cm^2, making tunnel ionization the dominant ionization mechanism. For very intense optical pulses ($\gamma \ll 1$), the Coulomb barrier may be suppressed below the ionization potential while there still exists a large population in the ground state (figure 2.2(c)). This regime is called above-barrier ionization.

After ionization, the next step is the acceleration of the free electron in the laser field. The assumption that the electron is free after ionization is justified because outside of the atomic potential, the laser field is much greater than the Coulomb potential. Furthermore, the electron and the field, due to the large number of states available to the electron, may be treated classically. The electric field is given by $\mathbf{E}(t) = E_0 \cos(\omega t)\hat{\mathbf{e}}_x + \alpha E_0 \sin(\omega t)\hat{\mathbf{e}}_y$, where E_0 is the field strength, ω is the laser frequency and α is the ellipticity (± 1 for circularly polarized light, 0 for linearly polarized light), and the electron's equations of motion (equations 2.3–2.6) are obtained by integrating $\mathbf{F}(t) = m\mathbf{a} = e\mathbf{E}(t)$,

$$v_x(t) = \frac{eE_0}{\omega m}\sin\omega t + v_{0x} \tag{2.3}$$

$$x(t) = -\frac{eE_0}{\omega^2 m}\cos\omega t + v_{0x}t + x_0 \tag{2.4}$$

$$v_y(t) = -\frac{\alpha eE_0}{\omega m}\cos\omega t + v_{0y} \tag{2.5}$$

$$y(t) = -\frac{\alpha eE_0}{\omega^2 m}\sin\omega t + v_{0y}t + y_0 \tag{2.6}$$

where v_{0x}, v_{0y}, x_0, and y_0 can be evaluated from the initial condition of the tunneling electron. It is assumed that as the electron tunnels through the barrier into the continuum, it does so with zero velocity at the position where the ionization potential and

the Coulomb + laser potential are equal. This position is usually a few Å, while the electron's excursion in the field is a few nm. Thus, the electron is considered to be at the origin when it tunnels into the continuum. From equations 2.3–2.6 it is possible to see that if the light is circularly polarized, the electron will not return to the position of the parent ion. For high-harmonic generation linearly polarized light has to be used, since the electron must return to the parent ion.

Equations 2.3–2.6 demonstrate that the kinetic energy of the returning electron will depend on the phase of the driving laser field at the time the electron tunnels through the barrier. Figure 2.3 shows a one dimensional calculation of the trajectory of the free electron for several initial phases of the laser field. This calculation shows that if the electron is emitted between 0° and 90° phase, it will return to the position of the parent ion. Furthermore, it is also possible to calculate the energy of the returning electron as a function of the phase of the laser pulse when the electron tunnels through the barrier (see figure 2.4). Notice that during its excursion in the laser field, the electron can gain energy up to $\approx 3.17U_p$. This happens when the electron is released into the field with a phase of $\approx 18°$. It is possible for an electron to gain more energy than $3.17U_p$, but that would require for the electron to be released at a phase of $\approx 180°$ or to stay in the laser field longer than one optical cycle (2.6 fs for 800 nm light), where the ionization probability is very low [58].

The final step in the three-step model is the recombination process. An electron returning to the parent ion can scatter elastically, ionize the ion collisionally, or emit a photon via recombination with the ion. If the electron recombines with the parent ion in the ground state and emits a photon, conservation of energy dictates that the photon cannot have more energy than $I_p + 3.17U_p$. This is known as the HHG cutoff (equation 2.7) and determines the maximum photon energy that can be emitted through HHG.

$$h\nu_{max} = I_p + 3.17U_p \tag{2.7}$$

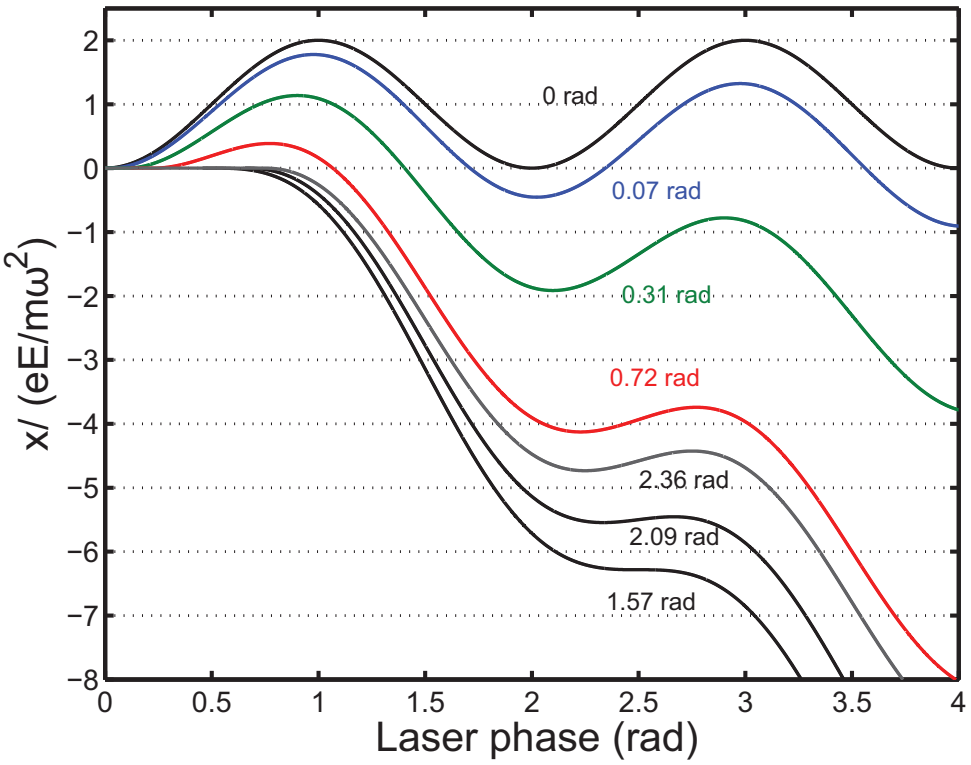

Figure 2.3: Possible paths for the electron during rescattering as a function of laser phase, and several selected values of the phase of the laser at ionization. Intersection with the x-axis indicates the possibility of recombination. Adapted from reference [6].

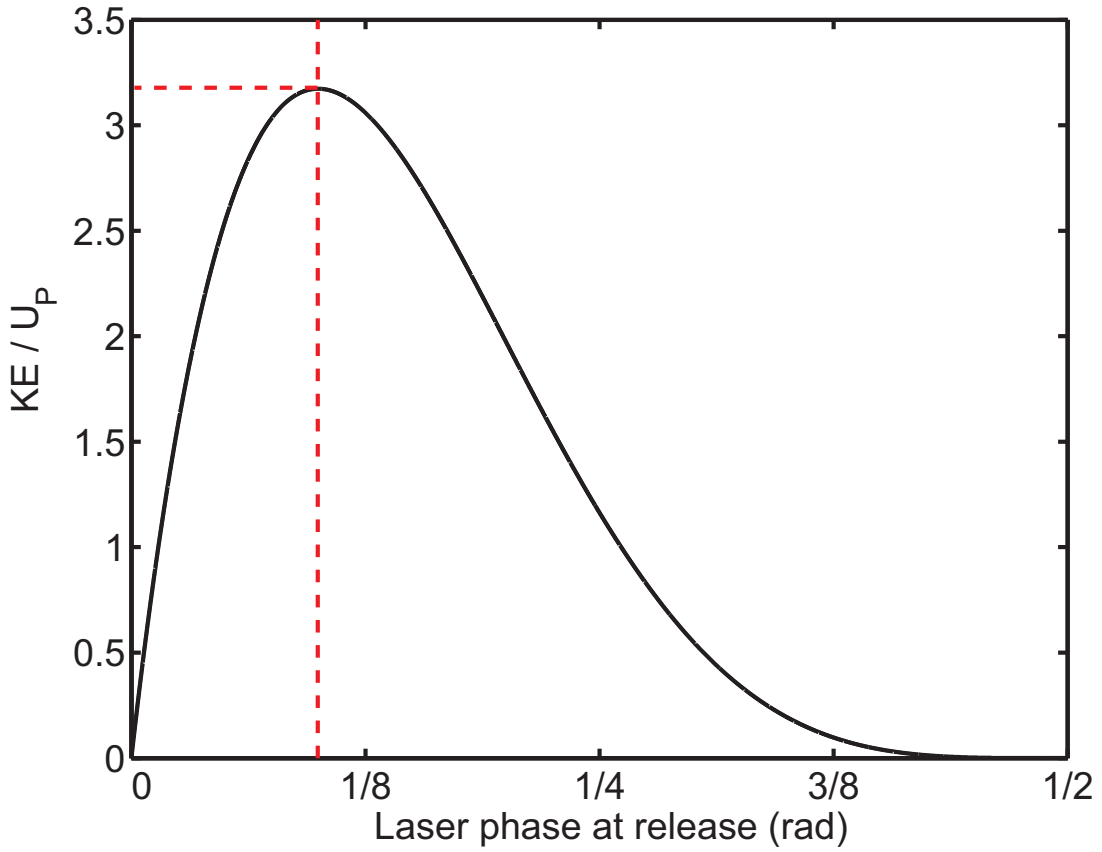

Figure 2.4: Energy of the returning electron as a function of laser phase. The red dotted line indicates the maximum kinetic energy (3.17 U_p) at phase value of $\approx 18°$. Adapted from reference [7].

This emission of light upon recombination can be calculated with the dipole operator $d(t) = \langle\psi|e\, r(t)|\psi\rangle$ [59]. The phase of the dipole operator is given by $\exp\left[-iS(t_i, t_f)\right]$, where $S(t_i, t_f)$, the quasi-classical action (equation 2.8), is the phase accumulated by the electron in the laser field,

$$S(t_i, t_f) = \int_{t_i}^{t_f} dt'' \left(\frac{[\mathbf{p}(t_i, t_f) - \mathbf{A}(t'')]^2}{2} + I_p \right) \tag{2.8}$$

where $\mathbf{p}(t_i, t_f)$ is the momentum corresponding to an electron ionized at time t_i and recombined at t_f, $\mathbf{A}(t)$ is the vector potential of the laser field, I_p is the ionization potential of the atom, and t_i and t_f are the ionization and recombination times, respectively. The stationary points of this phase determine which trajectories have the most significant contribution to the dipole moment. For a given harmonic, the dominant contribution comes from two trajectories: one with a short return time, and one with a long return time. Therefore, these two trajectories contribute photons of the same energy. Thus quasi-classical action also determines the phase of the emitted harmonic [62]:

$$\Phi_{at} = q\omega t_f - S(t_i, t_f)/\hbar \tag{2.9}$$

where ω is the driving laser angular frequency, and q is the harmonic order. Equation 2.9 shows that the phase of the emitted harmonics is dependent on the intensity of the IR driving field; therefore, by modulating the laser intensity, it should be possible to adjust the phase relation between the driving field and the harmonic field.

The single atom response is proportional to the absolute square of the Fourier transform of the dipole operator $d(\omega) = F\{d(t)\}$. References [58] and [59] contain $|d(\omega)|^2$ plots where the same qualitative behavior of high-harmonic generation is shown: a sharp cutoff, a long plateau, and a perturbative behavior for the low order harmonics.

This three-step process will repeat itself for every half cycle of the driving field, therefore generating odd harmonics of the driving field. This is due to symmetry con-

siderations in the nonlinear optical process - the generation of even harmonics requires a medium without inversion symmetry, which does not exist in a gas. If the symmetry is broken by introducing a second pulse of a different wavelength, it is possible to generate even and odd harmonics of the driving field.

2.1.3 Phase-matching

High-harmonic generation has proven to be a practical and useful light source for photoelectron spectroscopy [63]; however, the limited photon flux generated through HHG can limit its application in different research areas. The efficiency of HHG has been limited by the fact that the process is not phase-matched, in that the propagation speed of the x-rays and the fundamental light are different from each other. This limits the interaction length over which the electric field of the x-rays can build constructively. The highest conversion efficiencies reported to date are on the order of 10^{-5} to 10^{-6} [5, 64].

From classical nonlinear optics, the field of the q^{th} harmonic, after propagating through a nonlinear medium of length L, is

$$E_q \propto \int_0^L E_f^n d(z) \exp\left[-i\Delta k z\right] dz \tag{2.10}$$

where E_f is the driving field, n is the effective order of the nonlinear process, $d(z)$ is the nonlinear coefficient, $\Delta k = qk_f - k_q$ is the phase mismatch, and k_f and k_q are the wave vectors of the fundamental field and the q^{th} harmonic, respectively. As can be seen from equation 2.10 and figure 2.5, the intensity of the q^{th} harmonic at the exit of the medium is maximized when $\Delta k = 0$. Furthermore, integrating equation 2.10, under the assumption that E_f^n and $d(z)$ are independent of the propagation direction z, allows us to obtain the relation between the intensity of the q^{th} harmonic and the phase mismatch,

$$E_q \propto L^2 \mathrm{sinc}^2\left(\frac{\Delta k L}{2}\right). \tag{2.11}$$

Figure 2.6 shows the harmonic signal growth as a function of the medium length for different phase mismatch values. When $\Delta k = 0$, the harmonic signal grows quadratically with medium length, while for $\Delta k \neq 0$ the harmonic intensity oscillates. These oscillations can be described in terms of a characteristic length, the coherence length:

$$L_c = \frac{\pi}{\Delta k} \tag{2.12}$$

The coherence length is defined as the length necessary for a phase shift of π to develop between the signal generated at two different positions along the propagation direction. In other words, it is the length over which the harmonic signal increases before being converted back into the fundamental field. As seen in figure 2.6, a larger phase mismatch results in a shorter coherence length and less harmonic signal.

Early attempts at phase matching involved adjusting the laser to either focus before or after a gas jet of a noble gas [65]. However, by using a gas jet of noble gas, the interaction length is limited by the size of the jet, so efficient generation of high-harmonics is not achieved. Later, phase matching by pressure tuning in a hollow, gas-filled waveguide was demonstrated [66, 67]. For HHG in a hollow waveguide, the phase mismatch originates from three dispersion mechanisms: *i*) the neutral gas (Δk_n), *ii*) the free electrons (Δk_p), and *iii*) the waveguide (Δk_w). At the high-harmonic wavelengths, it is assumed that the neutral gas has an index of refraction ≈ 1, and that the HHG signal is generated with a small spatial profile such that it does not interact with the waveguide. Under these assumptions, the phase mismatch in a hollow waveguide is:

$$\Delta k = \Delta k_n + \Delta k_p + \Delta k_w \tag{2.13}$$

$$= \frac{2\pi q P \delta_n (1-\eta)}{\lambda P_{atm}} - \frac{\eta P N_{atm} \mathrm{r}_e}{P_{atm}}\left(q\lambda - \frac{\lambda}{q}\right) - \frac{q u_{nm}^2 \lambda}{4\pi a^2} \tag{2.14}$$

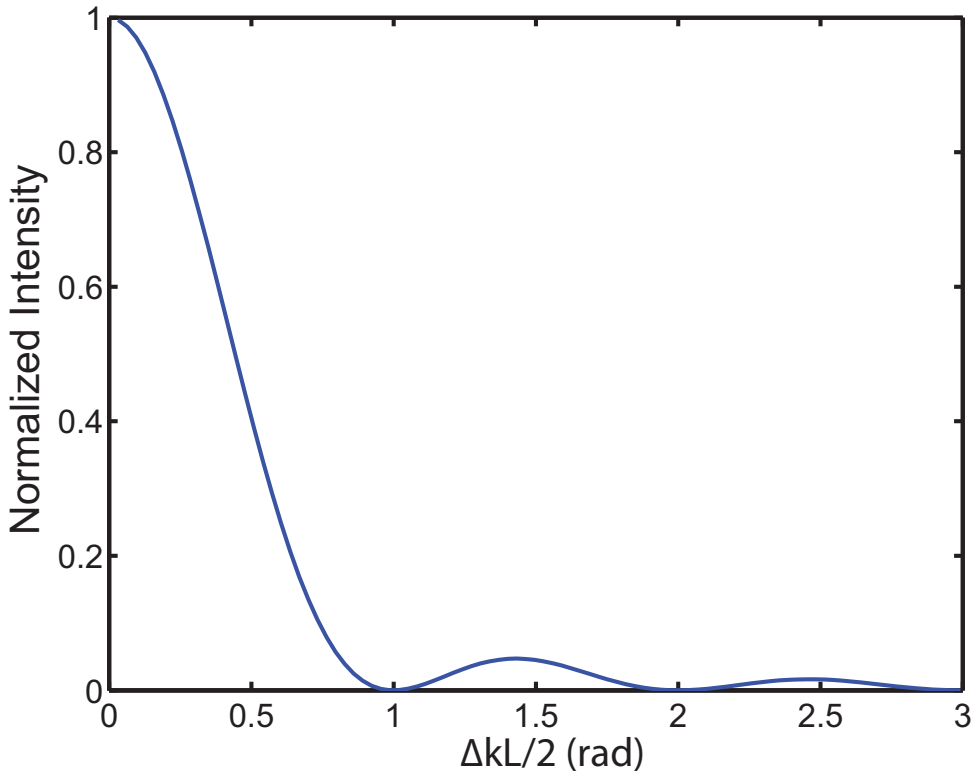

Figure 2.5: Normalized HHG intensity as a function of phase mismatch. Adapted from reference [7].

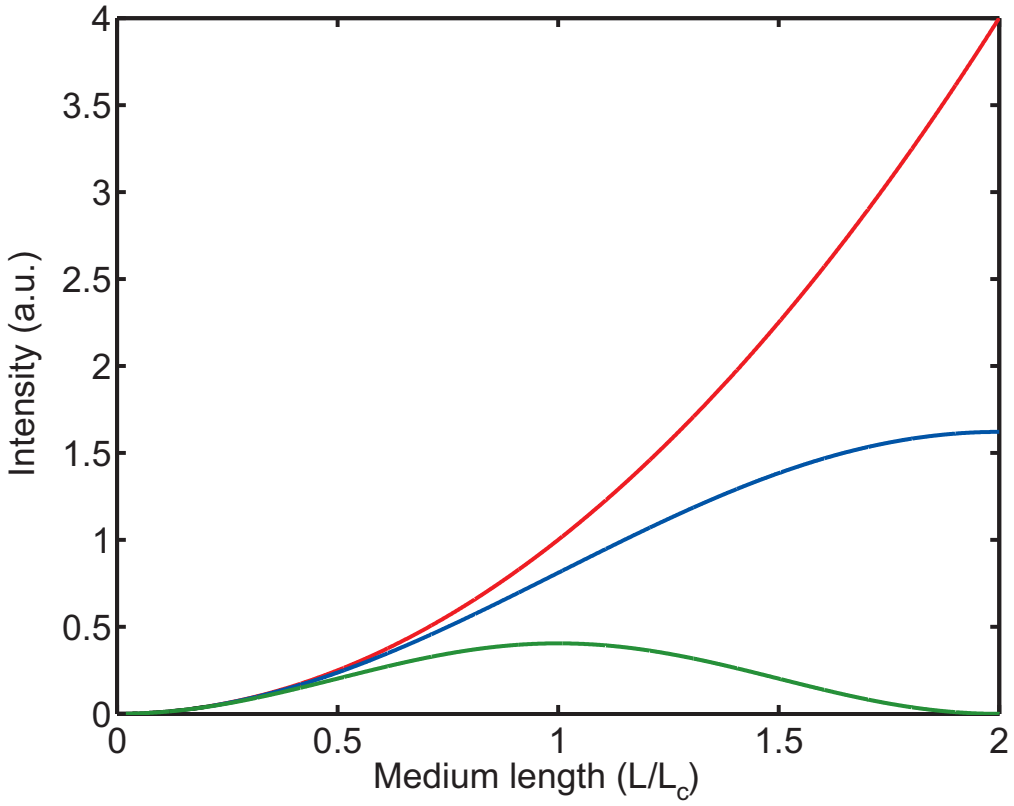

Figure 2.6: The high-harmonic and laser light go out of phase as they propagate through the medium. The coherence length L_c is defined as the length over which HHG and laser light remain in phase. If phase matching ($\Delta k = 0$, red) is achieved, the signal will increase quadratically. Larger phase mismatch values (shorter coherence lengths) result in lower HHG signal (blue $\rightarrow \Delta k = \pi/(2L_c)$, and green $\rightarrow \Delta k = \pi/L_c$).

where λ is the fundamental wavelength, q is the harmonic order, r_e is the classical electron radius, u_{nm} is a constant corresponding to the propagation mode in the waveguide, a is the waveguide radius, η is the fractional level of ionization, P is the gas pressure, P_{atm} is the atmospheric pressure, $\delta_n = n_{gas} - 1$ is the deviation of the neutral gas index of refraction from that of a vacuum, and N_{atm} is the gas density at atmospheric pressure. For small values of η there exists a pressure for which $\Delta k = 0$, but for large η phase matching is not possible and quasi-phase matching techniques are necessary [68, 69].

2.2 Laser-Assisted Dynamics

This section will show how the conventional field-free calculations can be modified to handle the presence of a strong field. It will also emphasize the nature of the wave function of a free electron in a laser field, known as a Volkov wave function. This section follows closely the work of Madsen [70].

2.2.1 Volkov wave

Strong fields are well-described by the time-dependent vector potential

$$\boldsymbol{A}(\boldsymbol{r}, t) = \boldsymbol{A}_0 \cos(\omega t - \boldsymbol{k} \cdot \boldsymbol{r}), \tag{2.15}$$

with $\boldsymbol{k}$ being the wave vector of magnitude k determined by the dispersion relation $\omega = kc$, and $\boldsymbol{A}_0$ the amplitude along the polarization vector of the field $\boldsymbol{\epsilon}$. The electric field $\boldsymbol{E}$ associated with the vector potential of equation 2.15 is given by

$$\boldsymbol{E}(\boldsymbol{r}, t) = -\frac{\partial}{\partial t}\boldsymbol{A}(\boldsymbol{r}, t). \tag{2.16}$$

This sections uses atomic units $\hbar = m_e = e = a_0 = 1$, where e is the electron charge, m_e is the electron mass, and a_0 is the Bohr radius. The laser light is assumed to be linearly polarized. The Coulomb gauge with $\nabla \cdot \boldsymbol{A} = 0$ and vanishing scalar potential are also utilized through this section. The coupling between the laser and

the electron is expressed by replacing the momentum operator of the electron with the minimal coupled momentum, $\hat{\boldsymbol{p}} \rightarrow \hat{\boldsymbol{p}} + \boldsymbol{A}(\boldsymbol{r}, t)$ [70]. Hence, the dipole approximation, $\exp(i\boldsymbol{k} \cdot \boldsymbol{r}) \sim 1$, may be applied very accurately. Consequently, the Hamiltonian is

$$H_0 = \frac{(\hat{\boldsymbol{p}} + \boldsymbol{A}(t))^2}{2} = \frac{\hat{\boldsymbol{p}}^2}{2} + \boldsymbol{A}(t) \cdot \hat{\boldsymbol{p}} + \frac{\boldsymbol{A}(t)^2}{2}, \tag{2.17}$$

where the vector potential is only time dependent.

In cases where the interaction of the electron with the field is represented as in equation 2.17, the interaction is described by the velocity gauge. Even though a variety of gauges exist [71, 72], physical observables are independent of the gauge chosen. The Hamiltonian in equation 2.17 can be rewriten as

$$H_0' = \frac{\hat{\boldsymbol{p}}^2}{2} + \boldsymbol{r} \cdot \boldsymbol{E}(t). \tag{2.18}$$

In cases where the interaction of the electron with the field is represented as in equation 2.18, the interaction is described by the length gauge.

As approximations are introduced, one gauge may be more accurate for a description of the physics. As an example, the length gauge probes regions where the wave functions change rapidly with r, which in this case are typically positions close to the nucleus.

In this case the velocity gauge will be used because the mathematics are simpler to handle. Therefore, solving the time-dependent Schrödinger equation for positive energies,

$$i\frac{\partial}{\partial t}\psi(\boldsymbol{r}, t) = \left[\frac{\hat{\boldsymbol{p}}^2}{2} + \boldsymbol{A}(t) \cdot \hat{\boldsymbol{p}} + \frac{\boldsymbol{A}(t)^2}{2}\right]\psi(\boldsymbol{r}, t). \tag{2.19}$$

Where, if not for the coupling terms introduced by the external field, the solution to equation 2.19 would be the usual plane waves $\psi_0(\boldsymbol{r}, t) = (2\pi)^{-3/2} \exp i(\boldsymbol{q} \cdot \boldsymbol{r} - q^2 t/2)$ with $\hat{\boldsymbol{p}}^2\psi_0(\boldsymbol{r}, t) = \boldsymbol{q}^2\psi_0(\boldsymbol{r}, t)$. By direct substitution it can be verified that

$$\psi_V(\boldsymbol{r},t) = \frac{1}{(2\pi)^{3/2}} \exp i\left[\boldsymbol{q}\cdot\boldsymbol{r} - \int_0^t dt'\left(\frac{q^2}{2} + \boldsymbol{A}(t')\cdot\boldsymbol{q} + \frac{\boldsymbol{A}(t')^2}{2}\right)\right] \tag{2.20}$$

is a solution to equation 2.19. This solutions is called a Volkov wave after the author who first considered the wave function of a free (relativistic) electron in an electromagnetic field [73].

Before proceeding, it would be useful to introduce (see Appendix A)

$$U_p = \frac{A_0^2}{4} = \frac{E_0^2}{4\omega^2} \tag{2.21}$$

$$\boldsymbol{\alpha}_0 = \frac{\boldsymbol{A}_0}{\omega} = -\frac{\boldsymbol{E}_0}{\omega^2} \tag{2.22}$$

where U_p stands for the ponderomotive potential - the kinetic energy of an electron in the laser field averaged over an optical cycle - and $\boldsymbol{\alpha}_0$ denotes the maximal classical excursion of the electron in its oscillatory motion in the field.

By evaluating the integrals in equation 2.19 and by using U_p and $\boldsymbol{\alpha}_0$, the Volkov wave may be written in a different way (see Appendix A):

$$\psi_V(\boldsymbol{r},t) = \frac{1}{(2\pi)^{3/2}} \exp i\left[\boldsymbol{q}\cdot\boldsymbol{r} - \boldsymbol{q}\cdot\boldsymbol{\alpha_0}\sin\omega t - \frac{U_p}{2\omega}\sin 2\omega t - \left(\frac{q^2}{2} + U_p\right)t\right]. \tag{2.23}$$

In equation 2.23 the first term of the exponent describes the plane wave motion of the electron with energy $q^2/2$ as indicated by the presence of this factor in the last term. The rest of the terms in the exponent are due to the interaction of the electron with the laser field. The $U_p t$ and $U_p/(2\omega)\sin 2\omega t$ terms describe an oscillating and constant energy shift gained by the electron in the presence of the field, while the second term describes the oscillatory motion of the electron of amplitude $\boldsymbol{\alpha}_0$ along the direction of the field's polarization.

Unfortunately, the expression in equation 2.23 is not well-suited for the calculation of the matrix elements due to the sinusoidal time-dependence of the exponent. A simpler exponential form may be obtained by introducing a sum over the generalized Bessel functions $J_n(u, v)$. The form of the generating function of these functions [74, 75]

$$\sum_{n=-\infty}^{\infty} e^{in\phi} J_n(u, v) = \exp i(u \sin\phi + v \sin 2\phi), \tag{2.24}$$

may immediately be used in equation 2.23. Thus, the expression for the Volkov wave is

$$\psi_V(\boldsymbol{r}, t) = \frac{1}{(2\pi)^{3/2}} e^{i\boldsymbol{q}\cdot\boldsymbol{r}} \sum_{n=-\infty}^{\infty} e^{-i(q^2/2 + U_p + n\omega)t} J_n\left(\boldsymbol{\alpha}_0 \cdot \boldsymbol{q}, \frac{U_p}{2\omega}\right). \tag{2.25}$$

As shall be seen, the Volkov wave function in equation 2.25 allows a simple evaluation of the time integrals occurring in the matrix elements.

2.2.2 Laser-assisted scattering

Laser-assisted elastic electron scattering is a process of the type

$$e_{\boldsymbol{q}_i} + A_i \rightarrow e_{\boldsymbol{q}_f} + A_i, \tag{2.26}$$

where atom A remains in its initial state A_i during the collision while the electron exchanges ℓ quanta with the laser field to change energy from $q_i^2/2$ to

$$\frac{q_f^2}{2} = \frac{q_i^2}{2} + \ell\omega \tag{2.27}$$

and momentum from $\boldsymbol{q}_i$ to

$$\boldsymbol{q}_f = \boldsymbol{q}_i + \boldsymbol{Q}, \tag{2.28}$$

where $\boldsymbol{Q}$ is the momentum transfer to the electron. This kind of process, known as free-free transition has been intensively studied experimentally and theoretically over the last two decades [76]. In a simple way, the electron-atom interaction is modeled by

a potential V, and the scattering is described by perturbation theory. Where if not for the presence of the field, the transition matrix element in the first Born approximation would simply be the matrix element of the potential sandwiched between two plane waves. However, the laser field turns the plane waves into Volkov waves, and the S-matrix element reads [77]

$$(S-1)^B_{fi} = -i\int_{-\infty}^{\infty} dt \langle \psi_V^{(f)} \mid V \mid \psi_V^{(i)} \rangle. \tag{2.29}$$

Substituting the expression for the Volkov waves in equation 2.25 into equation 2.29 and using the summation formula

$$\sum_{k=-\infty}^{\infty} J_{n\mp k}(u,v)J_k(u',v') = J_n(u \pm u', v \pm v'), \tag{2.30}$$

it is possible to derive (see Appendix A)

$$(S-1)^B_{fi} = -2\pi i \sum_{\ell} T^B_{fi}(\ell), \tag{2.31}$$

with $T^B_{fi}(\ell)$ the (transition) T-matrix for a scattering process with the exchange of ℓ photons

$$T^B_{fi}(\ell) = J_\ell(-\boldsymbol{\alpha}_0 \cdot \boldsymbol{Q})\tilde{V}(\boldsymbol{Q}), \tag{2.32}$$

and $\tilde{V}(\boldsymbol{Q})$ the Fourier transform of the potential

$$\tilde{V}(\boldsymbol{Q}) = \frac{1}{(2\pi)^3}\int d\boldsymbol{r} e^{-i\boldsymbol{Q}\cdot\boldsymbol{r}} V(\boldsymbol{r}). \tag{2.33}$$

In equation 2.31 the delta function expressing energy conservation has been suppressed, and the energy balance is given by equation 2.28.

The matrix element in equation 2.33 is the field-free T-matrix element in the first Born approximation. Thus, the differential cross-section for the exchange of ℓ photons reads

$$\frac{d\sigma^B(\ell)}{d\Omega} = J_\ell^2(\boldsymbol{\alpha}_0 \cdot \boldsymbol{Q})\frac{d\sigma^B}{d\Omega}. \tag{2.34}$$

Equation 2.34 expresses the laser-assisted cross-section in terms of the field-free cross-section and a Bessel function of integer order ℓ. The amplitude of the vector $\boldsymbol{\alpha}_0$ in equation 2.34 is related to the amplitude of the electric field by $E_0 = \omega^2\alpha_0$ as follows from equation 2.22. In the SI system, one atomic unit of field strength is given by $E_{\text{au}} = e/(4\pi\epsilon_0 a_0^2)$ with ϵ_0 as the vacuum permittivity. In this case, $E_{\text{au}} = 5.14 \times 10^9$ V/cm. The corresponding unit of intensity is the time-averaged Poynting vector $I_{\text{au}} = |E_{\text{au}}|^2/(2\mu_0 c)$, where μ_0 is the vacuum permeability, and the factor 1/2 comes from the time-averaging. When the values are substituted, $I_{\text{au}} = 3.51 \times 10^{16}$ W/cm^2. For field strengths and intensities on the order of E_{au} and I_{au}, the force exerted on the electrons by the laser field matches the strength of the field from the atomic nucleus.

The laser field does not need to be very strong to result in a nonperturbative coupling to the field. The point is that the coupling to the field enters through $\boldsymbol{\alpha}_0 \cdot \boldsymbol{Q}$. The larger the argument of the Bessel function, the more likely are high-order multiphoton processes. This result arises from the behavior of the Bessel function. The instantaneous kinetic momentum $\boldsymbol{p}(t)$ of an electron in the spatially uniform vector potential $\boldsymbol{A}(t)$ is given by

$$\boldsymbol{p}(t) = \boldsymbol{q} + \boldsymbol{A}(t), \tag{2.35}$$

where $\boldsymbol{q}$ is a constant vector that represents the time-averaged value of $\boldsymbol{p}(t)$. An electron with time-averaged momentum $\boldsymbol{q}_i$ will arrive at a scattering center at some time t and hence with incident momentum $\boldsymbol{p}_i$ determined by equation 2.35. Scattering is assumed to take place instantaneously (that is, in a time short compared with $1/\omega$) and elastically from an incident momentum $\boldsymbol{p}_i$ to a final momentum $\boldsymbol{p}_f$. Thus $\boldsymbol{A}(t)$ has the same value immediately after the collision as it had immediately before, and the time-averaged final

momentum $\boldsymbol{q}_f$ is determined by equation 2.35. Therefore,

$$\boldsymbol{q}_f - \boldsymbol{q}_i = \boldsymbol{p}_f(t) - \boldsymbol{p}_i(t) = \boldsymbol{Q}, \tag{2.36}$$

and, because $p_f^2 = p_i^2$,

$$q_f^2 - q_i^2 = -2\boldsymbol{Q} \cdot \boldsymbol{A}(t), \tag{2.37}$$

In a typical process $\boldsymbol{q}_f$ and $\boldsymbol{q}_i$ are regarded as the observables. Equation 2.37 then determines the value of $\boldsymbol{A}(t)$ at which the scattering took place, and equation 2.35 determines the values of $\boldsymbol{p}_f$ and $\boldsymbol{p}_i$ (and hence the energy) involved in the interaction with the scatterer.

In laser-assisted electron scattering, the role of the laser is to redistribute the electron intensity in different photon-exchange channels. This role may be seen formally by applying the summation formula

$$J_n(u,v) = \sum_{k=-\infty}^{\infty} J_{n-2k}(u) J_k(v), \tag{2.38}$$

for the Bessel functions from which it follows that

$$\sum_{\ell} \frac{d\sigma^B(\ell)}{d\Omega} = \frac{d\sigma^B}{d\Omega}. \tag{2.39}$$

This relation means, for example, that the cross-section for the exchange of zero photons is not equal to the field-free cross-section. Only in the limit of vanishing fields it is possible to find $\boldsymbol{\alpha}_0 \cdot \boldsymbol{Q} \sim 0$, and $J_\ell(0) = \delta_{\ell,0}$, from which the field-free cross-section can be obtained.

It has been shown [78] that equation 2.34 holds for the exact scattering cross-section in the limit that the photon energy is small compared to the kinetic energy of the electron. In this limit the theory predicts that the ratio of the laser-assisted cross-section to the field-free cross-section is given by the square of the Bessel function

$$\frac{d\sigma(\ell)}{d\Omega} = J_\ell^2(\boldsymbol{\alpha}_0 \cdot \boldsymbol{Q}). \tag{2.40}$$

Equation 2.40 is attractive because it allows a straightforward comparison with experiment, and this theory accounts well for data taken in experiment.

2.2.3 Laser-assisted photoelectric effect

The laser-assisted photoelectric effect is the process

$$\gamma + A \rightarrow A^+ + (e + \ell\hbar\omega), \tag{2.41}$$

where a high-energy photon γ is absorbed by an atom in the presence of a laser field. In the final state the continuum electron exchanges photons with the assisting laser field.

The Born approximation for the S-matrix expression for a transition from the initial atomic wave function Φ_0 to a final Volkov wave function ψ_V is

$$(S-1)_{fi}^B = -i \int_{-\infty}^{\infty} dt \langle \psi_V \mid \boldsymbol{A}_\gamma(t) \cdot \hat{\boldsymbol{p}} \mid \Phi_0 \rangle, \tag{2.42}$$

where $\Phi_0 = \phi(\boldsymbol{r})e^{iE_b t}$ with E_b as the binding energy of the initial electron wave function. Here $\boldsymbol{A}_\gamma(t)$ is the vector potential for the high-energy photon. In this process, the dipole approximation is introduced both for the laser field and the high-energy photon field. The strength of the coupling between the high-energy photon field and the electron is assumed to be sufficiently weak so that only the co-rotating (energy conserving part) of the interaction contributes. That is, in the matrix element of equation 2.42, the vector potential $\boldsymbol{A}_\gamma(t) = \boldsymbol{A}_{\gamma,0}\cos(\omega_\gamma t)$ is replaced by $\boldsymbol{A}_\gamma(t) = \boldsymbol{A}_{\gamma,0}/2\exp(-i\omega_\gamma t)$.

As before, by substituting the expression for the Volkov waves from equation 2.25 into equation 2.42, the following S-matrix element can be derived

$$(S-1)_{fi}^B = -2\pi i \sum_\ell T_{fi}(\ell), \tag{2.43}$$

where

$$T_{fi}(\ell) = \frac{1}{2}\boldsymbol{A}_{\gamma,0}\cdot\boldsymbol{q}_f\tilde{\phi}_0(\boldsymbol{q}_f)J_\ell\left(\boldsymbol{\alpha}_0\cdot\boldsymbol{q}_f,\frac{U_p}{2\omega}\right) \tag{2.44}$$

and $\tilde{\phi}_0(\boldsymbol{q}(\ell))$ the Fourier transform of the initial atomic state ϕ_0:

$$\tilde{\phi}_0(\boldsymbol{q}) = \frac{1}{(2\pi)^{3/2}}\int d\boldsymbol{r}e^{-i\boldsymbol{q}\cdot\boldsymbol{r}}\phi_0(\boldsymbol{r}). \tag{2.45}$$

The energy conservation implicit in equation 2.43 is

$$\frac{q_f^2}{2} + U_p + \ell\omega = \omega_\gamma - E_b. \tag{2.46}$$

With the $(2\pi)^{-3/2}$ normalization chosen for the Volkov waves, the relation between the transition matrix element and the scattering amplitude is

$$f_{fi}(\ell) = (2\pi)^2 T_{fi}(\ell). \tag{2.47}$$

The differential cross-section $d\sigma/d\Omega = (q_f/q_i)|f|^2$ with $q_i = q_f(\ell = 0)$ is

$$\frac{d\sigma(\ell)}{d\Omega} = \frac{q_f}{q_i}\frac{(2\pi)^4}{4}\left|\boldsymbol{A}_{0,\gamma}\cdot\boldsymbol{q}_f\tilde{\phi}_0(\boldsymbol{q}_f)J_\ell\left(\boldsymbol{\alpha}_0\cdot\boldsymbol{q}_f,\frac{U_p}{2\omega}\right)\right|^2. \tag{2.48}$$

The total cross-section in the ℓth channel is obtained by integration over the angular variables, $\sigma(\ell) = \int d\Omega q_f/q_i|f|^2$.

To the extent that the dependence of $\boldsymbol{q}_f$ on ℓ can be neglected, equation 2.48 reduces to

$$\frac{d\sigma(\ell)}{d\Omega} = J_\ell^2\left(\boldsymbol{\alpha}_0\cdot\boldsymbol{q}_f,\frac{U_p}{2\omega}\right)\frac{d\sigma}{d\Omega}, \tag{2.49}$$

with $d\sigma/d\Omega$ as the laser field-free differential photoionization cross-section. This result is similar to the result expressed by equation 2.34 for laser-assisted scattering.

The typical signature of the presence of an assisting laser field is the square of a Bessel function. From equation 2.49 it is possible to obtain an approximate expression for the differential probability that the photoelectric effect is accompanied by the exchange of n laser photons

$$\frac{dP_n}{d\Omega} = \frac{d\sigma(n)}{\sum_\ell d\sigma(\ell)} = J_n^2\left(\boldsymbol{\alpha}_0 \cdot \boldsymbol{q}_f, \frac{U_p}{2\omega}\right), \tag{2.50}$$

where the summation formula, equation 2.30, together with the result $J_0(0,0) = 1$ was used.

If the dependence of $\boldsymbol{q}_f$ on the number of exchanged photons is retained, the results are more involved. As an example, consider the probability that the photoelectric effect is accompanied by the exchange of n laser photons

$$P_n = \frac{\sigma(n)}{\sum_\ell \sigma(\ell)}. \tag{2.51}$$

Assuming that the main effect of the assisting field is to redistribute the probability current into different photon-exchange channels, it is possible to approximate the sum $\sum_\ell \sigma(\ell)$ by the total field-free cross-section σ_{FF} and use $P_n = \sigma(n)/\sigma_{FF}$ to obtain the probability. In this approach, the influence of the laser field A on the initial state, as well as the influence of the sample potential ϕ on the final continuum state, are neglected. The former is justified even for weakly bound systems as long as ϕ is a short-range potential [74], while the latter holds in the soft photon limit. Thus, the ratio of the laser-assisted and the field-free photoemission cross-section can be derived [70] as follows:

$$P_n = \frac{d\sigma(n)/d\Omega}{d\sigma/d\Omega} = J_n^2\left(\boldsymbol{\alpha}_0 \cdot \boldsymbol{q}_f, \frac{U_p}{2\omega}\right) \approx J_n^2\Big(\boldsymbol{\alpha}_0 \cdot \boldsymbol{q}_f\Big) \tag{2.52}$$

In the approximation of equation 2.52 the ponderomotive potential is neglected. As is the case in the soft photon limit, the target atom properties cancel and the prob-

ability depends only on the electron and laser field properties. It is therefore expected that, to the extent that the soft photon limit approximation is justified, the target properties are negligible.

In summary, the laser-assisted photoelectric effect can be considered to result from "dressing" of the free-electron wave function. When an electron is photoejected in the presence of an intense laser field, the electron is accelerated by the laser field. If the interaction occurs continuously over several optical cycles, the electron undergoes oscillations. This leads to ponderomotive energy shifts, and, in the presence of atomic nuclei or solids that can absorb momentum, to the generation of sidebands in the photoelectron spectrum. The appearance of sidebands corresponds to the absorption and stimulated emission of photons from the laser field.

Chapter 3

Experimental Setup

3.1 Introduction

The dynamics of an electronic excitation and the following relaxation process can be followed directly by using the pump-probe technique. Experimentally, this is realized by controlling the time delay between the pump and probe pulses: A first laser pulse (pump) excites the system under investigation and a second time delayed pulse (probe) samples the excited state of the system. By varying this time delay after a spectrum has been acquired, it becomes possible to follow the temporal evolution of the excitation process and its subsequent relaxation into the steady state. With the availability of fs-laser and HHG photons, a whole range of time-resolved techniques have become available. As photoemission samples electronic states, time-resolved x-ray photoelectron spectroscopy is able to sample the evolution of excited states above the Fermi level and in some cases laser induced changes at the core levels.

The time-resolved EUV photoemission spectrometer that we have used for our experiments (see figure 3.1) consists of two major components - an ultra-high vacuum (UHV) chamber and the EUV and IR beamlines.

3.2 EUV and IR Beamlines

The laser system used for these experiments is a commercial multipass Ti:sapphire amplifier (KM Labs "Dragon"). At an energy per pulse of 2 mJ and a repetition rate

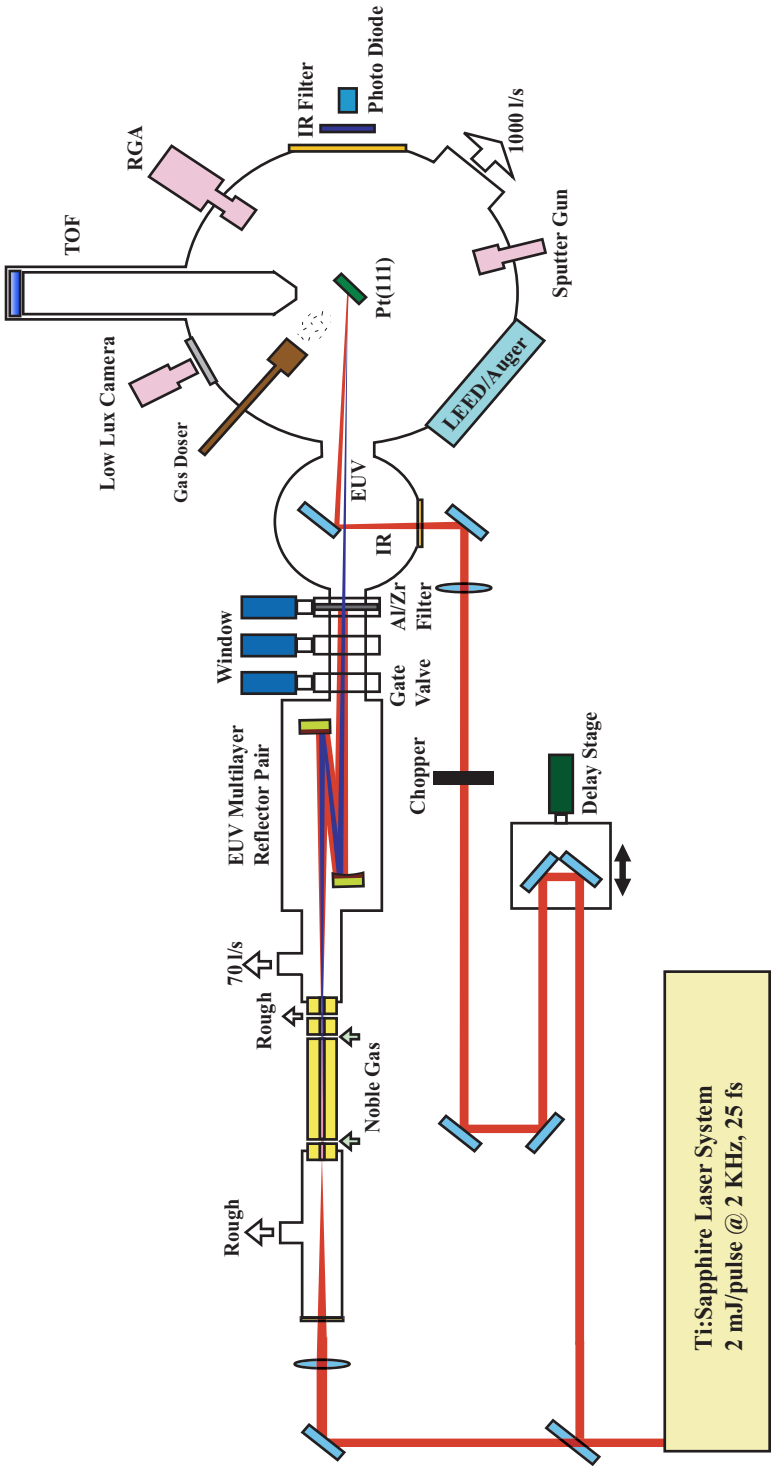

Figure 3.1: Experimental setup for observing the laser-assisted photoelectric effect from surfaces.

of 2 kHz, this laser produces 25 fs pulses with a central wavelength of 780 nm. The laser beam is directed through a beam splitter, which separates the beam into two. Depending on the experiment approximately 10 - 30 % of the energy is used for the IR beam, while the remaining energy is used for the EUV beam. Since in this thesis a number of experiments using different EUV and IR wavelengths are discussed, each will be examined separately.

3.2.1 IR beamline

The IR beam (10 - 30% of the laser energy) is directed through a computer-controlled delay stage in order to control the time delay between EUV and IR pulses. These pulses are then loosely focus into the UHV chamber and subsequently redirected to the sample at a small ($\approx 1^\circ$) angle with respect to the EUV beam. The IR beam spot size at the sample is varied between 0.2 and 1.2 mm by moving a focusing lens. The IR beam is chopped at a frequency of 1 kHz, and the electron detector is gated to record EUV+IR and EUV-only spectra alternately. This allows us to distinguish emission caused solely by the IR beam from two-color (EUV+IR) photoemission.

Furthermore, in order to experimentally verify the wavelength dependence of laser-assisted photoemission, we performed experiments with two different IR wavelengths:

- 780 nm: Chapters 4 and 5 discuss experiments where the IR wavelength is 780 nm (the fundamental frequency of the laser system). In these experiments, the IR pulse duration is broadened to 35 - 40 fs by dispersion as it propagates through various optical elements in the delay line.

- 1300 nm: The experiment discussed in chapter 6 studies the dependence of the LAPE sideband height for different IR wavelengths. We used an optical parametric amplifier (OPA) [79] to convert the 780 nm light into 1300 nm light.

In this experiment, the pulse duration of the IR beam is ≈ 90 fs.

3.2.2 EUV beamline

The remaining 70 - 90 % laser energy is up-converted by phase matched high-harmonic generation (see section 2.1) in a noble gas-filled, hollow waveguide [66] (see figure 3.2). Just as with the IR beam, the experiments discussed below make use of the two different EUV energies:

- 43 eV (27^{th} harmonic, 29 nm): In this case, Argon is the noble gas used to efficiently generate this photon energy through HHG. The argon pressure inside the hollow waveguide is ≈ 45 torr. This photon energy was used for the experiments discussed in chapters 4 and 6.

- 91 eV (57^{th} harmonic, 13.5 nm): ≈ 500 torr of Helium is used to generate this photon energy. The experiment covered in chapter 5 makes use of this photon energy.

Figure 3.2: Picture of a HHG waveguide v-groove holder engineered by the Kapteyn-Murnane group.

Since HHG produces a semi-continuum spectrum, frequency discrimination is needed in order to use the HHG photons for photoemission. In our experiments, we

use a pair of multilayer mirrors [80], one flat and one curved, to spectrally select the desired harmonic and to focus the EUV beam onto the Pt surface with a spot size of approximately 100 μm. For the 43 eV photons, this pair of multilayer mirrors is made by periodically growing magnesium and silicon carbide (silicon and molybdenum for the 91 eV photons) thin-films on a superpolished glass substrate to form a Bragg reflector for the incoming photons. The wavelength with the maximum reflectivity is equal to twice the thickness of the Mg:SiC (Si:Mo) stack of the multilayer mirrors. Figure 3.3 shows the reflectivity vs wavelength plot of a single Mg:SiC multilayer mirror. The wavelength of the maximum reflectivity of the multilayer mirror is near the 27^{th} harmonic of the driving 780 nm pulse. Figure 3.4 shows the reflectivity curve for a Si:Mo multilayer mirror. Experimentally the photon flux at the 27^{th} harmonic is higher than at the 57^{th} harmonic; however, the multilayer mirrors for the shorter wavelength photons have higher reflectivity.

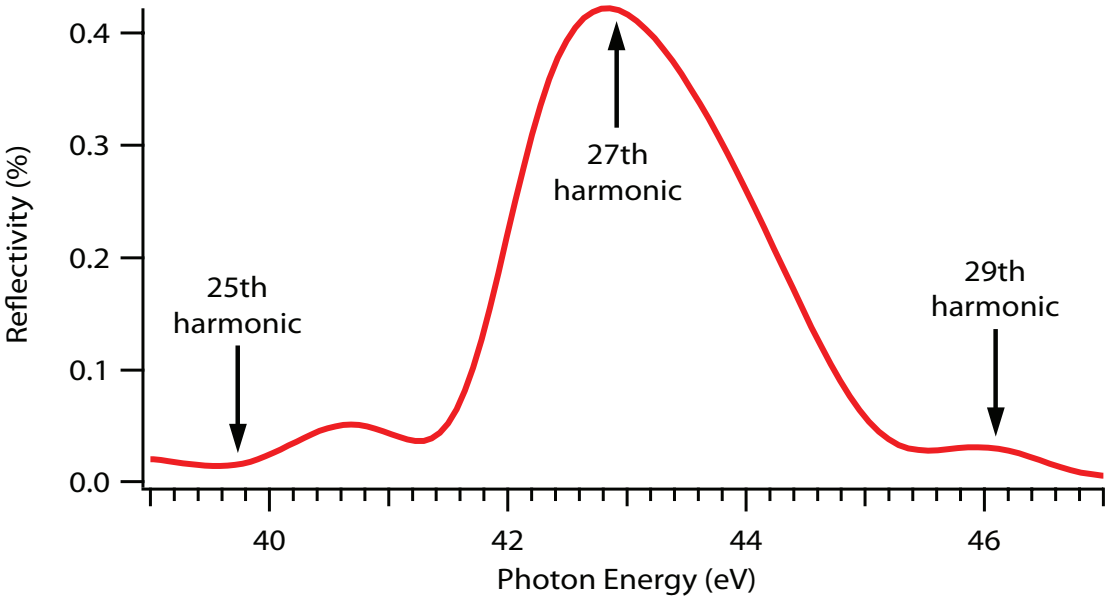

Figure 3.3: Reflectivity curve for a single Mg:SiC multilayer mirror.

Additionally, a 200 nm thick aluminum or zirconium filter is used to maintain a pressure differential between the high-order harmonic generation cell and the UHV

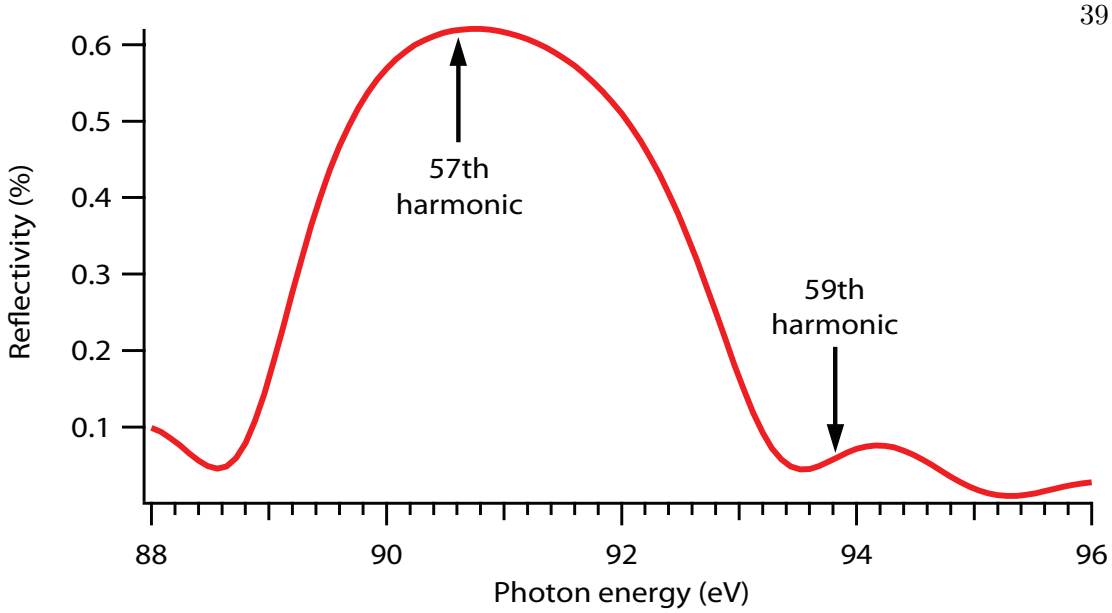

Figure 3.4: Reflectivity curve for a single Si:Mo multilayer mirror.

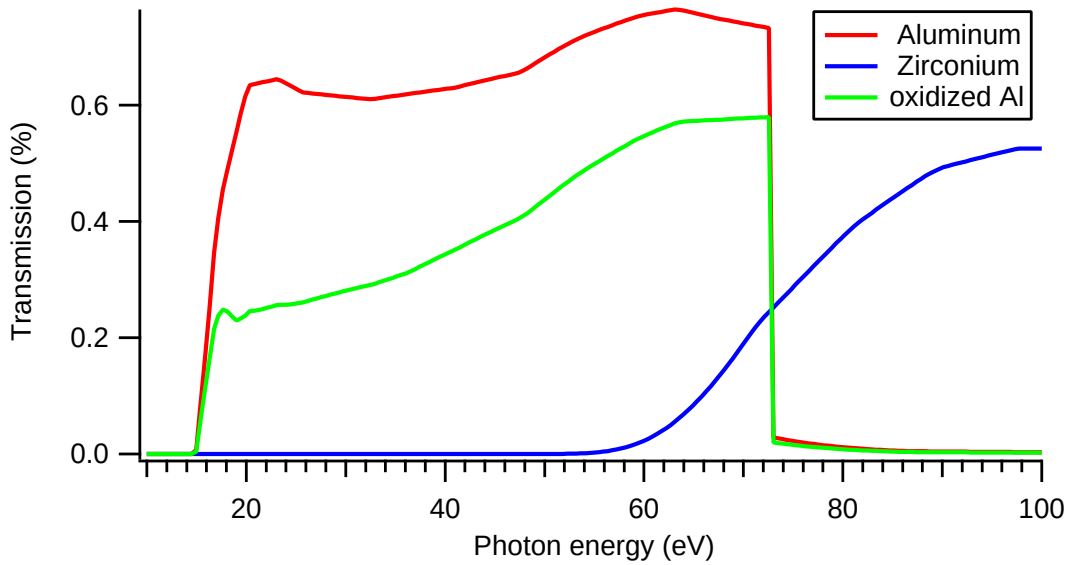

Figure 3.5: Transmission of the aluminum and zirconium filters. The green curve represents the transmission of an oxidized aluminum filter.

chamber, and to block the copropagating IR light while transmitting the EUV beam. The aluminum filter transmits the 43 eV photons, while the zirconium filter transmits the 91 eV light (see figure 3.5).

3.3 UHV Chamber

The UHV chamber is pumped by a 500 l/s turbo pump (Balzers TMU-520-SG) and a 270 l/s ion pump (Varian VacIon Plus 300 noble diode) to achieve a base vacuum pressure of under 1×10^{-10} mbar after a standard UHV bake out. To prevent the earth's magnetic field from penetrating into the vacuum chamber, the chamber is shielded internally by double layers of μ-metal. This prevents the course of photoelectrons from being distorted by external magnetic fields. A platinum(111) single crystal is mounted inside the chamber by spot-welding it onto two parallel tantalum heating wires, which are in turn spot-welded to a manipulator mounted vertically from the top port of the chamber (see figure 3.8). The manipulator has the capability of performing three-axis translational and azimuthal rotational motion with respect to the platinum sample. In addition, the manipulator's inner tube can be filled with liquid nitrogen, providing cooling for the sample.

A high current power supply (HP 6269B) is connected to the manipulator and drives the tantalum wires that heat the platinum sample. A proportional-integral-derivative (PID) temperature controller (Omega CN77000) controls this power supply. A K-type thermocouple is also spot-welded to the back of the platinum sample for measuring the sample's instantaneous temperature. The measured temperature feeds into the PID temperature controller as a feedback signal to control the high current power supply. Using this feedback control scheme, the electrical heating can be nicely balanced by the liquid nitrogen cooling; therefore, the sample temperature can be reliably controlled over a wide temperature range, from 79 to 1200 K, and the temperature can be increased or decreased at a rapid rate.

A custom-built, time-of-flight (TOF), electronic kinetic energy analyzer is used for detection (see Appendix B). Two shielding layers of μ-metal are installed around the inner wall of the TOF tube to insulate it from the earth's magnetic field. The total tube

length is $L_{tube} = 600$ mm and the inner diameter is 40 mm, which provides an electron collection solid angle of $S \simeq 2\times10^{-3}$ sterradians. At the end of the TOF tube, a custom-built, large area (40 mm), fast-response detector detects the electrons. A double micro-channel plate (MCP) is used at the front of the detector to obtain the gain necessary to detect single electrons. The MCPs amplify the single electron signal to detectable signal levels ($\sim$ 100 mV) by a secondary electron cascade process . The detector has timing resolution of about 200 ps. Impedance matching of the whole electron detector allows it to operate with a GHz frequency bandwidth. The key ideas of impedance matching are adapted from the design of A. Stolow [81], and a cone-shape anode design ensures that the fast electronic signal propagates into the coaxial cable with no noticeable reflection. The output signal is subsequently delivered to a high frequency pre-amplifier, followed by a constant fraction discriminator (ORTEC 9327), ensuring that the electron arrival time is independent of output signal intensity fluctuations. An all solid-state time-to-digital converter (TDC) (ACAM AM-F1) measures the electron flight times, referenced to a start signal from the laser system.

The real electron flight time is actually referenced to the moment when the EUV pulse arrives at the sample, also the moment when the sample starts to emit electrons. This moment appears on the TOF spectrum as an EUV scattered light peak. The peak is a result of the EUV pulse being scattered/reflected from the sample surface, with the scattered EUV light then triggering the detector. There is a 2 ns time delay between this EUV peak and the real start time, resulting from the propagation of the EUV light from the sample to the detector. This time difference is negligible since the fastest photoelectrons need more than 150 ns to reach the detector. By subtracting the time of the EUV start peak from the measured flight time, the actual electron kinetic energy E_{kin} can be calculated (see Appendix B).

As shown in figure 3.6, the EUV and IR beams irradiate the sample at a variable angle θ with respect to the surface normal. In order to prevent light reflected off the

sample from hitting the detector, the TOF tube is tilted up with respect to the plane of incidence by an angle of 20°. Consequently the observation angle ϕ with respect to the surface normal is given by $\cos\phi = \cos 20° \cos(90 - \theta)$.

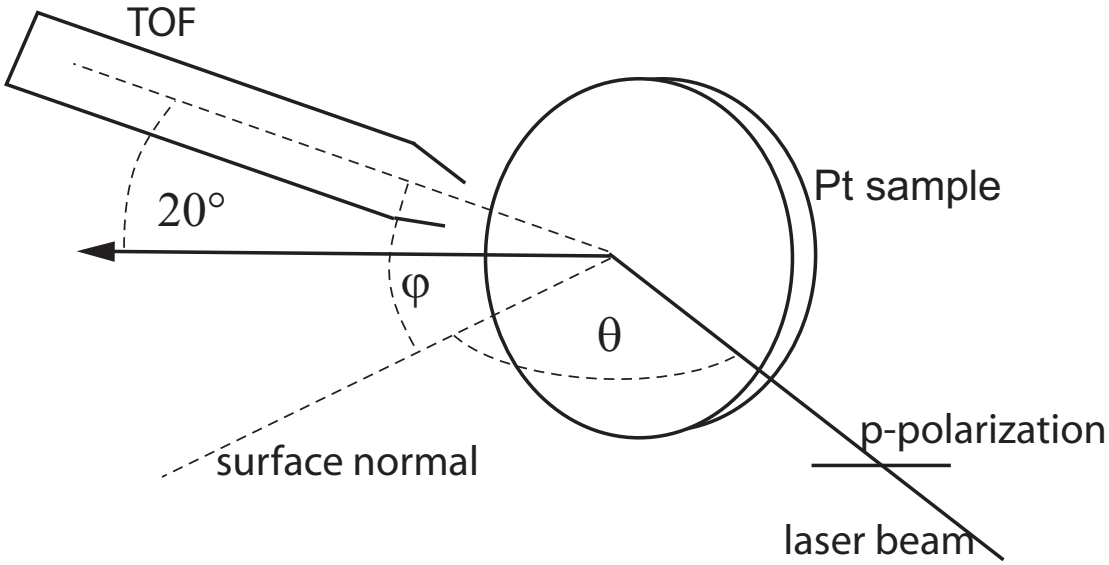

Figure 3.6: Geometry for the photoemission measurements: p-polarized IR light impinges on the Pt sample at an angle θ with respect to the surface normal. $\vartheta = 90 - \theta$ is the angle of the polarization vector with respect to the surface normal. The detector is titled by 20° with respect to the plane of incidence. The corresponding observation angle ϑ with respect to the surface normal is given by $\cos\phi = \cos 20° \cos\vartheta$.

For standard surface diagnostics, the UHV chamber is equipped with a Low Energy Electron Diffraction (LEED) Spectrometer and an Auger Electron Spectrometer (AES) (OCI BDL800IR), which monitor the condition of the sample's surface. The diffraction pattern of the LEED can reveal the local order of the sample surface, while surface contamination can be seen using the AES. A residual gas analyzer (RGA) (Leybold Inficon Transpector) is installed on the UHV chamber for monitoring the ambient chamber gas content. In addition, Thermal Desorption Spectra (TDS) [82] can be taken by the RGA, measuring the partial pressure of a target molecule while the temperature of the sample is steadily raised.

3.4 Sample Preparation

For sample preparation and cleaning, an argon ion sputter gun is installed in the UHV main chamber. The sputter gun can be used to remove the topmost several mono-layers of the platinum sample, and therefore sample surface contaminations are simultaneously removed. Rapid thermal annealing can subsequently be performed to reconstruct the surface order. However, on a day to day basis, we usually obtain a thermal desorption spectrum of oxygen adsorbed on Pt(111) to assess the cleanliness of the sample.

Thermal desorption spectroscopy is a well-known and commonly used technique for characterizing chemical reaction processes on surfaces. The idea of TDS is to adsorb the molecules under study to the metal surface at a low, non-reactive temperature. The temperature of the metal surface is subsequently increased at a constant rate to a temperature well above the temperature where the adsorbates react and desorb. By measuring the yield of the desorbing molecular species and the corresponding desorbing temperatures, information about adsorption energy of the adsorbates, activation energy, and the reaction channels of the chemical reactions can be extracted. For oxygen on platinum (111), TDS can help us understand the oxygen chemisorbed states and their corresponding properties.

Figure 3.7 shows the TDS spectrum of O_2 on Pt(111) taken using our setup. Oxygen was initially dosed onto the platinum sample at 77 K, to saturation coverage. Two distinct desorption peaks can be observed in the TDS spectrum: an intense α-O_2 peak at 145 K, and a weaker high temperature β-O_2 peak (the symbols of α and β are used for identification purposes only; the oxygen molecules desorbing from these two peaks are the same). The TDS spectrum of O_2/Pt can be explained by superoxo oxygen (O_2^-) dominating at the bridge site at high coverage, when oxygen is dosed to full coverage at liquid nitrogen temperature. When the surface temperature is heated

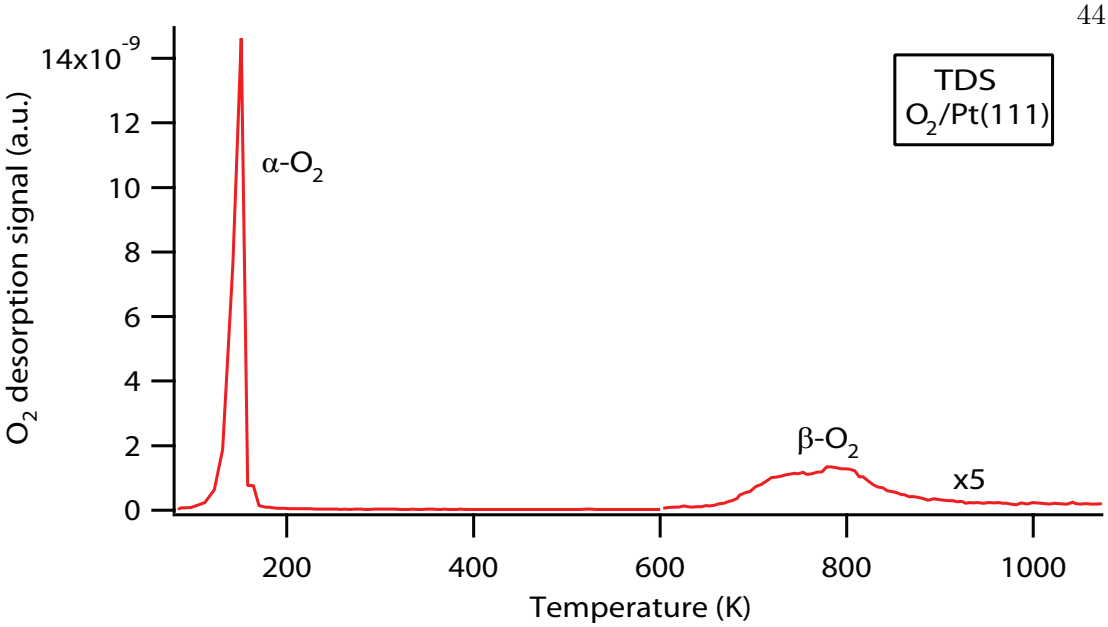

Figure 3.7: TDS for Pt(111) covered with O_2. The rate of temperature increase is 5 K/sec.

above 145 K, a large fraction of oxygen molecules desorb from the platinum surface, since the oxygen molecules have gained enough energy to overcome the energy barrier for desorption. Once some of the oxygen molecules desorb, the oxygen coverage becomes much lower on the platinum surface, and there will not be enough oxygen molecules left on the surface to cluster at adjacent bridge sites. The oxygen molecules now tend to move from the bridge site to the three-fold hollow sites to lower their total energy, leading to a state transition from the superoxo (O_2^-) into the peroxo (O_2^{2-}) state for the remaining oxygen molecules. When the surface temperature increases above 200 K, the intermolecular bond of the adsorbed oxygen molecule will gain enough energy to be broken. This causes the oxygen molecule to dissociate into two identical oxygen atoms, and the two oxygen atoms absorb on two different three-fold hollow sites on a platinum surface. Since atomic oxygen has a much higher adsorption energy, it will remain on the platinum surface until the surface temperature reaches temperatures higher than 600 K. Finally, the atomic oxygen will desorb and recombine to form oxygen molecules

and leave the platinum surface.

In our experimental setup we use a custom-built gas doser for precision gas dosing. The major benefit of using a gas doser versus using a gas leak valve is that a doser allows a much higher local pressure to be created around the sample area while keeping the rest of the chamber in high vacuum. This also minimizes the opportunity for gas molecules to adsorb at the UHV main chamber wall, preventing prolonged pump down times after gas dosing. In addition, if experimentally required, continuous gas dosing to the sample would not cause serious problems. Maintaining the high vacuum condition of the rest of the system is needed to ensure the functionality of other highly sensitive equipment. For example, the working pressure of the MCP electronic detector must be lower than 1×10^{-6} mbar.

3.5 Finding Temporal and Spatial Overlap

The spatial and temporal overlap between the EUV and the IR beams at the sample is obtained using a multi-step procedure. A preliminary spatial overlap is obtained by moving the sample holder (figure 3.8) so that the EUV and IR beams hit a phosphor screen that is moved in place of the Pt(111) surface. The beams are observed and aligned using a CCD camera that images the phosphor from outside the chamber.

The temporal overlap is obtained by moving the sample holder to another position, where the beams pass through a beta barium borate (β-barium borate, BBO), frequency-doubling crystal. The aluminum filter in the EUV beamline is replaced by a thin (0.355 mm) sapphire window to allow the IR light from the high-harmonic EUV beamline into the UHV chamber. A cross-correlation between the two IR fields then locates time zero. The position of time zero must be corrected for the sapphire window group delay, which is 934 fs. At this point, the Pt(111) sample is moved into place. Since the position of the phosphor screen along the light direction is not exactly the same as the Pt(111) sample, the spatial overlap must be readjusted. This is done using LAPE

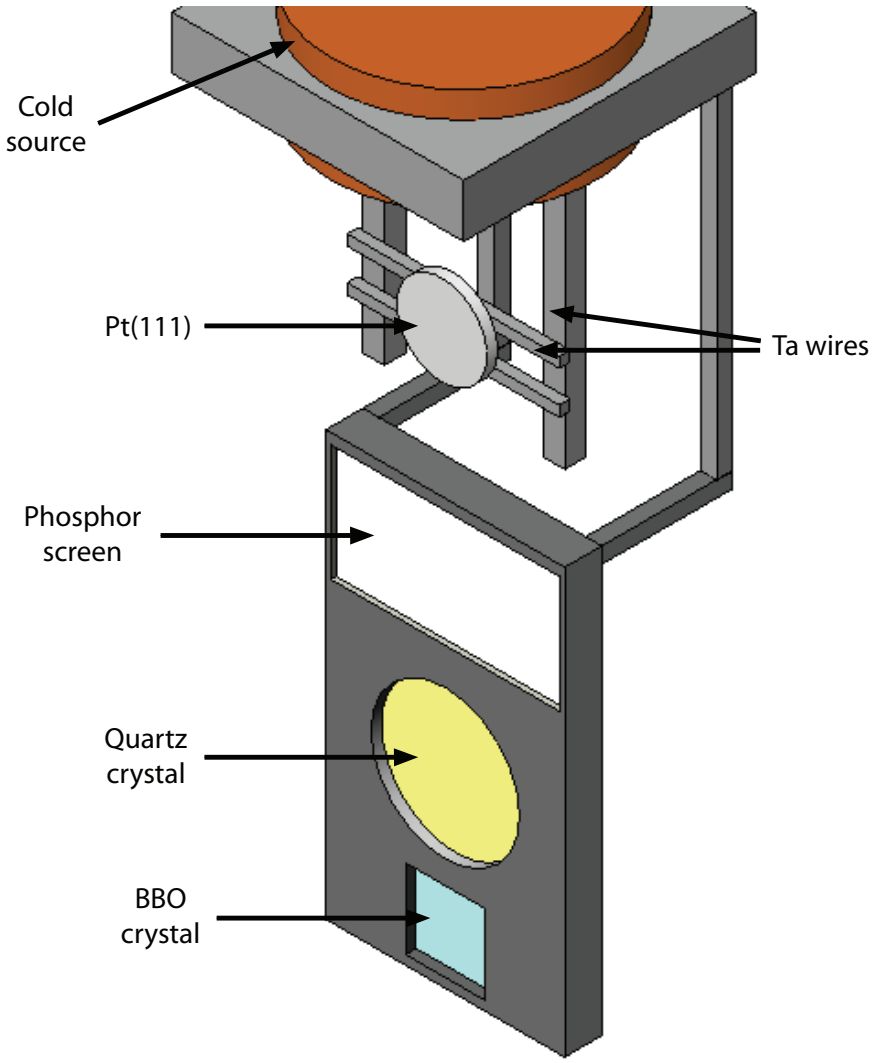

Figure 3.8: Schematic of the phosphor screen, Pt(111), BBO and quartz crystals holder.

(see section 4.4) itself, by observing the highest-energy photoelectrons as a measure of spatial and temporal overlap.

However, the above mentioned procedure can only be used for experiments where 780 nm light is used for the IR beam. In the experiments from chapter 6 we used 1300 nm light to "dress" the electrons photoemitted by the EUV light. Therefore, the method described above on how to find temporal overlap cannot be used. Instead we made use of the optical Kerr effect [83].

The optical Kerr effect is a change in the refractive index of a material in response to an electric field. In our case, the electric field is due to the light itself. It is distinct from the Pockels effect in that the induced index change is directly proportional to the square of the electric field instead of to the magnitude of the field. Under the influence of the applied field, the material becomes birefringent, with different indices of refraction for light polarized parallel to or perpendicular to the applied field. The difference in index of refraction, Δn, is given by

$$\Delta n = n_{\parallel} - n_{\perp} = KE^2\lambda_0 \tag{3.1}$$

where λ_0 is the wavelength of the light, K is the Kerr constant, E is the amplitude of the electric field, $n_{\parallel}$ is the index of refraction in the direction of the applied, and $n_{\perp}$ is the index at right angles to $\boldsymbol{E}$. This difference in index of refraction causes the material to act like a waveplate when light is incident on it in a direction perpendicular to the electric field. If the material is placed between two "crossed" (perpendicular) linear polarizers, no light will be transmitted when the electric field is turned off, while nearly all of the light will be transmitted for some optimum value of the electric field. Higher values of the Kerr constant allow complete transmission to be achieved with a smaller applied electric field. This effect only becomes significant with very intense beams such as those from ultrafast lasers.

In order to find time zero through the optical Kerr effect, we move the sample holder to a position where both beams pass through a quartz crystal. We place two "crossed" polarizers in the probe 1300 nm beamline, while we set the pump 780 nm light polarization at 45° from the probe light polarization (figure 3.9). We then monitor the intensity of the probe beam while changing the optical path-length of the pump beamline. When both pulses hit the quartz crystal at the same time, the intensity of the probe beam after the second polarizer increases. A measurement of the probe

light intensity versus time locates temporal overlap between both pulses. As mentioned before, in order to find time zero between the EUV pulse and the 1300 nm pulse, we need to correct for the delay induced by the sapphire window.

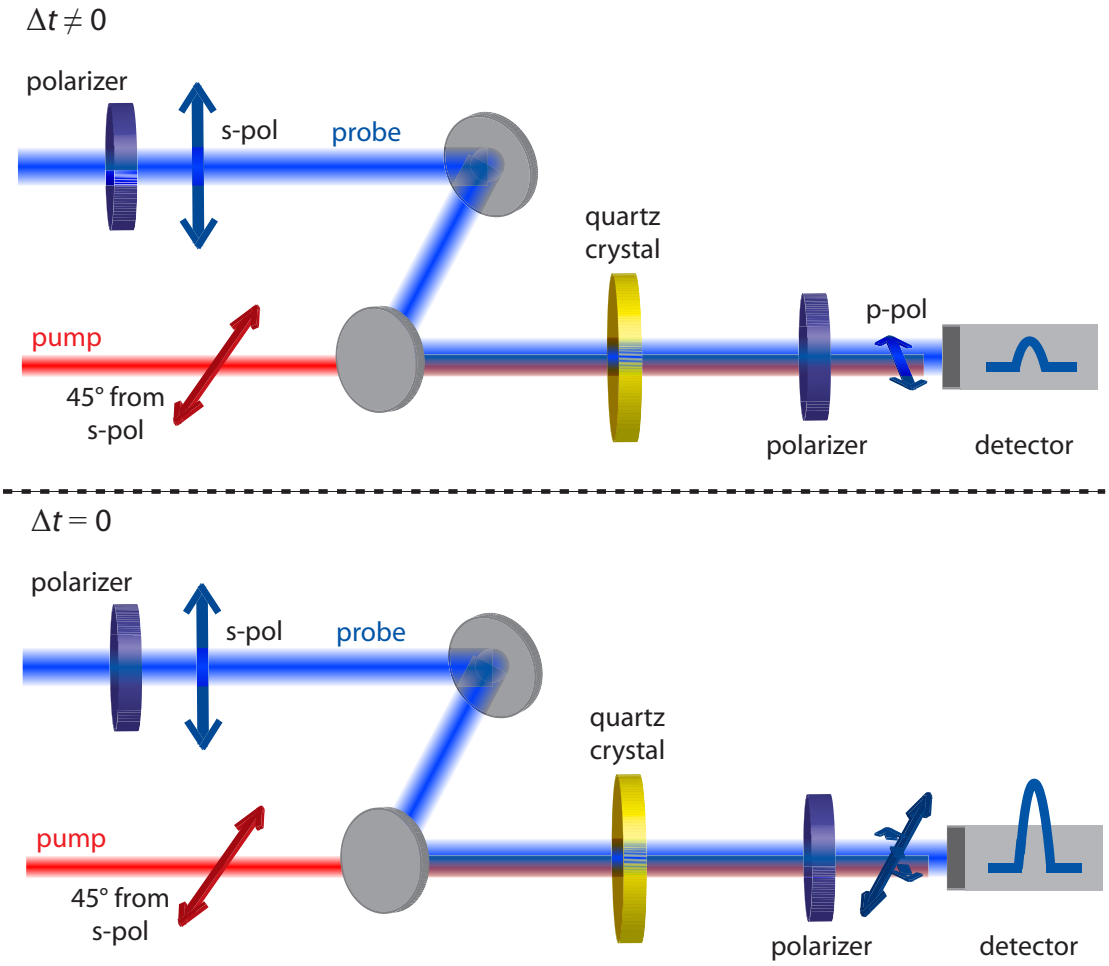

Figure 3.9: Schematic of experimental setup for finding temporal overlap when the IR pulse wavelength is different than 780 nm. In this case we use of the optical Kerr effect to find time zero.

Chapter 4

Laser-Assisted Photoemission from Surfaces

4.1 Introduction

The purpose of this chapter is to extract from EUV+IR photoemission data unambiguous signatures of all the processes that occur when a surface is illuminated simultaneously with an EUV and intense IR fields, i.e. above-threshold photoemission, heating of the valence electron distribution, and LAPE. Above-threshold photoemission and hot electrons are so-called *initial state* effects (i.e. signal originates from atoms that have not interacted with the EUV light), whereas LAPE is a *final state* effect in that it is specific to the EUV-excited atoms. Comparing the relative magnitudes of these effects allows us to develop methods to single-out the continuum free-free transitions corresponding to LAPE. We found that LAPE is the dominant process over a wide range of IR intensities and polarizations typically employed in experiments investigating charge-transfer dynamics in surfaces and surface-adsorbate systems. This result shows the feasibility of extending the variety of time-resolved measurements using LAPE that have been observed and employed in atomic and molecular samples, to solid surfaces.

4.2 Aspects of Surface LAPE

In principle, the concept of the laser-assisted photoelectric effect should apply not only to atoms but to solid surfaces as well. It should also result in the convolution of sideband shifts onto the entire continuous EUV photoemission spectrum from the

solid. However, due to the manifold different excitation paths and energy dissipation channels, the interpretation of energy shifts in the photoemission spectra from solid surfaces is more complicated than in the gas phase. The following sections discuss possible influences of the strong IR light on the photoemission spectra from solids.

4.2.1 Momentum conservation and ground state dispersion

A basic difference between photoemission from crystal surfaces, when compared to photoemission from atoms, concerns the exchange of momentum. This is restricted to integer multiples of the reciprocal lattice vector $\hbar \boldsymbol{G}$ in a crystal, due to the periodicity of the lattice. However, the presence of a surface removes the periodicity in one half-space and softens momentum conservation. In the case of EUV photoemission, the electrons have a very short escape depth on the order of 5 Å, according to the universal curve [12, 84]. They thus sense only one or two atomic layers. The surface can then act as a continuous source or sink of momentum normal to the surface [85], and the electron can be excited into a surface state, often called inverse LEED state. Along the surface normal, the latter is essentially a plane wave. For an IR laser pulse impinging on a metal surface, the electric field components parallel to the surface nearly vanish because of the boundary conditions. The remaining field, i.e. the component that is able to dress the photoemitted electrons, thus points along the surface normal, where the surface can balance momentum conservation. In this direction, the interaction of the emitted electron with the IR laser can be described by replacing the plane wave part of the LEED final state by a Volkov wave.

However in EUV photoemission, part of the spectrum arises from direct transitions, e.g., the emission from *d*-bands into *s*-bands in transition metals. This photoemission process conserves the momentum $q_{\parallel}$ parallel to the surface. As the "dressing" is associated with a momentum change along the surface normal, the direction of emission of the electron is changed, except for electrons emitted normal to the surface.

For angle-resolved photoemission spectroscopy with infinite resolution, or laser-assisted photoemission, the detected sidebands stem from electrons emitted from different initial states and at slightly different angles compared with the electrons that did not lose or gain photons of energy $\hbar\omega$ from the IR field. Due to the dispersion of the valence bands in solids, the corresponding energies can be shifted leading to a deviation of the sideband energy spacing compared with the IR photon energy. However, in the soft photon limit, the relative momentum change associated with the exchange of a photon between the photoelectron and the IR field is small. At an observation angle of 45°, the absorption or emission of a 1.6 eV photon by a 36 eV electron leads to $\Delta k_{\parallel} = 0.05$ Å^{-1}, which is about 0.02 of the total Brillouin zone. The corresponding energy shift due to dispersion is at most 50 meV, which is significantly smaller than the IR photon energy (1.59 eV) and even below the energy resolution of our detector. Thus, we neglect these dispersion energy shifts in this work.

4.2.2 Resonant interband and intraband transitions

Another difference between atoms and surfaces is the quasi-free behavior of electrons in a band, due to the delocalization of the electrons from individual ions. At the Fermi edge of Pt, however, the energy spectrum is dominated by *d*-bands, which deviate significantly from the free-electron like *sp*-bands. Due to the strong localization of the *d*-electrons to the crystal ions, the *d*-bands are narrow and exhibit only low dispersion. They can be described in the tight binding approximation and resemble bound electrons in atoms [86]. Ground state dressing of the *d*-electrons is therefore neglected in the soft photon limit for the same reasons as in atoms [87]. For the broader *sp*-bands, the tight binding approximation does not hold. Although the electrons can move freely, they cannot respond to the IR light in the same way as electrons in the continuum. At low frequencies, the interaction of light with a metal is dominated by intraband absorption. In this process, which corresponds to the classical IR absorption picture,

electrons can absorb any photon energy from the IR field and are promoted into unoccupied levels above the Fermi edge. This mechanism thus only affects a small fraction of the electrons in a narrow window around the Fermi edge, and does not lead to sideband peaks. Moreover, resonant $k_{\parallel}$-conserving interband transitions are only possible in certain directions when energy and momentum conservation are fulfilled. Contrary to the case of continuum electrons, only absorption is possible from the ground state since stimulated emission is forbidden by the Pauli principle, as the lower lying states are filled. The presence of such resonant interband transitions should thus be visible by an enhancement of the positive sideband; i.e., conduction-band electrons can absorb photons from the laser field. The dependence of this contribution on the EUV+IR time delay should follow the lifetime of the intermediate states, which is approximately 100 fs for transition metals [88]. Both effects are not observed in our experiment.

4.2.3 Non-resonant interband transitions

Due to the high IR intensities applied in LAPE experiments, non-resonant IR interband transitions into virtual levels occur, which can serve as intermediate states for multiphoton ionization. Such transitions have been studied theoretically in atoms in different limiting cases. For electrons in excited Rydberg states of atoms, non-resonant absorption and emission of microwave photons into virtual states can lead to dressing analogous to the continuum [89]. As unoccupied real levels above and below the initial Rydberg state are densely spaced, both absorption and emission are equally likely, which leads to symmetric sidebands. For electrons in an atomic ground state, symmetric sidebands can occur when the photon energy of the dressing beam is considerably smaller than the spacing between the atomic levels. In this case, which is usually fulfilled only for light in the far IR or microwave region, the distance of the virtual states after absorption and emission are approximately equally spaced from the closest unoccupied level [90].

In our experiment, the electrons are in the ground state and the photon energy is not resonant with any direct interband transition on a Pt(111) surface. Non-resonant absorption is closer to resonance with an unoccupied real state than stimulated emission, since unoccupied levels are only available above the ground state. Dressing of the ground state is thus expected to preferentially enhance the positive sideband leading to asymmetric amplitudes. In the light-metal interaction volume, however, the electron number reaches the same order of magnitude as the number of photons per pulse applied in our experiment. As a consequence, only a very small fraction of the electrons is excited into the virtual states, leading only to a negligible contribution to the positive sideband in the EUV photoemission spectrum. This is in contrast to gaseous atoms where the atom density is usually much lower than the photon density. In the case of dressing of the final state, only the small number of photoemitted electrons plays a role - so that in the continuum a significant fraction of the electrons can be dressed.

4.2.4 Dressed band structure

Theoretical investigations of intense field effects in solids predict the opening of band gaps [91, 92] whenever direct multiphoton transitions are possible. These band gaps are closely related to the intensity-dependent Autler-Townes splitting [93] of atomic levels in the presence of a resonant or near-resonant strong laser beam. At a photon energy of 1.6 eV, the laser is not resonant with any direct interband transition [94], so that ground state dressing is expected to play a minor role in our experiment. The strong IR laser thus influences the electrons only after photoemission, leading to the final state dressing picture similar to the experiments done in gaseous atoms.

4.2.5 Competing strong field effects

For applications of LAPE in EUV pulse duration measurements, the sideband amplitude range, after equation 2.50 $A_n = J_n^2(x)$ for small values of the argument x, is

of special interest. In SI units x can be written as

$$x = \sqrt{\frac{16\pi\alpha}{m_e\hbar}\frac{IE_{\mathrm{kin}}}{\omega_{\mathrm{IR}}^4}}\ . \tag{4.1}$$

For small x, A_1 can be approximated by $A_1 \approx x^2/4$ leading to

$$A_1 \propto \frac{IE_{\mathrm{kin}}}{\omega_{\mathrm{IR}}^4}. \tag{4.2}$$

In this regime, the sideband height depends linearly on the IR laser intensity, which makes it a suitable observable for EUV+IR cross-correlation measurements as well as for time resolved spectroscopy. Additionally, A_1 depends on the kinetic energy E_{kin} of the dressed electron and on the IR photon energy ω_{IR}. Figure 4.1 shows the intensity required to generate 1st-order sideband amplitudes of $A_1 = 0.1$ versus the photoelectrons kinetic energies E_{kin} for 800 nm light. For kinetic energies below 100 eV, an intensity of at least 10^{11} W/cm^2 is necessary. For slower electrons, the required intensity increases dramatically. This intensity range is only 1 to 2 orders of magnitude below the damage threshold of metal surfaces. Also, the excitation of non-thermal hot electrons leads to changes in the spectra similar to those caused by the photoelectric effect. Finally, the illumination of metal surfaces at such high intensities leads to significantly stronger electron emission and higher kinetic energies than from gaseous atoms, due to field enhancement and space-charge-induced Coulomb explosion.

In past work, it was shown that above-threshold photoemission (ATP) can be significant from surfaces at much lower laser intensities than in atoms, due to field enhancement effects [95]. Above-threshold photoemission is the photoemission of electrons from a surface by absorption of more photons than is required to overcome the work function. This effect can be understood, similar to LAPE, by the rate-limiting multi-photon ionization of the sample through absorption of the minimum number of photons needed, and followed by redistribution of these electrons in the continuum by

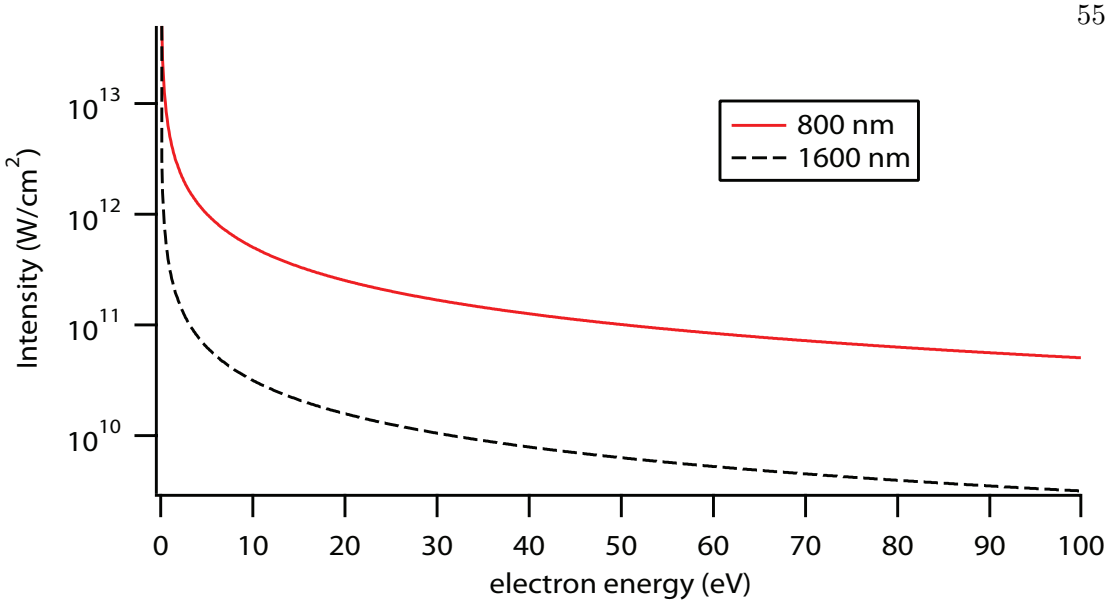

Figure 4.1: Calculated IR intensity required to generate first order sideband heights of A_1=0.1 for wavelengths of 800 nm and 1600 nm, respectively, as a function of the kinetic energy of the electrons. For kinetic electron energies of 36 eV and an 800 nm dressing wavelength, laser intensities greater than 10^{11} W/cm^2 are required.

absorption of additional photons [96]. For ultrashort Ti:sapphire laser pulses at 780 nm, intensities on the order of 10^{14} W/cm^2 are needed to cause a substantial emission of electrons by multiphoton ionization of gaseous atoms; i.e. above-threshold ionization. However, it has been known for a long time that surface plasmons can lead to substantial field enhancement (up to a factor of 10^3) corresponding to intensity enhancements of 10^6 on a metal surface [95]. This effect results in phenomena such as surface enhanced Raman scattering. Although forbidden by energy and momentum conservation on perfectly flat surfaces, these surface plasmons can be excited on rough surfaces. Due to the corresponding field enhancement, ATP can happen at intensities as low as 10^8 W/cm^2 [95]. These enhancements not only lead to higher kinetic energies of the ATP electrons from surfaces than the ATI electrons from atoms, but also the number of electrons is considerably larger. Additionally, the first step in ATP, multiphoton ionization, is stronger than in atoms, because of the low ionization potential (work function) of

atoms. Finally, the sample particle density is higher than in typical experiments on atoms. As a consequence, many electrons can be emitted from a very small volume of the solid sample by a single intense laser pulse, which leads to a Coulomb explosion as the electrons repel each other [35, 97]. This way, some of the electrons are accelerated and can gain a significant amount of extra kinetic energy, while others are decelerated and may not escape the surface. Surface preparation thus plays a major role in the ability to successfully observe LAPE.

4.3 Above-Threshold Photoemission

As was discussed above, the IR laser intensity at 800 nm required to generate sidebands is on the order of 10^{11} W/cm^2. Since the parallel component of the electric field nearly vanishes at the surface of a good conductor, the laser polarization must be perpendicular to the surface. Figure 4.2 shows a photoemission spectrum taken for p-polarized IR light as the laser intensity is varied around 10^{11} W/cm^2. No EUV light was incident in this measurement. Since the ponderomotive potential at these intensities is $<$0.1 eV and is much less than the work function of Pt (5.8 eV), no "channel-closing" occurs, and at least 4 IR photons are required to photoeject electrons from the surface. The lowest intensity curve shows multiphoton photoemission by 4 photons, with a small contribution of above-threshold photoemission by 5 photons. As the intensity is increased, two effects can be observed. First, above threshold photoemission becomes stronger. The 5-photon edge increases and new channels with 6 and 7 photons appear. However at higher laser intensities, the separation of subsequent edges is measurably larger than the IR photon energy. This occurs because the number of photoelectrons increases dramatically and leads to a Coulomb explosion of the electron cloud, due to their mutual repulsion [35]. As a result, faster electrons at the front of the cloud are accelerated, while slower electrons at the back are decelerated. This effect already becomes very strong at the moderate laser intensities applied here.

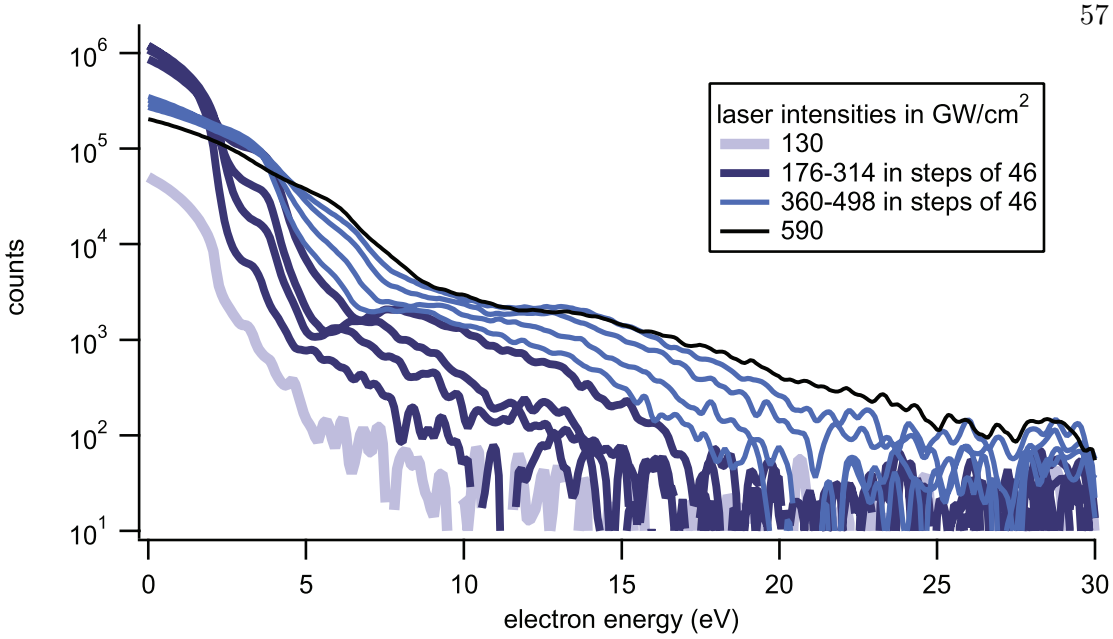

Figure 4.2: Multiphoton-induced photoemission spectra taken at different laser intensities ranging from 130 to 590 GW/cm^2 using IR light only. ATP (above threshold photoemission) and space-charge acceleration generate electrons with kinetic energies of tens of eV.

In contrast to experiments on gaseous samples, the higher target densities and lower ionization potentials in solids lead to stronger multiphoton ionization, above-threshold photoemission, and as a consequence, to stronger space-charge acceleration. To detect LAPE from solids with Ti:sapphire laser pulses at 800 nm, EUV photon energies of at least 30 to 40 eV are required so that the photoejected electrons corresponding to the Fermi edge have energy significantly higher than the IR-induced ATP electrons. However, even if the EUV photoelectron Fermi edge lies beyond the high energy ATP electrons, its shape can still be altered by the space-charge if too many IR-induced electrons are emitted. It is therefore important to reduce space-charge effects as much as possible.

The measurement shown here was performed on a sample that was cleaned as described before. This is necessary since any surface roughness can lead to strong local enhancements of the IR field at the surface [95], which dramatically increases the

number and energy of IR-ejected electrons. Due to the strong susceptibility of these effects to surface roughness, the IR-induced electron spectra differ strongly from day to day, and figure 4.2 can thus only be taken as an example. We observe the creation of hot spots on the Pt(111) surface resulting from IR laser intensities above 10^{12} W/cm^2 at pulse duration $\sim$ 30 fs. These hot spots result in a huge increase in high energy electrons resulting from the IR field. Apart from using shorter pulse durations to raise this damage threshold, the use of lower IR photon energy as the dressing field would help to circumvent this problem. In the present experiment, however, IR-induced electrons can be kept sufficiently low by thorough sample preparation and by restricting the IR laser intensity to moderate values.

4.4 Extraction of the Sideband Structure

As mentioned before, LAPE has been extensively studied in the gas phase, where the discrete nature of the photoelectron spectrum makes the sidebands easy to distinguish. To extract this peak-like sideband structure from the continuous spectra of solid surfaces, the EUV+IR spectrum must be deconvolved from the EUV-only spectrum using a fitting procedure. Figure 4.3 shows a series of photoelectron spectra around the Fermi edge, at an IR peak intensity on the order of 10^{11} W/cm^2 and for relative time delays between the IR and EUV beams ranging from -100 fs to +100 fs. Negative time delays denote that the EUV pulse arrives after the IR pulse. The IR beam was polarized in the plane of incidence (p-polarized). The EUV-only spectrum is only shown for the -100 fs measurement (dashed line). At this time delay, both the EUV-only, as well as the EUV+IR spectra, show the typical *d*-band structure of clean Pt(111). This Pt *d*-band peak near the Fermi edge, although 0.9 eV wide, is nevertheless a very useful characteristic peak around which to observe sidebands. While the spectral shape is unaffected by the presence of the IR field, the EUV+IR spectrum is slightly shifted to higher electron energies as compared to the EUV-only spectrum, due to the space-

charge induced Coulomb explosion. We have observed this space-charge-induced shift to be present for time delays between at least -1 ps and +1 ps. This can be explained by the fact that the photo-emitted electrons are traveling slowly enough that they do not escape from the range of the space-charge field of the IR-induced electron cloud during the time frame of the experiment. Thus, the EUV photoelectron energies are slightly shifted even when the IR pulse comes considerably after the EUV. This space-charge effect increases strongly with the IR intensity. At very high intensities it not only shifts the EUV+IR spectra, but also changes its shape (see e.g. figure 4.13). However in figure 4.3, the space-charge effect is rather low, indicating an effective IR intensity in the low 10^{11} W/cm^2 range. The space-charge shift is determined from the -100 fs curves and all EUV+IR spectra are corrected for it before subsequent analysis.

In the photoemission spectrum shown in figure 4.3 near that which corresponds to zero time delay between the laser and EUV pulses, we observe a very strong shape change at the Fermi edge. Insight into the origin of this change can be gained by calculating the average kinetic energy of the photoelectrons above 20 eV, both with and without the IR pulse present. (Below 20 eV photoelectron kinetic energies, the EUV+IR spectrum is dominated by low-energy electrons from above-threshold photoemission.) No significant IR-induced increase of the average kinetic energy was found around zero fs. Indeed, the calculated average photoelectron kinetic energies with and without the IR were identical, within 0.1 meV, at all time delays. This indicates an essentially equal redistribution of electrons to lower and to higher kinetic energies in the presence of the IR field that modifies the photoelectron spectra. Consquently, this result excludes interpretations of a photoelectron spectrum modified by image potential states, ground state dressing, or hot electrons [98], since in all cases the average kinetic energy should be increased by the presence of the IR field. We therefore interpret the Fermi edge modification near time zero to be the result of the laser-assisted photoelectric effect. Viewed in a perturbative two-step model, the electrons photo-emitted by the EUV beam can absorb

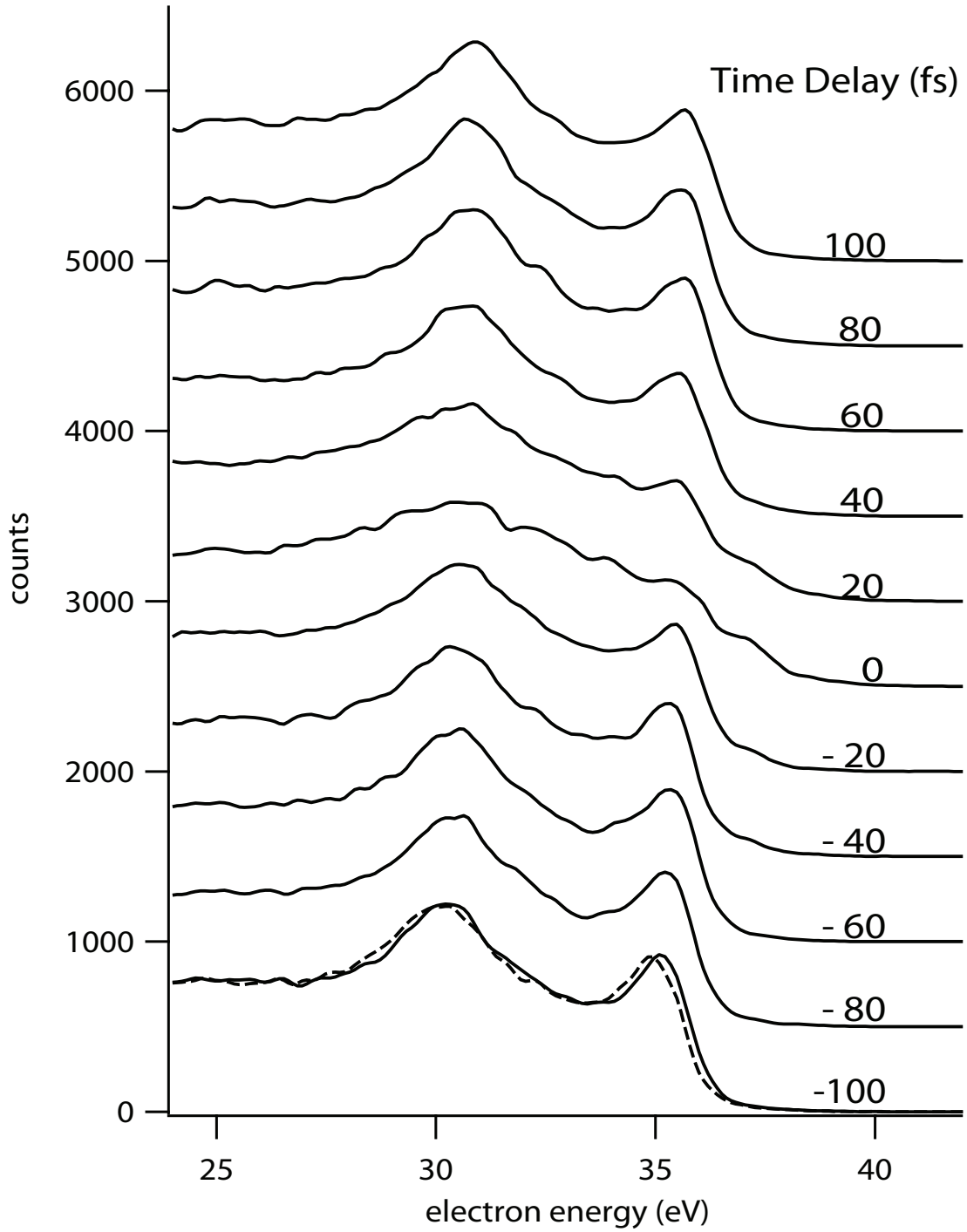

Figure 4.3: Observed photoelectron spectra from Pt(111) as a function of time-delay between the IR and EUV beams. For -100 fs time delays, the EUV-only spectrum (dashed line) is also shown. A slight shift of the spectrum due to IR-induced space-charge can be seen, but this does not change the shape of the spectrum and can thus be corrected for. The strong modification at the Fermi edge of the time zero spectrum is due to laser-assisted photoemission.

or emit photons from the IR field, leading to sidebands in the photoelectron spectrum. In an atomic system, the EUV photoelectron spectrum consists of discrete atomic peaks, and the LAPE sidebands are easily distinguished. From a surface, the photoemission spectrum consists of a continuous distribution due to the band structure of the solid. Nevertheless, the high density-of-states at the Fermi edge for Pt(111) allows sideband peaks to be discerned at ± 1.6 eV.

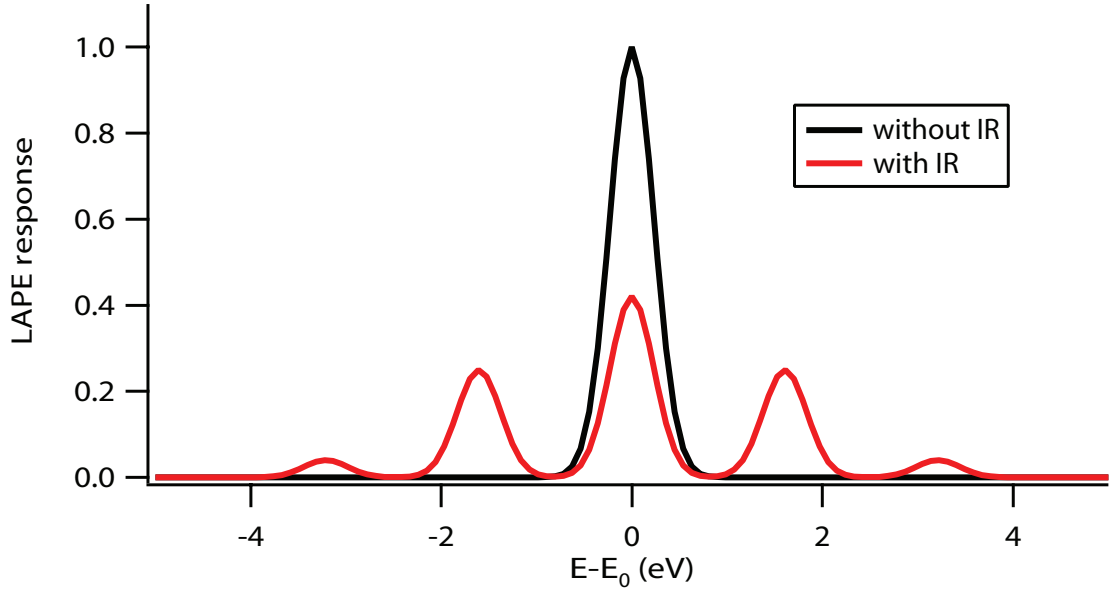

Figure 4.4: Calculated LAPE response function using equation 4.3 assuming the generation of two sidebands.

To quantitatively extract the sideband intensities in the case of photoemission from Pt in the presence of an intense IR field, we modeled the absorption and emission of up to two IR photons by a photo-electron of kinetic energy E_0 by

$$f(E-E_0) = \frac{1-2A_1-2A_2}{\sqrt{2\pi\sigma^2}} e^{(E-E_0)^2/2\sigma^2} + \sum_{\pm}\left(\frac{A_1}{\sqrt{2\pi\sigma^2}} e^{(E-E_0\pm\hbar\omega)^2/2\sigma^2} + \frac{A_2}{\sqrt{2\pi\sigma^2}} e^{(E-E_0\pm 2\hbar\omega)^2/2\sigma^2}\right) \quad (4.3)$$

(see Figure 4.4). Since the kinetic energies of the affected electrons are large compared

to the IR photon energy (soft photon limit), we assume that the influence of the ground state on the free-free transitions is negligible. In particular, this LAPE response function is considered independent of the electron's kinetic energy over the fit range around the Fermi edge. Consequently, the EUV+IR spectrum is expected to be generated by a convolution of the EUV-only spectrum with the LAPE response function of equation 4.3. We therefore fit this convolution to the combined EUV+IR photoemission spectrum, allowing the sideband intensities A_1 and A_2, as well as the width σ and the peak separation $\hbar\omega$, to be fit parameters. The factor in front of the first Gaussian peak is chosen to normalize the response function to 1. The parameters A_1 and A_2 thus give the fraction of electrons scattered into the first and second sidebands respectively. Figure 4.5 shows the result for zero time delay between the IR and EUV beams. The black line gives the photoemission spectrum without the IR pulse present. The red line shows the photoemission spectrum with the IR pulse present. Finally, the blue line shows the fit to the EUV+IR curve by convolving the LAPE response function from equation 4.3 with the unperturbed spectrum. The inset of figure 4.5 shows the LAPE response function associated with the resulting fit parameters: $A_1 = 0.241 \pm 0.004$; $A_2 = 0.013 \pm 0.003$; $\sigma = 0.23 \pm 0.02$ eV; and $\hbar\omega = 1.59 \pm 0.02$ eV. The inset is multiplied by $\sqrt{2\pi\sigma^2}$, so that the peak heights reflect the corresponding intensity parameters A_1 and A_2.

The fit to the sideband separation of $\hbar\omega = 1.59$ eV corresponds very well to the photon energy of the IR beam, while the width σ reflects closely the convolution of the laser bandwidth (≈ 0.1 eV) and the detector resolution at the high energy part of the photoelectron spectrum (≈ 0.2 eV). Initially, we allowed the response function to be asymmetric using different intensity parameters $A^{\pm}_{1,2}$ for the positive and negative sidebands. However, this fit generally yielded sideband heights that were identical for the high- and low-energy sidebands, as would be expected for the LAPE in this weak-field regime (see figure 4.6). The quality of the resulting fit strongly supports the interpretation of these data as surface LAPE. This is further corroborated by the fact

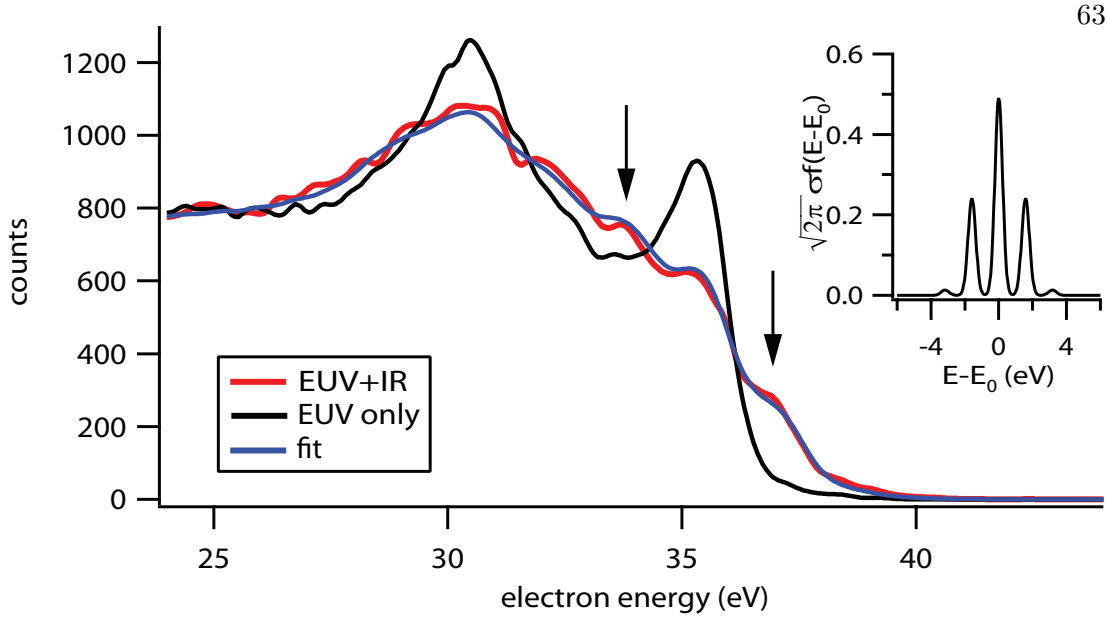

Figure 4.5: Photoemission spectrum at zero time delay between the EUV and IR fields, taken from the data shown in figure 4.3. Observed photoemission spectrum with (red line) and without (black line) the IR pulse present. The blue line shows the fit to the EUV+IR curve by convolving the LAPE response function from equation 4.3 with the unperturbed spectrum. The inset shows the LAPE response function associated with the fit.

that no sidebands are observed when the polarization of the IR light is perpendicular to the direction of detection (s-polarized, see figure 4.15a). However, hot electrons can be observed for both polarizations of the IR field. These hot electron-energy distributions persist for significantly longer times than the LAPE response (hundreds of femtoseconds), and are discussed below.

By fitting the photoelectron spectra for all other time delays, with $\hbar\omega$ and σ fixed to the values derived from the time zero photoemission spectrum, we determine the strengths A_1 of the first-order sideband as a function of delay between the IR and EUV pulses (figure 4.7b). The small error bars show the large sensitivity of the fit to the sideband heights, which is due to the fact that the positive sidebands show up in a region well beyond the Fermi edge where the EUV-only spectrum exhibits a small count rate. For a cross-correlation measurement, an observable which is linear in the laser

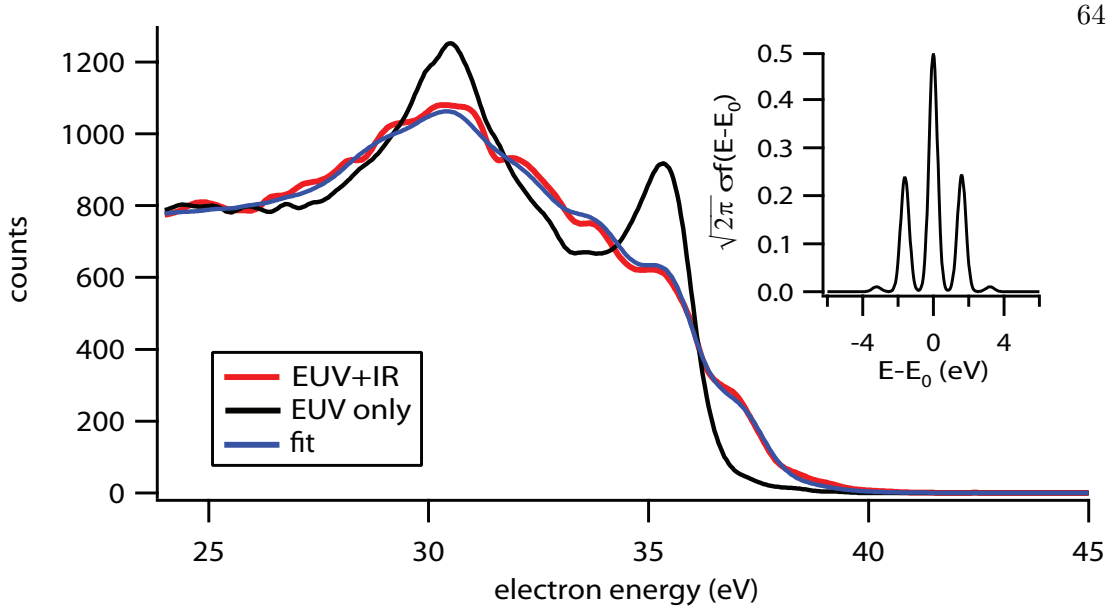

Figure 4.6: Identical spectrum to that shown in figure 4.5, where the positive and negative first-order sideband heights are allowed to vary during the fit. However, no significant asymmetry is generated as a result of this fit.

intensity I_L is required. As shown in figure 4.7a, A_1 fulfills this requirement for small I_L, where A_1 is approximated by the asymptote $A_1^* = x^2/4$, and, following equation 4.1, $x^2 \propto I_L$. For larger intensities, however, A_1 levels off and exhibits a sublinear behavior. To ensure a linear dependence for all data points, the sideband heights A_1 are thus replaced by the corresponding values A_1^* of the asymptote. A Gaussian fit yields a full width at half maximum of 33 $\pm$ 2 fs, in accordance with the expected EUV pulse duration of $\sim$ 10 fs and the IR pulse duration on the order of 35 fs, respectively [50].

Figure 4.8 shows a LAPE measurement at an angle of about $\vartheta = 5°$ (see figure 3.6) between the IR polarization (p-polarized) and the surface normal, close to grazing incidence. At this sample angle, which corresponds to an observation angle of about 20° with respect to the surface normal, the *d*-band peak at the Fermi edge is even more pronounced than in the previous geometry, and it dominates the broader *d*-band structure at 30 eV. As a result, the sideband characteristics of the LAPE process become even more obvious. The steps due to the first- and second-order positive sidebands are

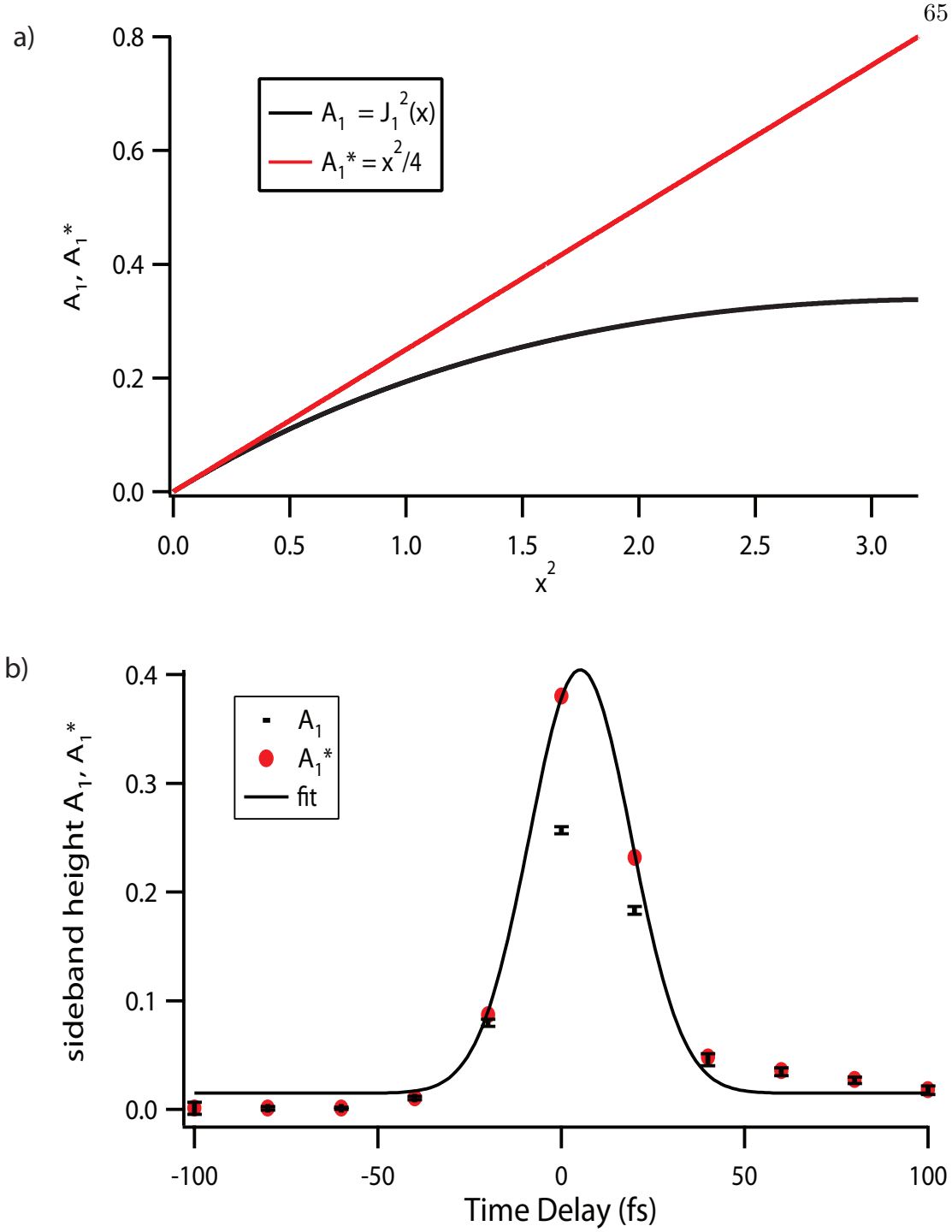

Figure 4.7: (a) The solid line shows the square of the Bessel function $A_1 = J_1^2(x)$,plotted versus $x^2 \propto I$. The dotted line depicts the asymptote behavior for small x: $A_1^* = x^2/4$. For a cross-correlation measurement, a linear intensity dependence of A_1 is required, which is only fulfilled for small x. (b) Measured cross-correlation of the IR (with 30 fs pulse duration) and the expected $\approx$ 10 fs duration EUV pulses as a function of time delay. The measured sideband heights A_1 are replaced by the corresponding values A_1^* of the asymptote, so that linear intensity dependence is ensured for all data points. A Gaussian fit yields 33 $\pm$ 2 fs, limited by the duration of the IR pulse duration. A Gaussian fit to the uncorrected A_1 data yields 37 $\pm$ 3 fs.

more pronounced and the first-order negative sideband is visible. Moreover, like in the previous data set, the EUV+IR spectrum can again be reproduced from the EUV-only data by convolution with the symmetric sideband function of equation 4.3. This result has been found at several other sample angles as well, which are not shown here. The universal applicability of this fit procedure to data taken at different sample angles excludes band structure effects, e.g. the opening of band gaps [91, 92], from being the cause of the observed IR-induced modifications to the photoemission spectra.

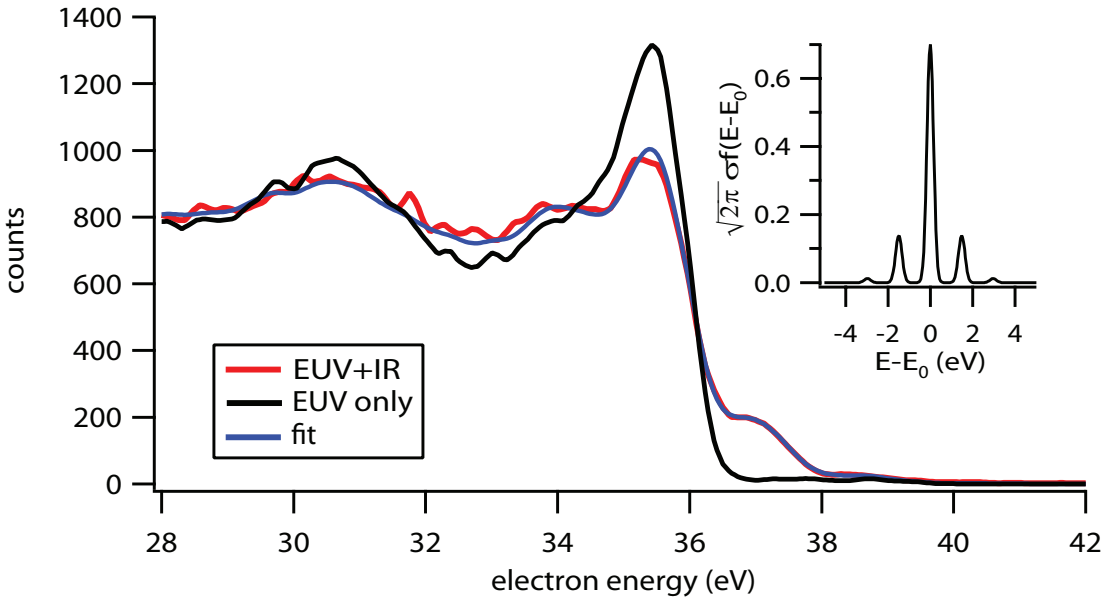

Figure 4.8: LAPE spectrum taken at a different sample angle of $\vartheta = 5°$. Due to the larger d-band peak at this angle, the negative sideband is more clearly visible.

Figure 4.9 shows a time series of LAPE spectra (red curves) between -40 fs and 40 fs in steps of 5 fs. The black curves represent the EUV-only spectra and the blue curves are the fits. In this data set, the space-charge turns out to be stronger than in the previous measurement. This may be due to higher surface roughness, which depends on the cleaning procedure and thus changes from day to day. The corresponding shift to higher energies of the EUV+IR spectra with respect to the EUV-only curve is already corrected-for in figure 4.9. In addition, the data at -40 fs (where the EUV pulse comes

after the IR pulse) reveal a slight smearing of the EUV+IR spectrum, caused by the space-charge induced Coulomb explosion. Despite this smearing, the fit procedure still qualitatively reproduces the EUV+IR spectra, especially the step-like structure in the spectra that show strong LAPE. Quantitatively however, the space-charge distortion will lead to systematic deviations of the fit parameters A_1 and A_2. These sideband heights are plotted versus time delay in figure 4.10. A_1 grossly follows the expected Gaussian cross-correlation characteristics as in the previous data set. However, it does not go to zero at the wings, primarily because of the space-charge effects. Moreover, the background is not constant, but is higher for large time delays. This background is most likely composed of a constant part, due to the space-charge effect, and above time zero, a time-dependent part from hot electrons. These effects will be discussed in more detail in the following sections, but they will not be taken it into account in the discussion of the present data set. A tentative Gaussian fit of the A_1 curve in figure 4.10 yields a width of 38 $\pm$ 5 fs, similar to the previous measurement.

Due to the larger number of data points, the present time series makes it possible to investigate the time dependence of the smaller second-order sideband height A_2 (see figure 4.10). It follows a similar Gaussian curve with a width of 35 $\pm$ 3 fs, in agreement with the time dependence expected from the pulse lengths. Despite the contributions from hot electrons and space-charge, we can perform a coarse check of equation 2.50 by comparing the maxima of A_1 and A_2. For the observed $A_1^{max} = 0.25 \pm 0.02$ we expect, after $A_n = J_n^2(x)$, an accompanying $A_2^{max} = 0.026 \pm 0.06$, which agrees reasonably with the measured value of 0.038 ± 0.002.

Figure 4.11 shows an alternative analysis of the data using the *d*-band peak at the Fermi edge. After subtraction of the EUV-only curves in figure 4.8 from the EUV+IR data, two maxima arise around 34 eV and 37 eV, originating from the the positive and negative first-order sidebands, respectively. Additionally, the depletion of the *d*-band peak leads to a minimum in the subtracted data. These three extrema are plotted

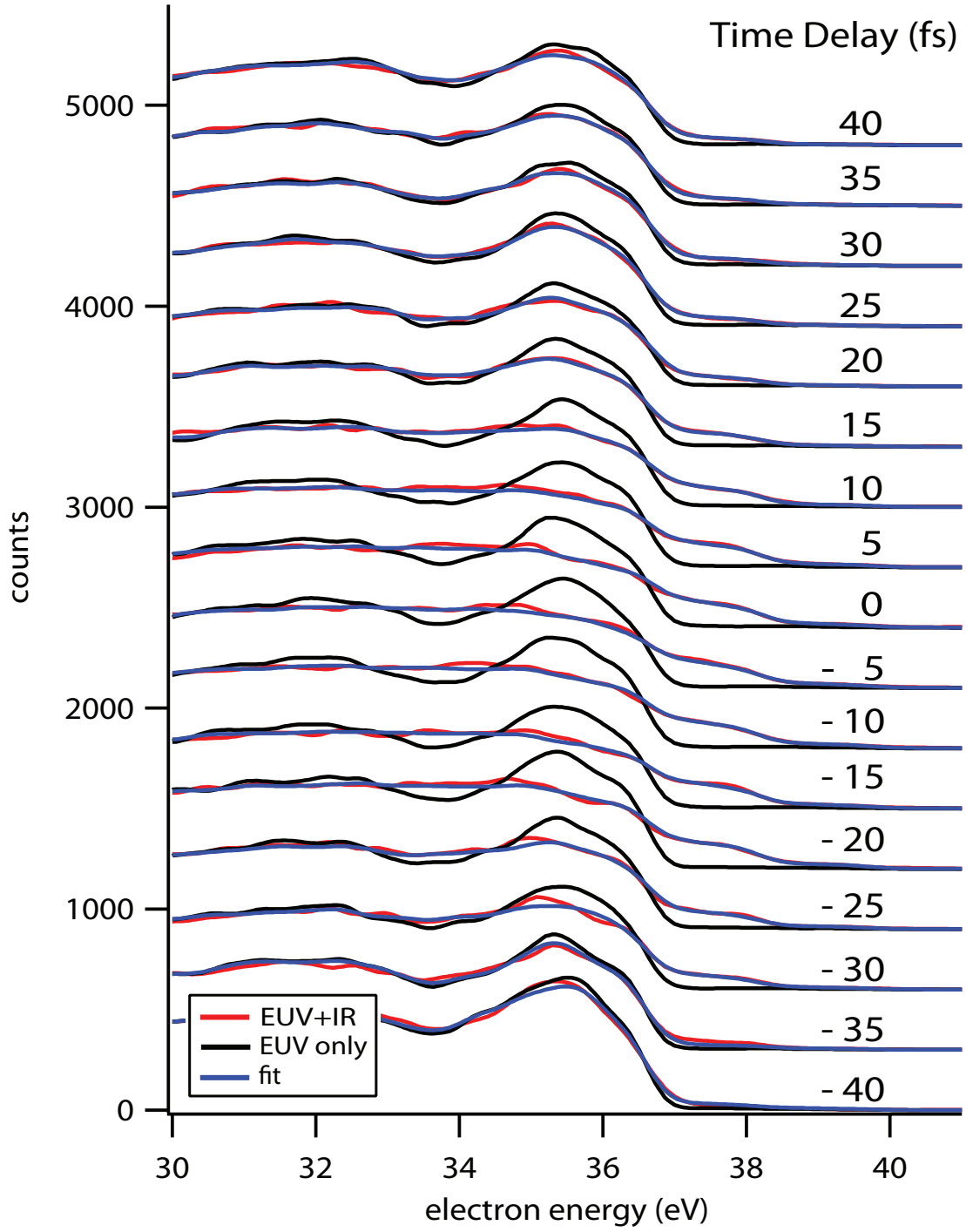

Figure 4.9: LAPE time series for EUV+IR pulse separations between -40 fs and 40 fs in steps of 5 fs. The black lines show the EUV-only data. The EUV+IR spectra (red lines) are corrected for a 0.1 eV space-charge shift. The blue lines show the symmetric fits.

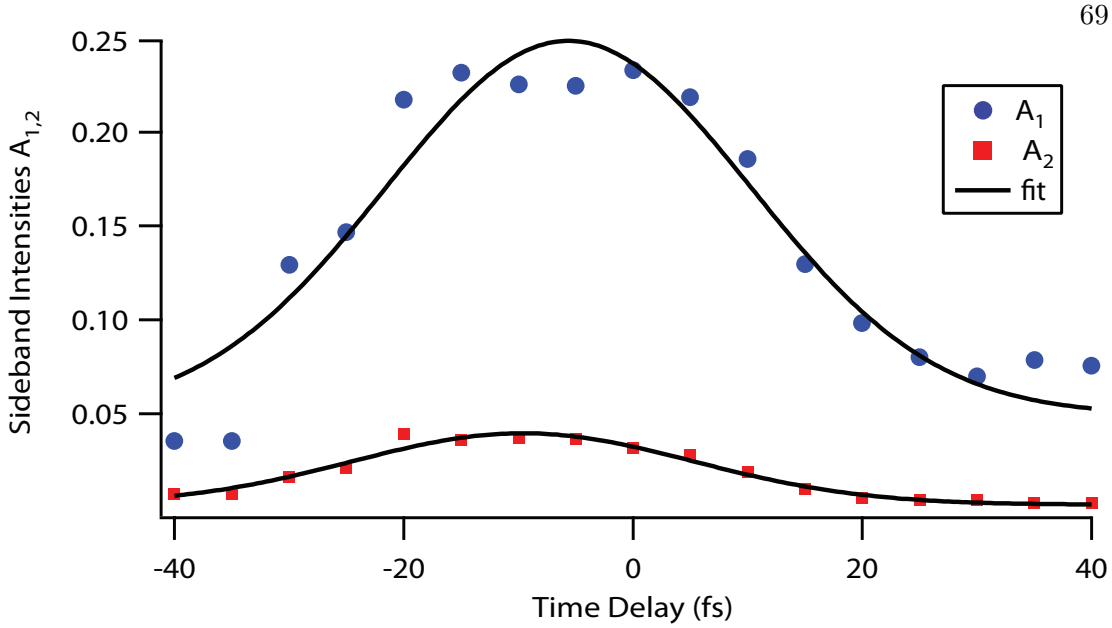

Figure 4.10: Amplitude of the first-order (blue circles) and second-order (red squares) sideband intensity versus time delay. The fits result in FWHM of 37 ± 5 fs and 35 ± 3 fs for the first- and second-order sidebands, respectively.

versus time delay in figure 4.11. Gaussian fits result in widths of 36 ± 4 fs for the positive sideband, 37 ± 6 fs for the negative sideband, and 38 ± 5 fs for the 0th order, which agree with each other and with the pulse widths within their error margins. In summary, dressing of pronounced peak-like structures in the electron spectra of solids can be detected by a direct comparison of the EUV-only and the EUV+IR data and by monitoring the sideband heights or, more sensitively, by the depletion of the photoemission peak. Alternatively, if the structure is more complicated, the convolution of the EUV-only data with a sideband function has to fit to the EUV+IR data. In any case, the dressing makes it possible to measure the time when electrons are ejected from surfaces or adsorbates by photoemission or subsequent Auger decay. To achieve optimum time resolution, other IR-induced effects such as space-charge acceleration or hot electron excitation must be minimized.

As scattering of photo-emitted electrons within the material leads to large angle

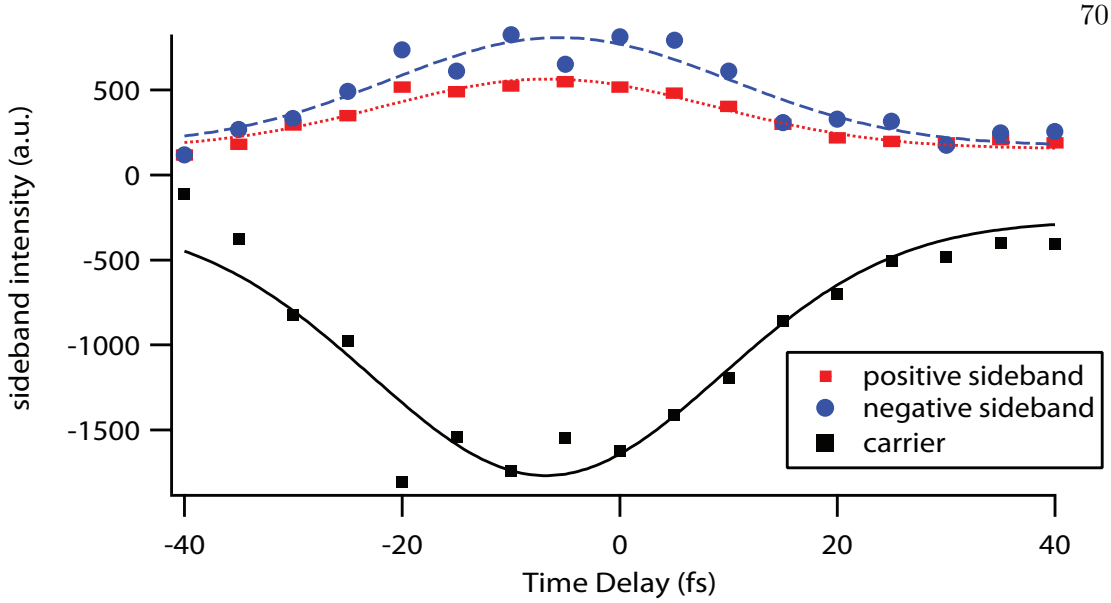

Figure 4.11: Positive and negative sideband heights (upper curve) and depletion of the *d*-band peak (lower curve) versus time delay. The Gaussian fits yield 36 ± 4 fs for the positive sideband, 37 ± 6 fs for the negative sideband, and 38 ± 5 fs for the depletion signal, respectively.

and energy changes, scattered electrons are effectively removed from the part of the spectrum near the Fermi edge that we analyze. The observed electrons thus essentially originate from a thin layer defined by their ≈ 5 Å mean free path. We believe that the finite transit time through this layer ultimately limits the resolution of surface-LAPE for characterizing EUV pulses or for measuring ultrafast inner-shell electron dynamics in solids. In our case, this value is < 200 attoseconds, and thus does not limit our measurement. Still higher resolution could be obtained by increasing the EUV photon energy, and thus the emitted photoelectron energies, so that they escape more quickly. Therefore, this result also opens up new possibilities for studying femtosecond-to-attosecond correlated electron dynamics in solids.

4.5 Laser Intensity Dependence of LAPE from Surfaces

To study the intensity dependence of the first-order sidebands, we first investigated the influence of the sample on the effective intensity on the surface. To this end, the IR light was p-polarized and the surface was rotated horizontally to three different angles ϑ between the IR polarization and the surface normal. $\vartheta = 0°$ denotes grazing incidence with the polarization being perpendicular to the surface. $\vartheta = 90°$ denotes normal incidence and parallel polarization with respect to the surface. Figure 4.12 shows the amplitude A_1 of the first-order sideband extracted at three different angles. Towards $\vartheta = 90°$, A_1 decreases strongly. This sample angle dependence can be fit with a $\cos^2$ consistent with the assumption that only the electric field exactly at the surface interacts with the photoemitted electron. As the parallel component $E_{\parallel}$ vanishes here, only the perpendicular field $E_{\perp} = E_{in} \cos\vartheta$ remains. For moderate laser intensities, A_1 is linear in I_L and therefore follows $I_{in} \cos^2\vartheta$.

Figure 4.13 depicts a series of photoemission spectra taken at different IR peak intensities. EUV+IR (red lines) and EUV-only (black lines) at time zero as well as EUV+IR at -100 fs time delay (blue) are shown. The -100 fs curves reflect the influence of the space-charge of the IR-induced low-energy electrons on the EUV photoelectrons around the Fermi edge. At low intensities, it results in a shift to higher energies due to acceleration, whereas the shape of the spectrum is unaffected. At the highest intensity shown, the space-charge also changes the shape of the spectrum. After correcting for the space-charge shifts using the -100 fs spectra, the sideband heights A_1 are determined using the fit procedure described in the previous section, and results are shown in figure 4.14. The measurement taken near 600 GW/cm^2 is still below the damage threshold of the surface. However, at this intensity the space-charge created by the IR beam on the sample starts changing the shape of the EUV+IR spectrum as compared to the EUV-only spectrum, making the extraction of the sideband amplitude more difficult.

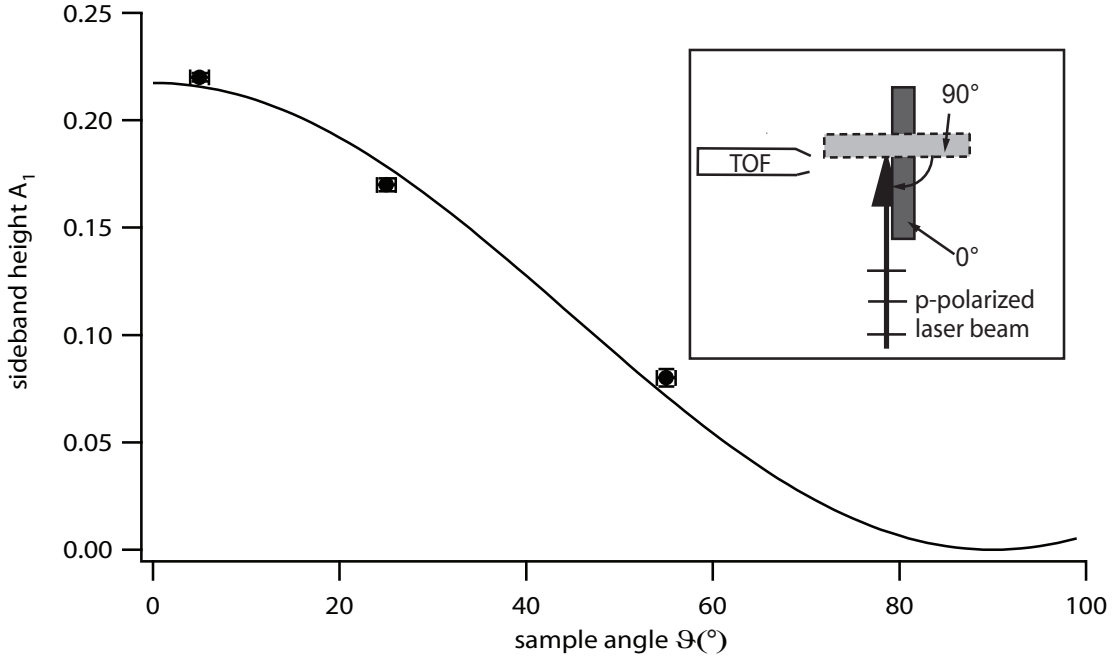

Figure 4.12: First-order sideband height as a function of the sample angle. The sample is shown to influence the effective dressing field, because the component of the electric field perpendicular to the surface is reduced due to boundary conditions. The data agree with the expected $\cos^2$ reduction in the effective intensity. The inset illustrates the definition of the sample angle (surface normal) for 0° and 90° with respect to the IR polarization.

We thus used a EUV+IR spectrum taken at -100 fs as a background spectrum for the convolution, since it shows the same distortions due to the space-charge effect as the EUV+IR spectrum, but does not exhibit the sidebands. This procedure leads to the larger uncertainty for this data point. At even higher laser intensities, electrons from ATP begin to overlap with the Fermi edge in the spectra and bury the LAPE signature. However, such high laser intensities are only necessary for testing the validity of the simple theoretical description of surface LAPE given earlier.

The laser intensity is also corrected for the sample angle, so that it corresponds to the perpendicular component of the electric field. This corrected laser intensity-dependence is then fit to $A_n = J_n^2(a\sqrt{I})$. Here, a is a fit parameter and $n = 1$ denotes the number of absorbed or emitted IR photons. Qualitatively, we find excellent agree-

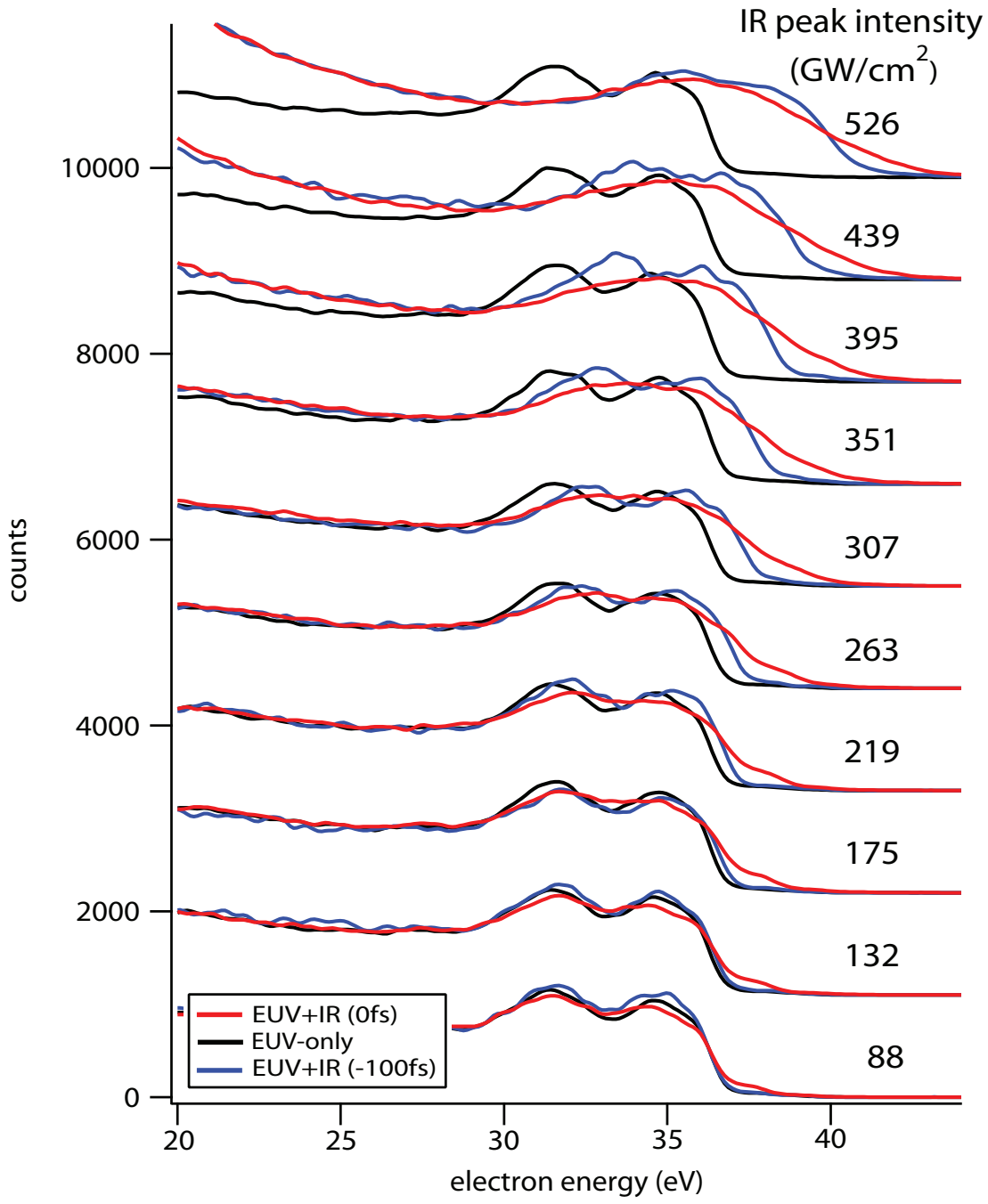

Figure 4.13: Photoemission due to both EUV+IR (red lines) and EUV-only (black lines) light at time zero as well as EUV+IR for a delay of -100 fs (blue lines) for different IR laser intensities. The -100 fs curves show the influence of the space-charge induced by the IR-induced low-energy electrons on the XUV photoelectrons around the Fermi edge. At low intensities, it results in a shift to higher energies due to acceleration. At the highest intensity shown, the space-charge also changes the shape of the spectrum.

ment between our data and this model. The quantitative comparison is limited by the knowledge of the actual IR beam intensity. The peak IR intensity corresponding to the perpendicular electric field at the surface was calculated by taking into account the sample angle. This intensity is likely to be an overestimation of the effective dressing intensity for two reasons. First, the EUV beam spot size is estimated to be a significant fraction of the IR beam spot size. And second, a possible misalignment of the spatial EUV+IR overlap would decrease the effective intensity. From the kinetic energies of the electrons around the Fermi edge and the laser photon energy, the first-order sideband amplitude is expected to peak at 540 GW/cm^2. From the fit we find the maximum of the Bessel function at 960 GW/cm^2, which is within our error margin for the effective intensity. Note also that our highest data point has an amplitude of $A_1 = 0.30$, very close to the maximum of the square of the first order Bessel function of 0.348. This shows that essentially all detected photoelectrons are dressed.

For applications such as measurement of pulse duration or surface electron dynamics, it is desirable to use lower IR pulse intensities in the linear regime, where the cross-correlation $A_1(\tau)$ directly reflects the time behavior under study. At these laser intensities, we found LAPE to be the dominant process. The presence of space-charge induces only a small overall shift in the spectra that can be corrected for. Above threshold photoemission can be suppressed below 600 GW/cm^2 by using a flat surface [95]. The excitation of hot electrons has been found to cause significantly smaller modifications of the photoemission spectrum than LAPE even at rather high laser intensities [99]. However, the presence of such hot electrons can be distinguished from LAPE since their presence increases the average electron kinetic energy around the Fermi edge.

Our data show that laser-assisted photoemission from a Pt(111) surface can be observed for IR intensities up to 600 GW/cm^2, below what is needed to observe heating, ATP, or desorption at metal surfaces [37]. This result is important for applications of surface LAPE to the study of attosecond electron dynamics in solids and in surface-

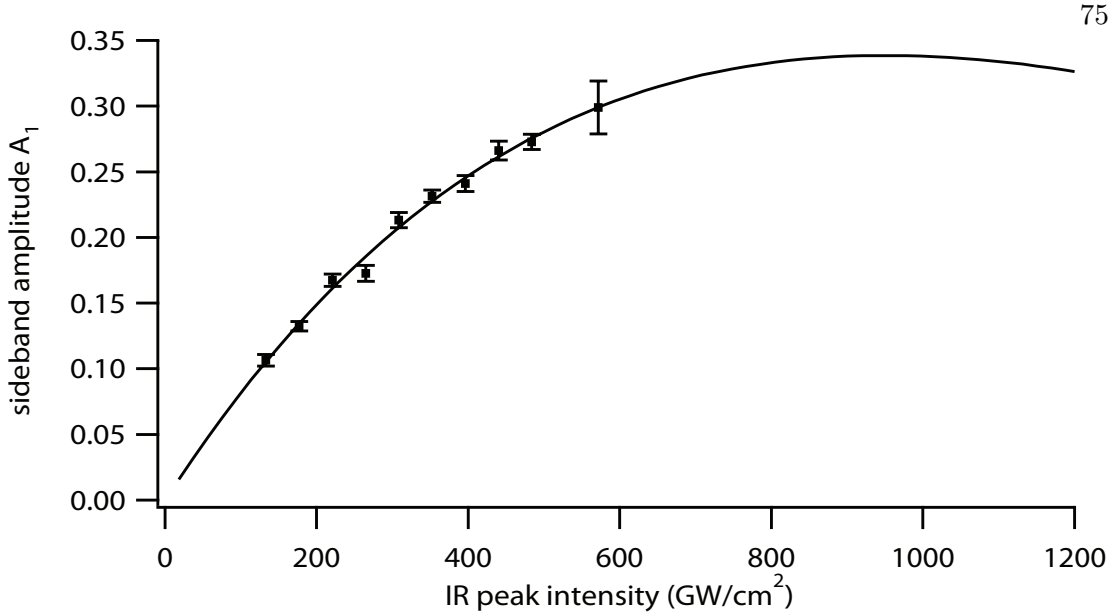

Figure 4.14: Extracted sideband intensity A_1 as a function of the effective IR beam peak intensity, perpendicular to the surface. The influence of the sample angle has been taken into account. The sideways intensity follows the theoretically expected square of the first-order Bessel function. The maximum of the curve is a factor of two higher than expected from the argument of the Bessel function (equation 4.1). This is within our experimental uncertainty in the determination of the effective dressing intensity because of insufficient knowledge of the spatial overlap between EUV and IR pulses on the sample.

adsorbate systems.

4.6 Hot Electrons

At high IR laser intensities ($I_L > 5 \times 10^{11}$ W/cm^2), a significant number of electrons within the conduction band will be excited, resulting in a non-equilibrium hot electron distribution at the Fermi edge. The number of excited electrons depends only on the laser fluence absorbed by the metal. Hot electron excitation is thus expected regardless of the polarization, although energy coupling onto the surface can vary, to some extent, with polarization. In order to observe hot electrons, but suppress LAPE, we acquired the time series of photoemission spectra shown in figure 4.15a using s-polarized IR light at a high intensity of about 10^{12} W/cm^2. For time delays greater than -60 fs, a

slight influence of the IR laser light is observed in the EUV+IR spectra. However, this effect is considerably smaller than in the previous measurements with p-polarized light. We analyze these excess electrons in two different ways. First we subtract the EUV-only spectra from the corresponding EUV+IR spectra. The difference in these spectra show a peak above the Fermi edge stemming from the excess electrons. Figure 4.16 shows the integrated area of this peak versus time delay. The second approach to analyze these data is by calculating the average kinetic energies $\langle E_{\mathrm{kin,IR}} \rangle$ and $\langle E_{\mathrm{kin,EUV}} \rangle$ above the ATP distribution (i.e. >33 eV in this case). In figure 4.16, the solid line shows, as a function of time delay, the normalized difference $(\langle E_{\mathrm{kin,IR}} \rangle$-$\langle E_{\mathrm{kin,EUV}} \rangle)/\langle E_{\mathrm{kin,EUV}} \rangle$, i.e. the laser-induced increase of the kinetic energy. After proper scaling, the curves are shown to follow the same characteristics: an increase in electrons $> E_F$ at -60 fs followed by an exponential decay as the time delay increases. In this case, the IR pulse serves as a pump for the process observed here. This time behavior is fundamentally different from the cross-correlation found for LAPE, and indicates the excitation of a comparatively long-lived hot electron distribution.

Figure 4.15b shows another time series taken with p-polarized IR light at a laser intensity of 5×10^{11} W/cm^2, which is half the intensity used with the s-polarized light data discussed above. These data clearly show a LAPE signal at -40 fs, visible again as a comparably strong step-like modification of the Fermi edge. In addition, excess electrons are visible beyond the Fermi edge for time delays exceeding the EUV+IR cross-correlation time. We again corrected for the small space-charge effect and then evaluated the excess electrons and the kinetic energy increase (figure 4.17). In this measurement, the time dependence of the excess electrons exhibits a two-component structure. We ascribe the peak at -40 fs to LAPE. The corresponding spectrum could be fitted in the way described above. The subsequent slow decay is due to hot electrons. A fit yields a decay time of about 260 fs, in agreement with the measurement using s-polarized light. The kinetic energy curve reflects only the hot electron contribution to

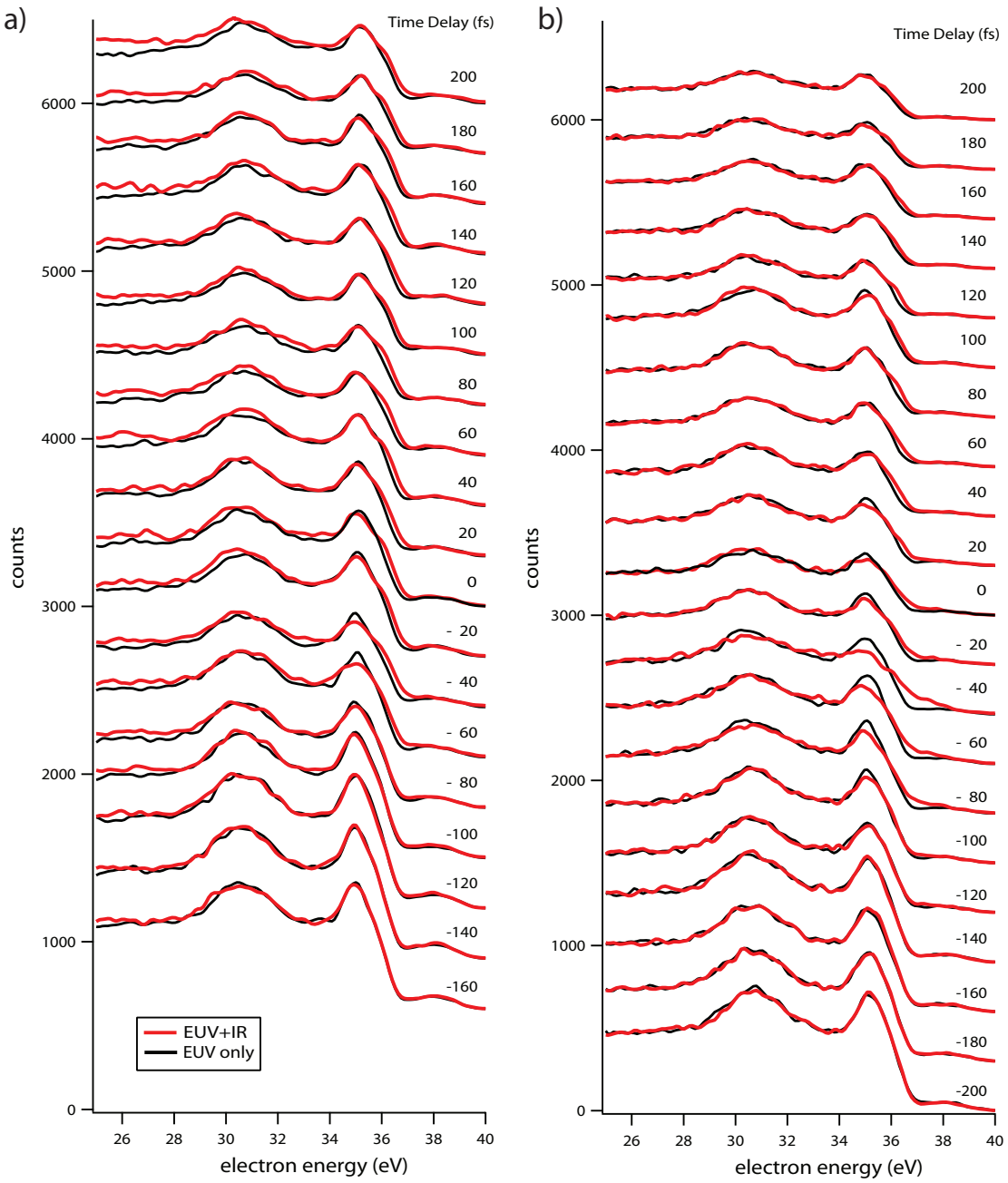

Figure 4.15: (a) Photoemission spectra around the Fermi edge for s-polarized IR light at high laser intensity (10^{12} W/cm^2). The electric field at the surface vanishes in this case, so that no dressing is expected. However due to the absorption of IR light, a hot electron distribution is excited, and is visible at the Fermi edge for relative time delays later than -60 fs (time zero in this measurement). (b) Photoemission spectra for p-polarized IR light at half the intensity applied in a) (5×10^{11} W/cm^2). Hot electrons are visible at positive time delays. LAPE can be observed at -40 fs (time zero), clearly dominating the hot electron distribution and distinguishable by its step-like shape.

the excess electrons since LAPE does not change the net kinetic energy. This shows that the slow decay can be attributed to electrons that gain kinetic energy on average, whereas the peak is due to electrons that are redistributed symmetrically due to LAPE.

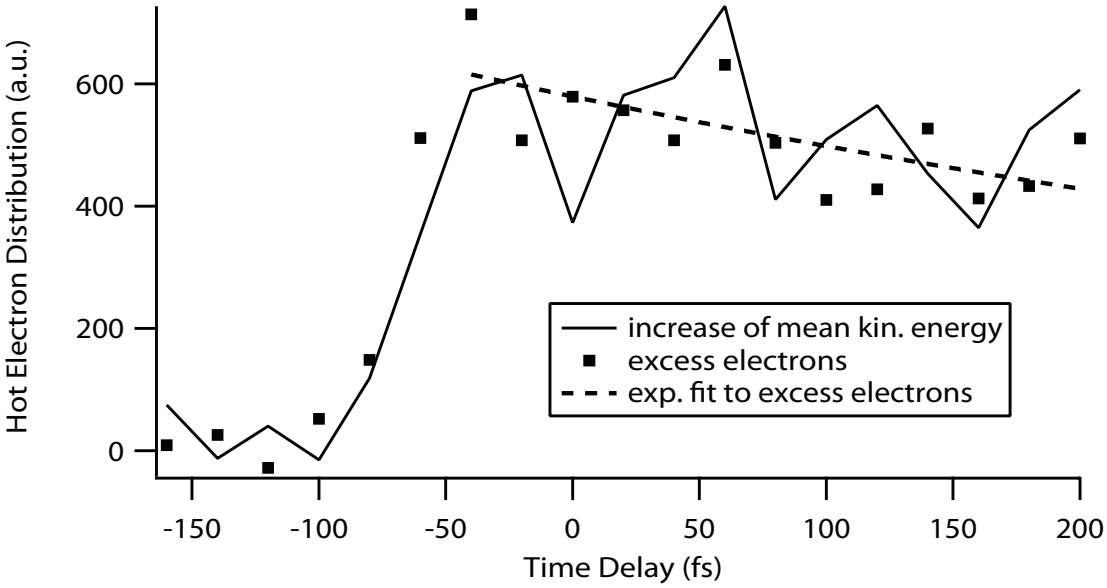

Figure 4.16: Excess hot electrons (dots) at the Fermi edge for s-polarized IR light. These hot electrons follow a sharp rise and slow exponential decay. The fit (dashed) yields a lifetime of about 270 $\pm$ 60 fs. This behavior is also found for the average kinetic energy (solid line) and is consistent with expected hot electron lifetimes.

4.7 Conclusion

In this chapter the laser-assisted photoelectric effect from a solid surface was investigated. By illuminating a Pt(111) sample simultaneously with ultrashort 1.6 eV and 42 eV pulses, we observed sidebands in the extreme ultraviolet photoemission spectrum. Sideband amplitudes were extracted very accurately from the continuous spectra over a wide range of laser intensities. Our results agree with a simple model, in which LAPE is described by EUV photoemission followed by the interaction of the photoemitted electron with the laser field. This strong effect can definitively be distinguished from other laser surface interaction phenomena, such as hot electron excitation, above-threshold

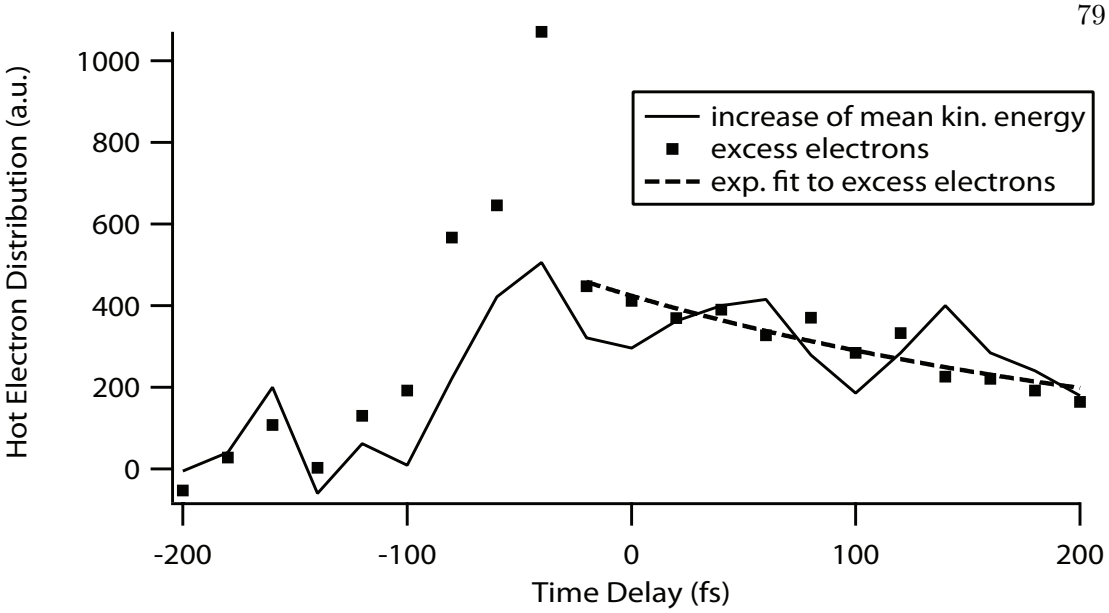

Figure 4.17: Excess hot electrons (dots) at the Fermi edge for p-polarized IR light. In this case, the excess electrons show a two component structure. For large time delays they decay exponentially. The fit results in a lifetime of 260 $\pm$ 80 fs, in agreement with the value found for s-polarized light (270 $\pm$ 60 fs). Around time zero, the electron distribution exhibits a peak which is due to LAPE. The average kinetic energy, which is insensitive to LAPE, still follows the exponential decay behavior characteristic of hot electron decay.

photoemission and space-charge acceleration.

Chapter 5

Direct Measurement of Core-Level Relaxation Dynamics in Complex Systems

5.1 Introduction

The results presented in chapter 4 are important for the study of ultrafast, femtosecond-to-attosecond time-scale electron dynamics in solids and surface-adsorbate systems. By studying the evolution of the sideband height at different time delays between EUV and IR pulses, we can extract information about the electron dynamics. If the electron to be studied is directly photoemitted by the EUV pulse, then the temporal evolution of the sideband height allows us to characterize the EUV pulse duration. However, if the electron under study is a secondary electron, which means the electron is photoemitted some time after the EUV pulse hits the sample, then the temporal evolution of the sideband height encodes information about the time it took for the electron to be photoemitted. In the case of adsorbates (atoms or molecules), a comparison of the time it takes for this electron to be photoemitted while the atom/molecule is absorbed on a substrate or in gas phase gives us information about charge-transfer time scales between the adsorbate and the substrate.

Charge-transfer processes between substrates and adsorbates are of great importance in many areas of surface science [100]. Various approaches have been used to obtain information about charge-transfer time scales, including line-shape analysis [101], core-hole clock spectroscopy [102, 103], and direct time-domain pump-probe

experiments [104,105]. Line-shape analysis has been successfully applied to the study of core-hole lifetimes in isolated molecules and atoms, where spectral lineshapes are mainly homogeneously broadened. Thus, the spectral linewidth is unambiguously related to the dynamics of simple decay processes, because no further energy and momentum dissipation processes exist.

However, in the case of adsorbates on solid surfaces, inhomogeneous contributions due to the substrate (distortions, dislocations, and impurities) and adsorbate-substrate vibrations can increase the linewidth. Charge-transfer processes between the adsorbate and substrate can increase the homogeneous linewidth. For adsorbate states, in general, a clear separation between homogeneous and inhomogeneous broadening is not always possible. Time domain measurements promise to directly observe dynamics unaltered by additional inhomogeneous contributions. However, these experiments require a time resolution comparable to typical electronic charge-transfer time scales, which are often in the range of a few fs, and in some cases can even be sub-femtosecond. As a result, real time experiments [106] have proven to be very challenging.

Core-hole clock spectroscopy is a method that seeks to overcome the limitations of pure energy- or time-domain methods, by using a sequence of energy-resolved measurements in conjunction with an adsorbate core level as an internal "reference clock" for investigating fast electron relaxation dynamics [102, 103]. This approach has demonstrated that adsorbate-to-substrate electron transfer processes can proceed on attosecond-to-femtosecond timescales. However, this technique requires accurate knowledge of core-hole lifetimes in adsorbate-substrate systems, which may differ from the core-hole lifetime of the same atom/molecule in the gas phase. In investigations to date, the lifetime of these core states has been inferred through energy-domain measurements, assuming that the lifetime of these states is not changed from that of a free atom measured using high resolution atomic spectroscopy.

The first time-resolved studies of electronic and charge-transfer dynamics at sur-

faces investigated valence band resonances of chemisorbed and physisorbed atoms and molecules on metallic surfaces [107,108]. These efforts reported a strong influence of the substrate on the resonance lifetimes, even for physisorbed systems, due to good overlap of the electronic wavefunctions. These experiments used time-resolved two-photon photoemission, driven by a combination of ultraviolet and infrared (UV+IR) photons with energies up to a few eV. Therefore, these studies explored adsorbate states in the valence and conduction bands just below the vacuum level. To date however, investigations of core energy levels have been performed only in the energy domain [109]. Recently, the development of high-harmonic generation (HHG) sources [5, 25, 110] has made it possible to access the ultrafast dynamics of both valence and core levels [37,98].

Here we present the first time-domain measurement of Auger decay from a complex materials system - an adsorbate on a surface (Xe/Pt(111)), see figure 5.1. By comparing laser-assisted photoemission from a Pt substrate with the delayed laser-assisted Auger decay from Xe, we measure the core-hole lifetime for the $4d$ vacancy in atomic Xe absorbed on a Pt(111) surface to be 7 ± 1 fs. This measurement is possible despite the many complexities that result from the metallic substrate, such as above threshold photoemission, hot electrons, and space-charge effects. It is also the first measurement of the lifetime of core holes in Xe/Pt, since there exists no spectroscopic measurement of the linewidth of these transitions. The extracted lifetime for the Xe/Pt $4d$ core-hole is consistent with high-resolution linewidth measurements of Xe in the gas phase, clearly validating our approach. Furthermore, our results demonstrate that time-resolved measurements are possible that can definitively identify the nature of any spectral broadening in more tightly bound systems, such as chemisorbed systems. This measurement is the first time-domain observation of highly excited states in a complex system, i.e. not in an isolated atom environment.

As mentioned in chapters 2 and 4, in a laser-assisted process, an atom is irradiated simultaneously by an ultrafast soft x-ray (SXR) and a laser beam. Characteristic

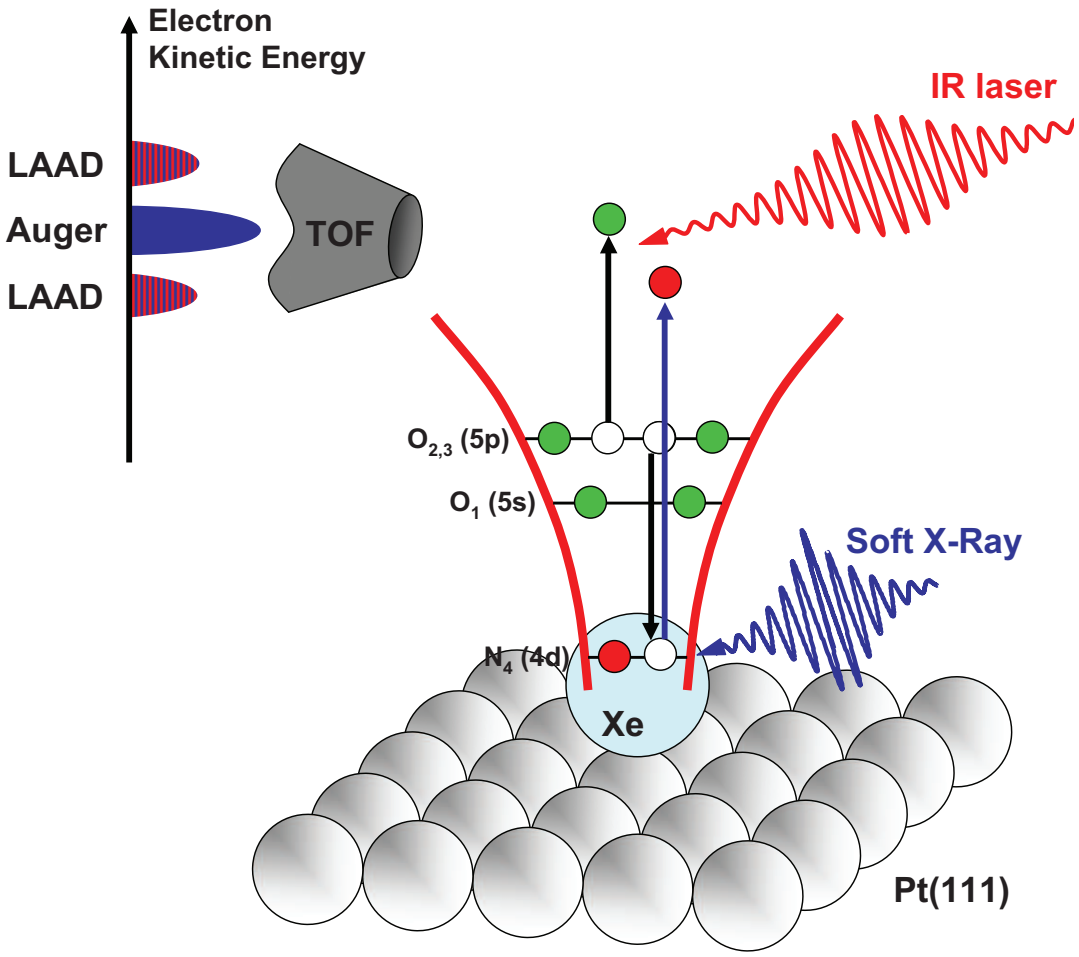

Figure 5.1: Schematic of the experiment. Ultrafast SXR and IR pulses are focused into a Xe/Pt(111) surface, where the kinetic energy of the photoemitted electrons is measured by a time-of-flight detector. An electron from the Xe N_4 ($4d$) shell is ejected by the SXR, followed by filling of the core-hole by an $O_{2,3}$ ($5p$) shell electron and ejection of a secondary (Auger) electron from the $O_{2,3}$ shell. In the presence of the IR beam, sidebands appear in the photoelectron spectrum of both Xe and Pt. By comparing the sideband amplitude vs time delay for the Pt and Xe, we can extract the lifetime of the Xe $4d$ core hole.

sidebands appear surrounding the SXR photoemission peaks, corresponding to simultaneous absorption and emission of laser photons. The magnitude and shape of these sidebands change as the time delay between the SXR and laser beams is changed, encoding information about the underlying electron dynamics.

5.2 Sample Preparation

Before dosing the surface with Xenon, the Pt surface was cleaned via three cycles of oxygen annealing at 450 °C and flashing to 1000 °C. After dosing the Pt(111) surface with a monolayer of Xe at a temperature of 84 °K, three distinct features can be distinguished in the photoelectron spectrum (see figure 5.2). Around the Fermi edge, corresponding to photoelectron kinetic energies of ~ 85 eV, we observe the *d*-band of Pt. At photoelectron kinetic energies between 22 and 26 eV, we detect the Xe $4d$ core-levels, while at energies between 35 and 42 eV, we observe the Xe *NOO* Auger electrons. These Auger electrons are emitted when an electron from the Xe N_4 ($4d$) shell is ejected by a 90.8 eV SXR, followed by filling of the core-hole by an $O_{2,3}$ ($5p$) shell electron and ejection of a secondary (Auger) electron from the $O_{2,3}$ shell, as shown in figure 5.1.

5.3 Results and Discussion

In the presence of an intense laser field, sidebands appear in the Xe/Pt(111) photoemission spectrum (see figure 5.3) over the entire energy range. By comparing the sidebands surrounding the Pt *d*-band peaks (corresponding to the fast process of direct photoemission), with the sidebands surrounding the Auger peaks of Xe (corresponding to the slower process of Auger decay), we can directly measure the lifetime of the $4d$ core hole of Xe/Pt(111). In this way, we take advantage of the precise timing information inherent in laser-assisted photoemission.

In order to extract the sideband height from our data we follow the same steps described in section 4.4. However, for low IR intensities, careful comparison of theory

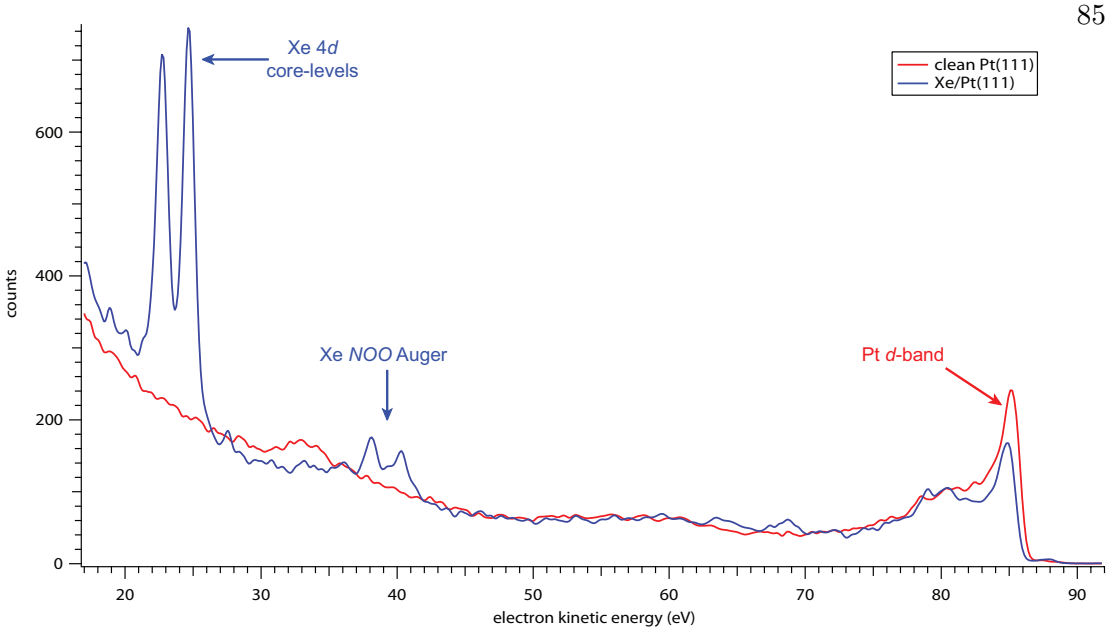

Figure 5.2: Photoelectron spectra for clean (red) and Xe dosed Pt (blue).

and experiment have shown that the sideband height can be modeled by the square of a Bessel function $A_1 = J_1^2(x)$ [70], with the argument given by equation 4.1.

For small intensities, A_1 approaches the asymptote $A_1^* = x^2/4$, and becomes linear in the IR laser intensity I:

$$A_1^* \approx \frac{I E_{\mathrm{kin}}}{\omega_{\mathrm{IR}}^4}. \tag{5.1}$$

Here, E_{kin} represents the kinetic energy of the photoemitted electron, and ω_{IR} the IR photon energy. In this linear regime, A_1 directly provides a suitable observable to follow the electron dynamics. At higher intensities, however, A_1 levels off and shows a sub-linear behavior. To obtain a signal linear in I throughout the entire intensity range, we project the sideband heights onto the asymptote by replacing all measured A_1 by the corresponding values [99].

Figure 5.4 shows photoemission spectra for the case of SXR only, as well as the optimal overlap of both IR and SXR beams in space and time on the Xe/Pt(111) sample.

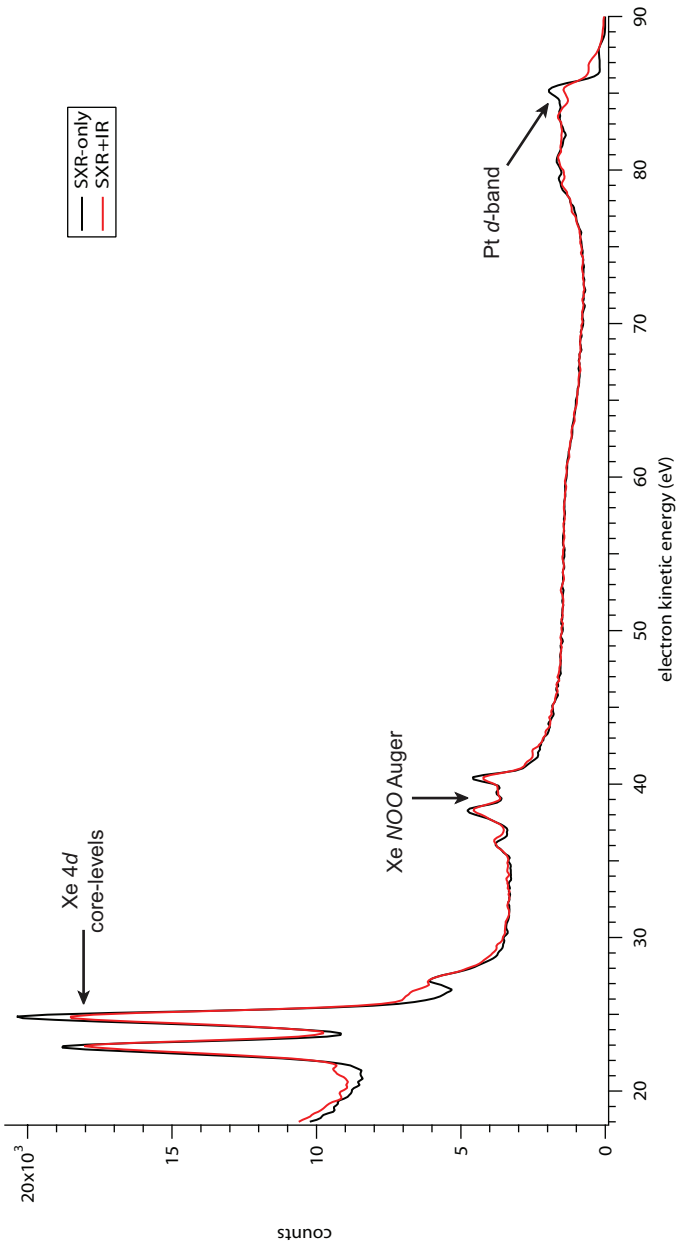

Figure 5.3: Photoelectron spectra for Xe/Pt(111) with (red) and without (black) the presence of the IR pulse.

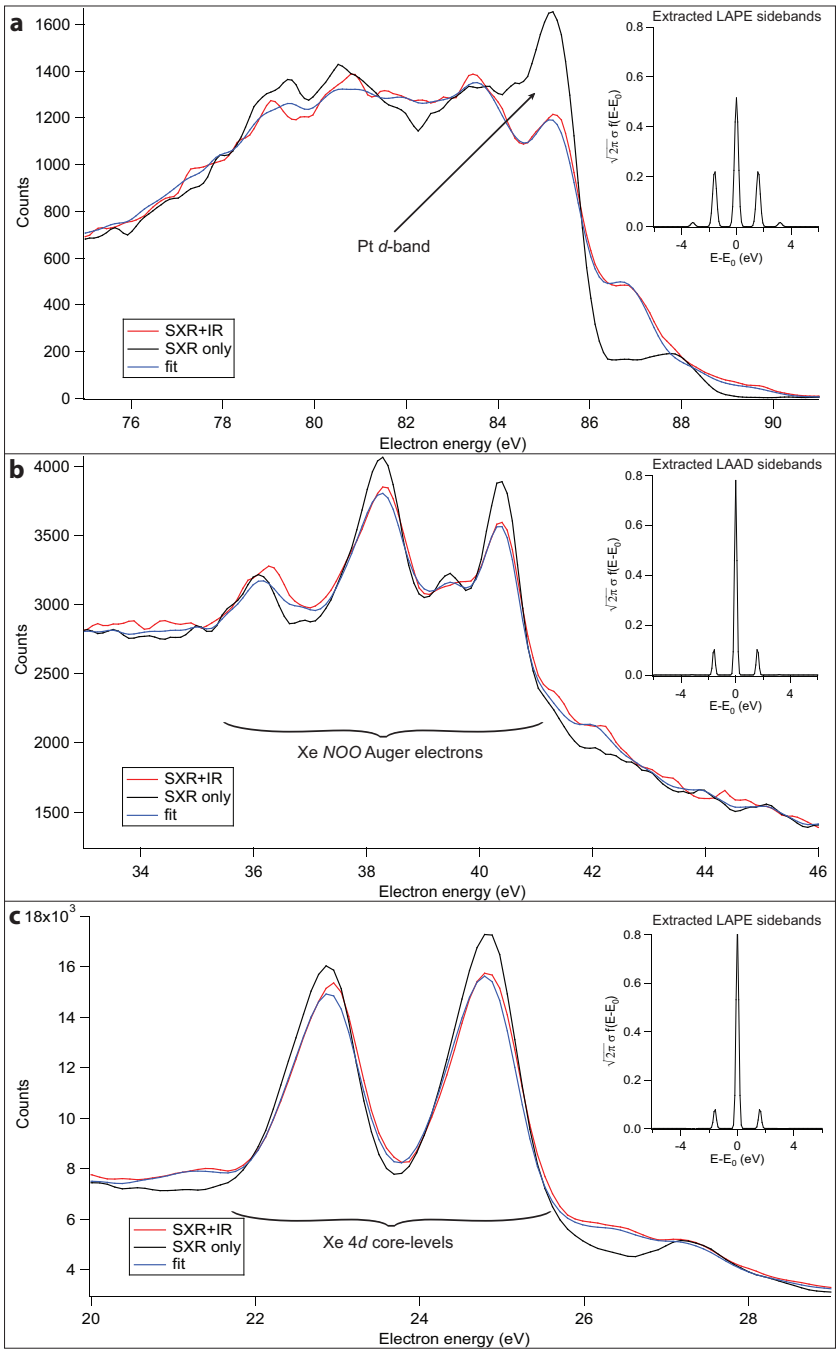

Figure 5.4: Extraction of the LAPE/LAAD sideband amplitudes for Xe/Pt(111) at zero time delay between the IR and SXR beams. (a) Photoelectron spectra near the Pt *d*-band; (b) near the Xe Auger *NOO* bands; and (c) near the Xe 4*d* peaks. The red and black lines represent the spectra with and without the IR pulse, respectively. The blue lines show the fit to the SXR+IR curve when the LAPE response function from equation 4.3 is convolved with the SXR-only spectrum. The insets show the extracted LAPE/LAAD response function associated with the fit, demonstrating the dependence of the sideband amplitudes on the photoelectron energy.

These spectra clearly show strong sidebands surrounding the Pt d-band, with weaker but still detectable sidebands surrounding the Xe Auger NOO peaks and the Xe $4d$ peaks.

Equation 5.1 implies that the ratio of the sideband heights of the Pt d-band and the Xe $4d$ peaks should be equal to the ratio of their corresponding photoelectron kinetic energies:

$$\frac{A^*_{d-\text{band}}}{A^*_{\text{Xe}}} = \frac{E_{\text{kin}(d\text{-band})}}{E_{\text{kin(Xe)}}}. \tag{5.2}$$

To verify this experimentally, one can consider the first-order sideband height at the Pt d-band ($A^*_{d-\text{band}}$), with a value of 0.26 ± 0.01, for a photo-emitted electron kinetic energy of 85.1 eV. For the first-order sidebands surrounding the Xe $4d$ peak (A^*_{Xe}), their height is 0.08 ± 0.01, corresponding to an electron kinetic energy of 24.8 eV. Thus, the sideband height ratio yields 3.43 ± 0.02, while the electron kinetic energy ratio is 3.4. This good agreement of the extracted sideband heights with that predicted by theory, coupled with the excellent agreement of the fit from equation 4.3 and the experimental data over a very broad energy range (blue and red curves of figure 5.4), confirms that laser-assisted photoemission (LAPE) and laser-assisted Auger decay (LAAD) processes are responsible for all the large changes in the SXR photoemission spectrum of Xe/Pt in the presence of an intense IR beam.

Figure 5.5 shows a series of photoelectron spectra at a peak IR laser intensity of 1.3×10^{11} W/cm^2, for relative time delays of -50 fs to 50 fs between the SXR and IR beams. Negative time delay corresponds to the SXR pulse arriving after the IR pulse. The IR beam polarization was chosen parallel to the direction of detection in order to maximize the laser-assisted photoemission sidebands. Due to the low intensity of the IR beam used in this experiment, we do not observe above-threshold photoemission effects [95, 96] at the kinetic energies of the Xe $4d$ peaks, or space-charge effects [35, 97]

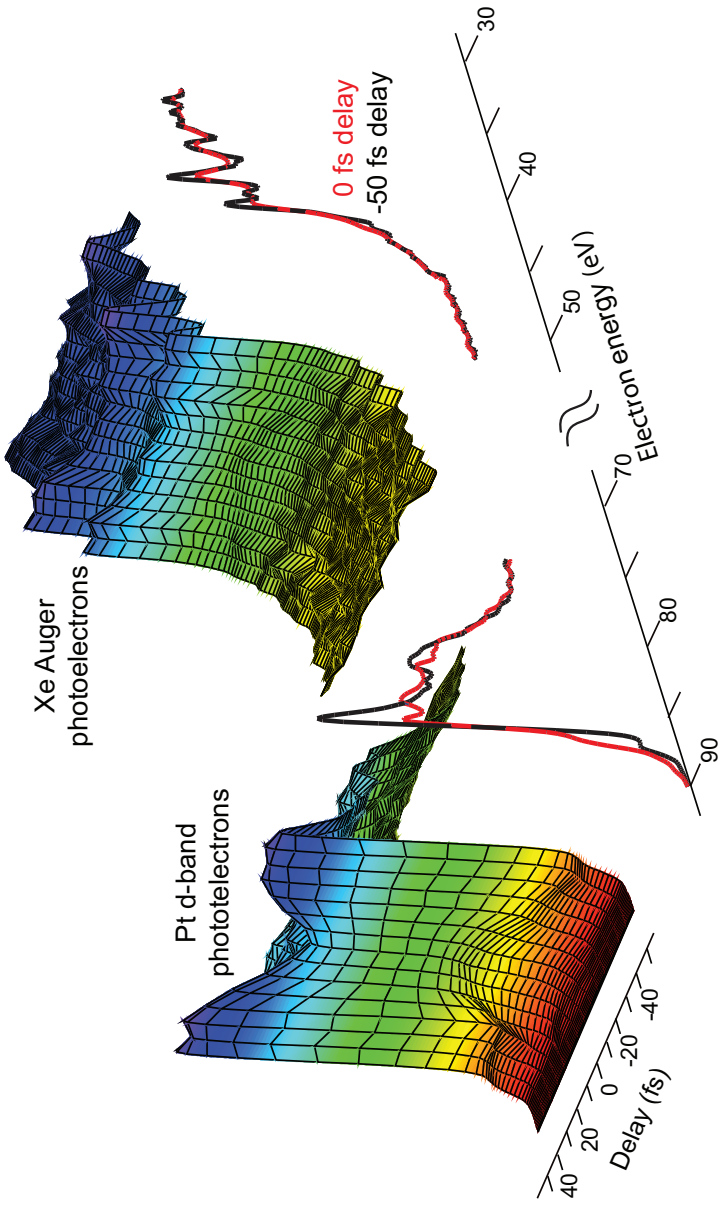

Figure 5.5: Photoelectron spectra from Xe/Pt(111) as a function of time delay. Negative time delays denote that the SXR pulse arrives after the IR pulse. The time evolution of the redistribution of electrons due to the IR dressing at the Pt *d*-band and at the Xe Auger photoelectron peaks can be observed. The spectra shown in the lineouts correspond to the photoelectron spectrum at zero (red) and at -50 (black) fs time delay between the SXR and the IR pulses.

at the Fermi edge. In figure 5.5, the time evolution of the redistribution of electrons can be observed, both at the Pt *d*-band and in the region of the Xe Auger peaks. The spectra shown in the lineouts correspond to the photoelectron spectrum at zero (red) and at -50 (black) fs time delay between the SXR and IR pulses.

For each time delay, the sideband height at the Pt *d*-band and at the Xe Auger peaks are independently obtained. The results for the projected first-order sideband amplitudes are plotted in figure 5.6. The left and right axes have been scaled with respect to each other in order to match the ratio between the kinetic energies of the Pt *d*-band and the Auger peaks. The time evolution of the sideband height for the Pt *d*-band electrons ($A^*_{d-\text{band}}$) corresponds to a cross-correlation between the SXR and the IR pulses. A Gaussian fit yields a FWHM value of 36.1 ± 1.5 fs, centered at time zero. Since our IR pulse duration is 35.5 ± 1.2 fs, measured using the Frequency Resolved Optical Gating technique [111], we obtain a SXR pulse duration of 6.6 ± 6.1 fs from the cross-correlation signal.

In contrast to the sideband signal extracted from the Pt *d*-band (red curve), the sideband signal corresponding to the Xe Auger electrons (A^*_{Auger}) (black curve) is clearly shifted by $\sim$ 6 fs with respect to time zero. Moreover, a Gaussian fit yields a broadened FWHM of 40.1 ± 2.1 fs. The observed time shift and broadening are the result of the inherent lifetime of the Xe $4d$ core-hole. By fitting the Auger sideband curve with the convolution of a decaying exponential and the direct photoelectron cross-correlation obtained from the Pt *d*-band data, we obtain a Xe $4d$ core-hole lifetime of 7.1 ± 1.1 fs. Thus, by comparing laser-assisted photoemission and Auger decay, the characteristic delay of the Auger emission can be precisely measured, making it possible to obtain fairly good resolution even using a relatively long 35 fs IR pulse.

Achieving temporal overlap between the SXR and the IR pulses during the data acquisition time was of crucial importance to accurately extract the core-hole lifetime. In order to test the stability of the temporal overlap, we acquired our data in 10 increasing

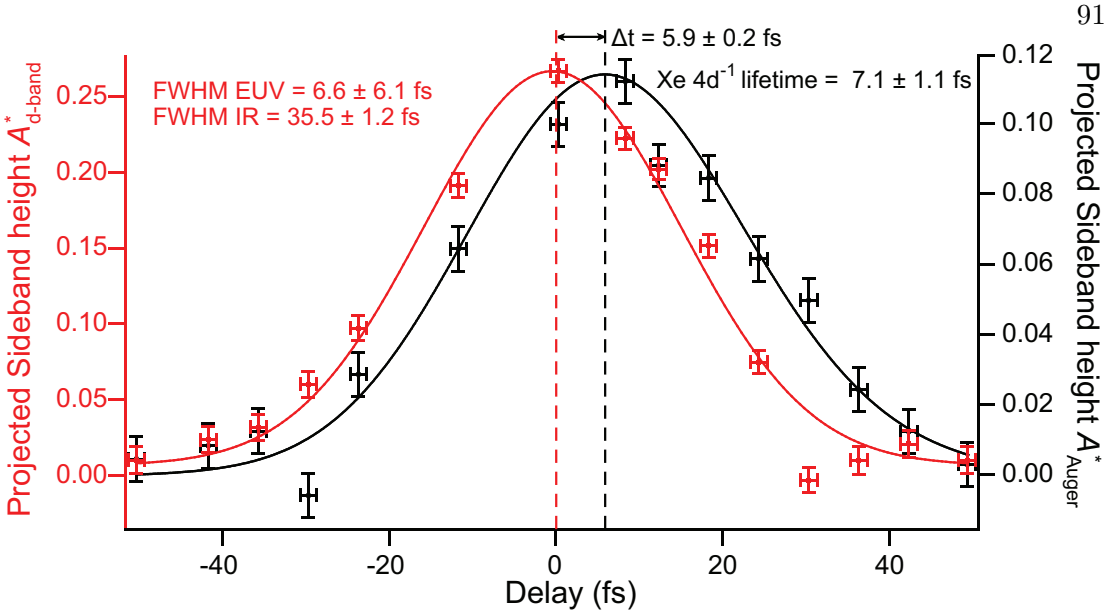

Figure 5.6: Sideband height vs time delay for the Pt d-band and Xe Auger photoelectrons. The sideband height for the Pt d-band (red curve) corresponds to a cross-correlation between the SXR and the IR pulses. In contrast, the Auger sideband height (black curve) is clearly shifted by 5.9 ± 0.2 fs with respect to time zero, and is also broadened with respect to the Pt d-band curve. The shift and broadening are due to the inherent lifetime of the Xe 4d core hole. From these curves we extract a Xe 4d core-hole lifetime of 7.1 ± 1.1 fs.

time-delay scans, each with time duration of 45 minutes. The IR beam was chopped at 1 kHz, and the TOF detector was gated to record SXR+IR and SXR-only spectra, alternately. The peak of the LAPE signal (from the Pt d-band electrons curve) for all scans was compared to extract a slow time-zero jitter between the SXR and the IR pulses. Combining this time jitter, which is mainly caused by mechanical vibrations in our experimental setup, with the statistical error obtained from our fit, we can determine the core-hole lifetime with an accuracy of ± 1.1 fs.

As mentioned before, our measured Xe 4d core-hole lifetime is consistent with a recent gas phase energy-domain measurement (see figure 5.7), that measured a width of 111 ± 3meV (6.3 ± 0.2 fs) for Xe 4d states [8]. The close correspondence between our measurements and previous energy-domain measurements demonstrates that this

technique can extract core-hole lifetimes in the time domain [53], thereby identifying the nature of any spectral broadening in more tightly bound systems, such as chemisorbed systems.

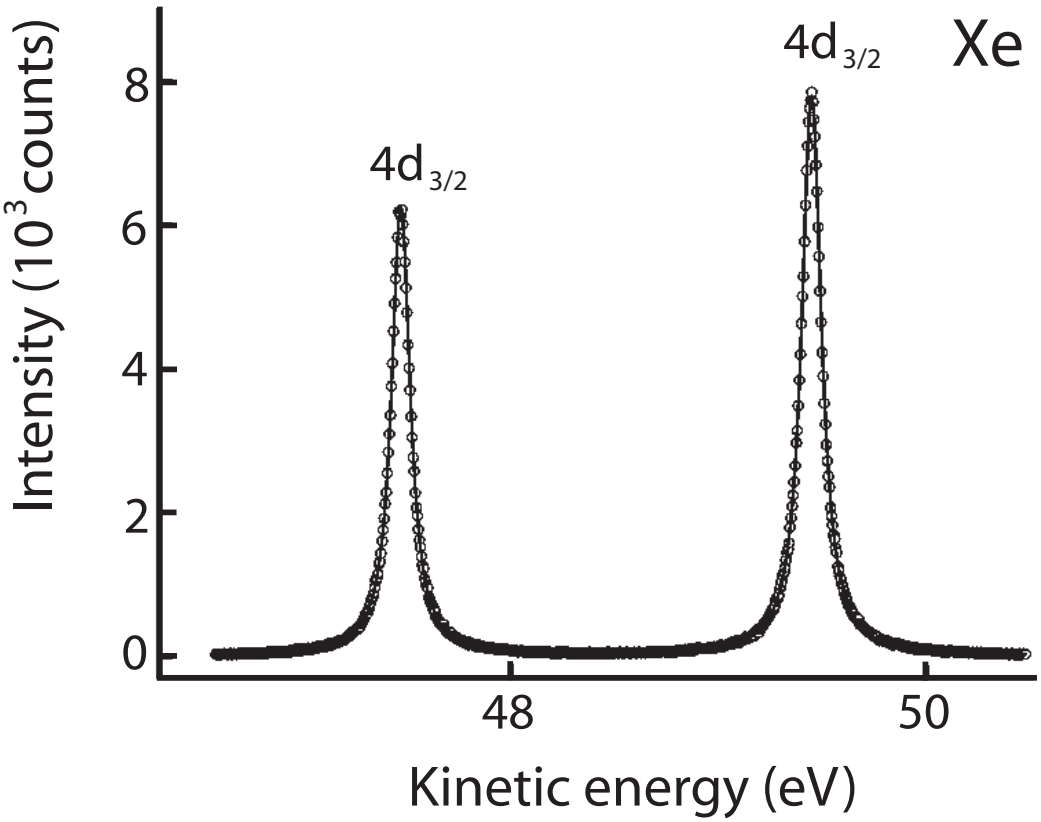

Figure 5.7: Xe 4*d* photoelectron lines measured at 117.0 eV photon energy. The solid line shows the result of the least-square fit to the data points given by circles. Figure reproduced from reference [8].

5.4 Conclusion

By comparing laser-assisted photoemission from a Pt(111) substrate with the delayed laser-assisted Auger decay from Xe, we report the first time-domain measurement of a core-hole lifetime of a complex system - in this case an adsorbate on a substrate. Furthermore, we have experimentally proven the validity of equation 5.1 as a good the-

oretical model for describing LAPE from surfaces. Future experiments can investigate more tightly bonded chemisorbed systems. In these systems, the stronger chemical bond (and hence enhanced charge-transfer process) between substrate and adsorbate is known to influence the linewidth, broadening it compared with the isolated atom case. As well as uncovering the mechanisms that influence charge-transfer at surfaces, these experiments will also provide an exact surface core-hole lifetime as a reference for other charge-transfer techniques such as core-hole clock spectroscopy.

Chapter 6

Laser-Assisted Photoemission with Long-Wavelength IR Pulses

6.1 Introduction

As mentioned in chapter 4, for ultrashort Ti:sapphire laser pulses at a wavelength of 780 nm, intensities on the order of 10^{11} W/cm^2 are typically required to generate observable LAPE signals. At such high intensities, the IR laser can itself lead to electron emission through multiphoton and above-threshold ionization (ATI), or in the case of emission from a solid surface, above-threshold photoemission (ATP). These multiphoton emission processes often result in a large flux of electrons from the sample that can obscure the detection of sidebands. These processes are so-called initial state effects (i.e. signal originates overwhelmingly from atoms that have not interacted with the EUV light), whereas LAPE is a *final state* effect in that these processes are specific to the EUV-excited atoms.

The ATP process is particularly problematic for ultrafast measurements of surface electron dynamics. In ATI and ATP processes, electrons can absorb many more photons than the photoionization threshold, and thus are ejected at high kinetic energies. In the case of ATI in atoms, these electrons generally still have sufficiently low kinetic energies that they are separated in energy from the EUV-induced electrons, and thus are not a major problem. However, past work has shown that ATP from surfaces can be significant at much lower laser intensities than in atoms, due to field enhancement effects [95]. For example, in the series of experiments discussed here, 780 nm IR pulses with a peak

intensity of 1.4×10^{11} W/cm^2 generate ATP photoelectrons with kinetic energy up to 23 eV. These ATP electrons can make it impossible to detect the LAPE signal from dynamic processes that generate free electrons with low kinetic energies. Processes such as Auger decay [53] and interatomic Coulombic decay [112,113] often result in low-energy electrons, and thus their spectroscopic signatures are buried in a large background of ATP electrons. Furthermore, the high flux of ATP electrons from a very small surface area leads to a Coulomb explosion of the electron cloud, in which fast electrons are accelerated and slow electrons are decelerated because of Coulomb repulsion between them [35, 97]. This space-charge effect can distort the photoelectron energy spectrum and also smear the LAPE signal [99]. Thus, for many studies in time-resolved surface electronic dynamics, it is critical to identify approaches for reducing ATP and space-charge initial state effects. Moreover, even in the case of time-resolved studies in isolated atoms, there are cases where a reduction in ATI signal can be desirable.

This chapter shows that the use of a strong-field dressing laser pulse at longer IR wavelengths dramatically reduces ATP and space-charge effects while maintaining a robust surface LAPE signal. Comparing LAPE photoemission spectra from a clean Pt(111) surface taken using 780 nm and 1300 nm dressing wavelengths demonstrates that the LAPE signal is significantly enhanced while the number and kinetic energies of ATP electrons are reduced and the space-charge effects are suppressed. This remarkable improvement results from the favorable wavelength scaling of both the LAPE and ATP effects combined. Therefore, this new approach to laser-assisted photoemission allows us to probe ultrafast dynamics in solids and surface-adsorbate systems over a large final-state energy range. In particular, this methodology promises to make possible the study of time-resolved, low kinetic-energy processes on surfaces for the first time.

6.2 Results and Discussion

As discussed in chapter 4, for low IR intensities, careful comparison of theory and experiment [70, 96] has shown that the sideband height can be modeled by the square of a Bessel function $A_1 = J_1^2(x)$, with the argument given by equation 4.1. And, for a small argument x, A_1 can be approximated by $A_1 \approx x^2/4$ leading to equation 4.2:

$$A_1 \propto \frac{I E_{\text{kin}}}{\omega_{\text{IR}}^4}.$$

Equation 4.2 shows that the amplitude of the LAPE sidebands can be increased by 1) increasing the IR intensity I, 2) increasing the kinetic energy E_{kin} of the electron to be dressed, or 3) decreasing the frequency ω_{IR} of the dressing field. Option one, increasing the IR intensity, is generally undesirable because it increases the ATP electron flux and may also damage or induce desorption from the surface [95]. Option two, increasing the photoelectron kinetic energy, is not generally applicable. For processes such as Auger decay or interatomic Coulombic decay, the ejected electron kinetic energy is determined by the energy level structure of the system, and cannot be varied by changing the energy of the incoming photons. Therefore, the best option for increasing the LAPE signal level is to tune the wavelength of the IR dressing pulses to wavelengths longer than the 780 nm wavelength typical of a Ti:Sapphire laser. This approach is particularly compelling given the λ^4 dependence from 4.2. Tuning to longer wavelengths can be done in a straightforward way using an optical parametric amplifier (OPA) [79]. This approach is also desirable since the OPA process can be used to generate pulses significantly shorter than the (Ti:sapphire) driving laser. However up to this point, the predicted scaling of the LAPE process to longer wavelengths has not been verified experimentally, and the wavelength dependence of processes such as ATP had not been systematically explored.

Figure 6.1 shows the observed photoemission spectra in the energy region near the Fermi edge in the case of illumination of a clean Pt(111) crystal. Here, the EUV and

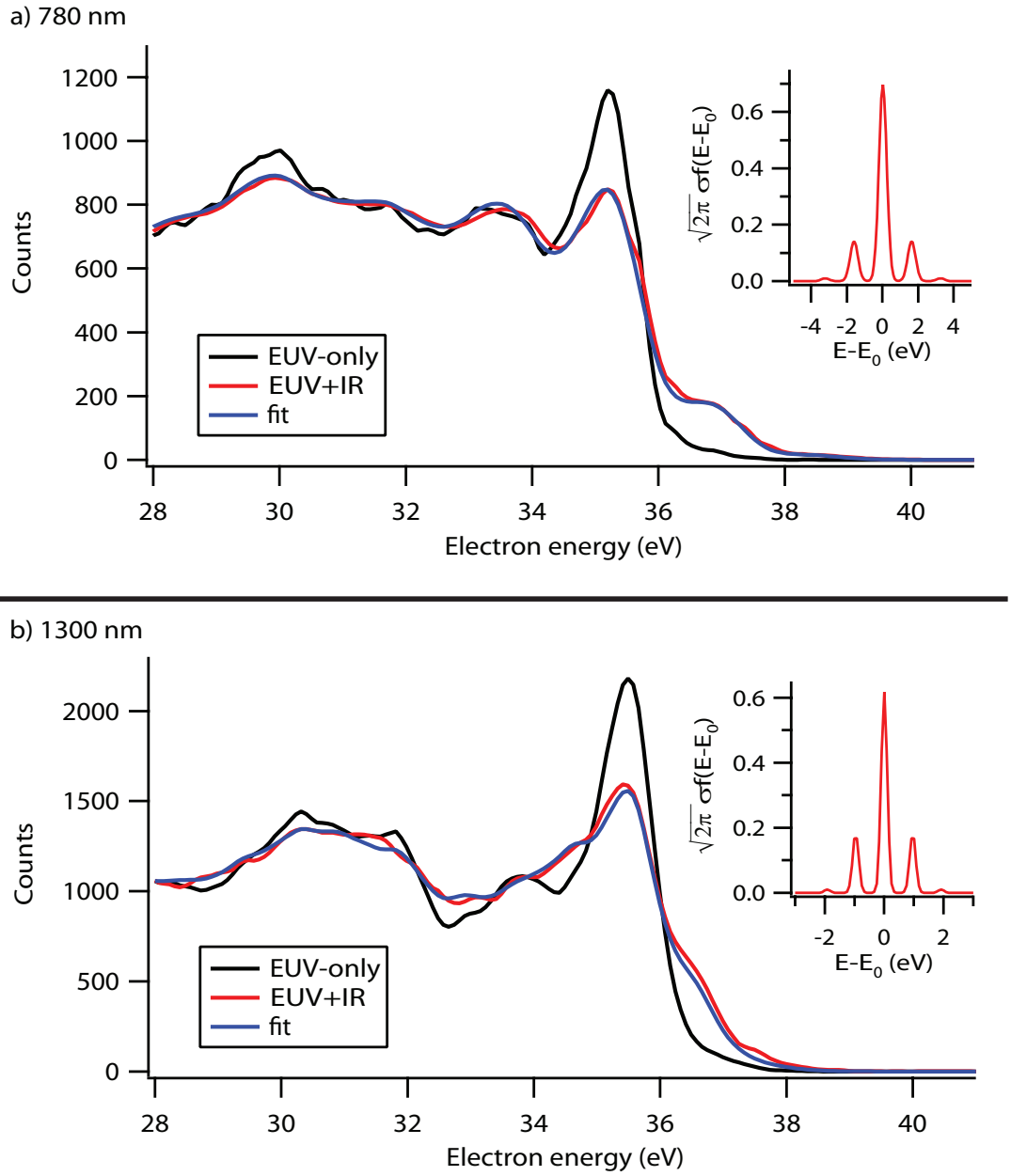

Figure 6.1: Laser-assisted photoelectric effect with (a) 780 nm and (b) 1300 nm driving pulses. Both spectra are measured at zero time delay between the EUV and IR pulses. The red and black lines represent the photoemission spectra with and without the IR pulse present, respectively. The blue lines show the fit to the EUV+IR curve when the LAPE response function from equation 4.3 is convolved with the EUV-only spectrum. The insets show the LAPE response functions associated with the fit. In (a) the 780 nm pulses with peak intensity $I_{780\text{nm}} = 1.4 \times 10^{11}$ W/cm^2 generate sidebands $A_{1(780\text{nm})} = 0.13 \pm 0.01$, while in (b) the 1300 nm pulses with peak intensity $I_{1300\text{nm}} = 2.4 \times 10^{10}$ W/cm^2 generate sidebands $A_{1(1300\text{nm})} = 0.18 \pm 0.01$. Compared with the 780 nm pulses, the 1300 nm pulses create a greater LAPE signal at much lower intensities.

IR pulses are temporally coincident, so that the photoemitted electrons experience the peak dressing laser intensity. The red and black lines give the photoemission spectra with and without the IR pulse present, respectively. The blue lines show the fit to the EUV+IR curve using the fitting procedure introduced in section 4.4. The insets of figure 6.1 show the LAPE response function associated with the resulting fit parameters. In figure 6.1a 780 nm pulses were used to drive LAPE, while in figure 6.1b 1300 nm pulses were used. The figure demonstrates that LAPE driven by 1300 nm pulses shows notably larger sidebands than when 780 nm pulses were used, even though the 1300 nm laser intensity was much lower than the 780 nm laser intensity. Therefore, these data directly indicate that the use of 1300 nm pulses very significantly enhances the LAPE signal [114].

In addition to increasing the strength of the LAPE signal, the lower-intensity of the 1300 nm pulses also dramatically reduces ATP photoelectrons. This happens both because the intensity is lower and because longer-wavelength photons have less energy, thus ATP requires a larger number of photons. This leads to a considerably smaller cross-section for ATP. Theoretical calculations of the ATP cross-section depend on other factors such as the IR intensity, the IR polarization, the work function of the sample, and the time duration of the pulses. Detailed discussions can be found in references [115–118]. Figure 6.2 shows EUV-only and EUV+IR spectra over the full energy range for the cases where LAPE was driven by 780 and 1300 nm pulses. ATP is the main contributor to the difference in the low-energy range. By comparing the difference in the low-energy range in both spectra, we find that the lower-intensity 1300 nm pulses introduce significantly fewer electrons with lower kinetic energies than the higher-intensity 780 nm pulses. Thus, ATP is suppressed when lower-intensity, longer-wavelength pulses are applied.

The suppression of ATP, without a reduction of the LAPE signal, is especially useful for studying dynamics in surface-adsorbate systems. In many interesting processes

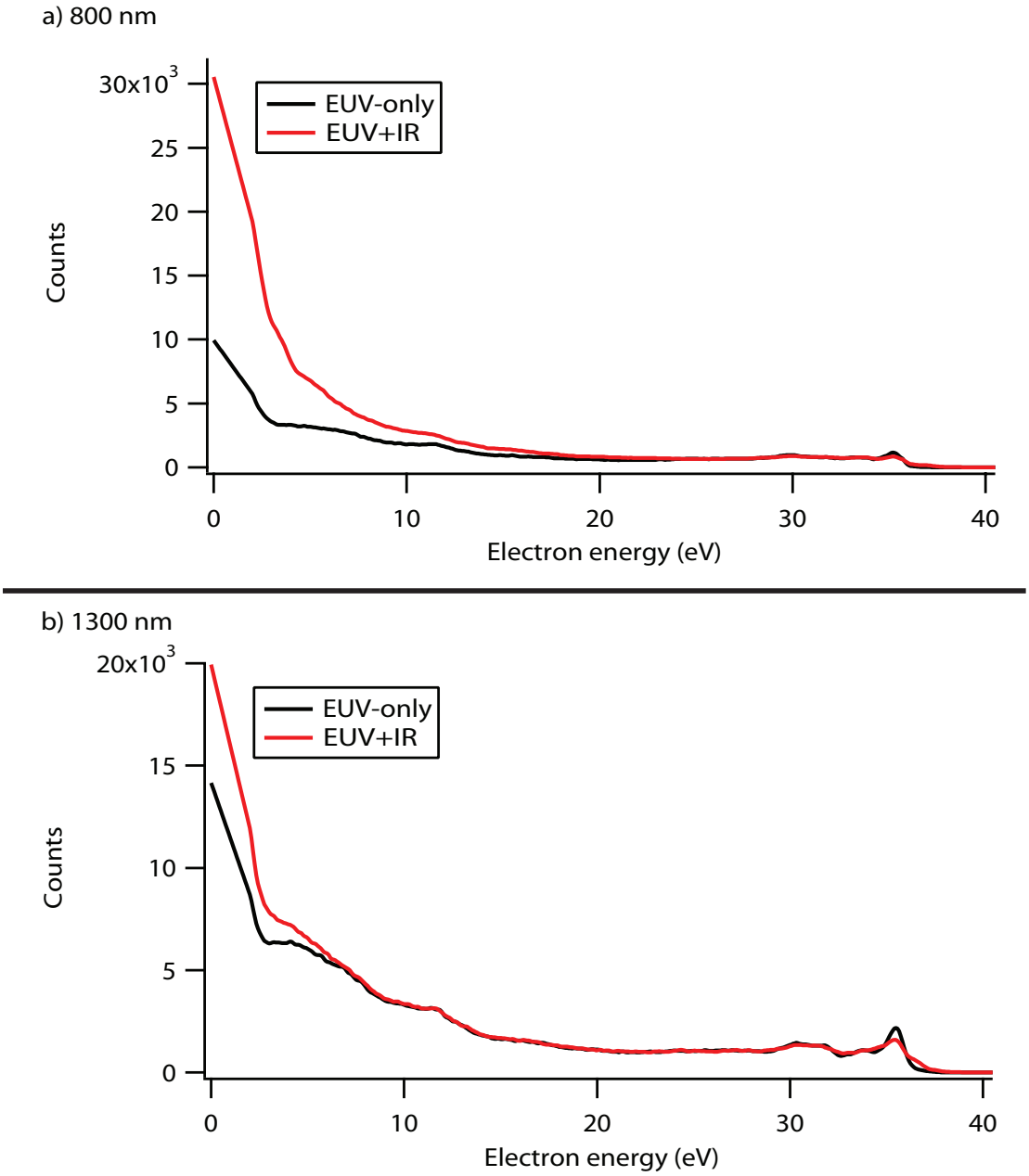

Figure 6.2: Photoemission spectra with EUV pulses and (a) 780 nm pulses (b) 1300 nm pulses. Black curves represent the spectra with the EUV light only, while red curves represent the spectra in the presence of both EUV and IR pulses at zero time delay. In the lower energy range, the difference between the red and black curves is caused by above threshold photoemission. At the Fermi edge, the difference is caused by the laser-assisted photoelectric effect. The intensity required for 780 nm pulses to obtain observable LAPE signal introduces a large amount of photoelectrons in the low energy range up to 23 eV. In contrast, with the 1300 nm pulses, the intensity used produces ATP photoelectrons with kinetic energies of less than 7 eV.

in these systems, the electrons to be studied are photoemitted with low kinetic energies. When longer-wavelength IR pulses are used, ATP generates fewer low-energy electrons, therefore offering a wider energy range in which to detect an unobscured LAPE signal. Furthermore, IR-induced multiphoton or thermal desorption of the adsorbate will also be strongly suppressed.

Besides these improvements, strongly reduced space-charge effects using 1300 nm dressing pulses were also observed (see figure 6.3). In the combined EUV+IR spectrum using 780 nm dressing pulses, a clear shift of the photoemission spectrum to higher energies is seen with respect to the EUV-only spectrum. As explained before, this shift is caused by the Coulomb repulsion of the numerous photoelectrons generated as a result of ATP. In contrast, space-charge effects are suppressed in the 1300 nm spectrum. This leads to a more accurate calculation of the LAPE signal and eliminates the need to correct for space-charge shifts in the LAPE sideband fit, as was done with the data shown in figure 6.1a.

In addition to the advantages mentioned above, the results allow us to experimentally verify the $\omega_{\mathrm{IR}}^{-4}$ dependence of the LAPE sideband strength. Equation 4.2 shows that at low-dressing laser intensities, the first-order sideband height is directly proportional to the intensity of the driving pulse and the kinetic energy of the electron to be dressed, while it is inversely proportional to the frequency of the driving pulse to the fourth power. Using our experimental results from figure 6.1 we can verify the relationship -

$$\frac{\omega_{780\mathrm{nm}}^4}{\omega_{1300\mathrm{nm}}^4} = \frac{A_{1(1300\mathrm{nm})} I_{780\mathrm{nm}}}{A_{1(780\mathrm{nm})} I_{1300\mathrm{nm}}}. \tag{6.1}$$

The predicted frequency ratio yields 7.7, while the experimentally determined factor on the right side of equation 6.1 yields 8.0 $\pm$ 0.4. This excellent agreement between our experimental data and equation 6.1 demonstrates that the theoretical model

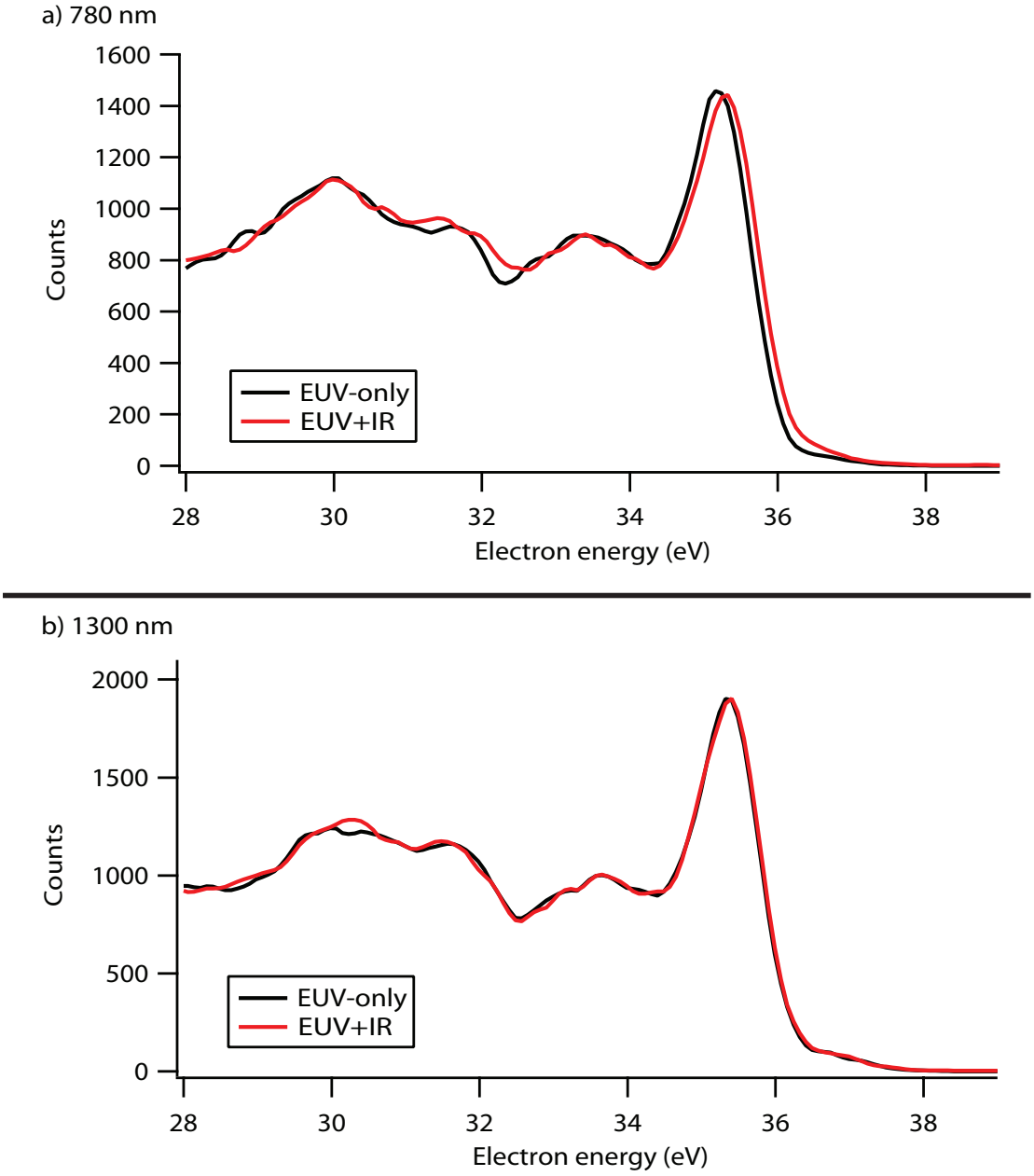

Figure 6.3: Comparison of the space-charge effect around the Fermi edge at -100 fs time delay. For 780 nm pulses, the large amount of low-energy photoelectrons generated through ATP causes a shift of the whole spectrum around the Fermi edge. This effect is greatly suppressed with 1300 nm pulses, because fewer photoelectrons are generated from the IR pulse through ATP at this wavelength.

presented in references [70, 119] is correct for describing LAPE from surfaces. The 4 % discrepancy found in our data is mainly caused by errors in the measurement of the beam size and the spatial overlap between the EUV and IR beams on the sample.

6.3 Conclusion

This chapter reports data that clearly demonstrate several advantages to using longer-wavelength pulses to drive the laser-assisted photoelectric and Auger effects from surfaces. In previous work studying electron dynamics in surface-adsorbate systems, using the correct IR dressing laser intensity was a critical issue. This is because the range of intensities over which LAPE signal could be observed without introducing too much ATP, was quite narrow. By moving to a dressing wavelength of 1300 nm, the enhanced LAPE signal, suppressed ATP, and reduced space-charge noise dramatically improve the range of laser intensities over which good LAPE signals can be observed. This new approach to LAPE and LAAD will therefore be critical for enabling time-resolved studies of ultrafast electronic processes at surfaces.

Chapter 7

Outlook

7.1 Angle-Resolved Photoemission with High Harmonics

7.1.1 Motivation

Currently, our electron detector cannot resolve the emission angles of the photoelectrons emitted from the sample. In many surface science experiments, resolving the emission angle is not critical to understanding the details behind the mechanism under study. For some experiments, however, obtaining angular information and therefore the dispersion of the electronic band structure, will improve our understanding of the processes occurring on the sample. The development of electron analyzers capable of recording in parallel the kinetic energy E_{kin} and the momentum $k_{\parallel}$ of the photoemitted electrons, allows the investigation of the sample's electronic band-structure $E_{\mathrm{kin}}(k_{\parallel})$.

The results shown in this section were performed with one of these new detectors in the laboratory of Prof. Martin Aeschlimann at the University of Kaiserslautern. This experiment is a result of the ongoing collaboration between the Kapteyn/Murnane, Aeschlimann and Bauer groups.

7.1.2 Introduction

In recording the momentum-resolved electronic structure $E(k)$ of a surface, angle-resolved photoemission spectroscopy (ARPES) has emerged as a leading experimental

technique. ARPES identifies static key properties of complex systems, such as adsorbed molecules [120] or high-temperature super conductors [121]. The ultrafast dynamics in these systems associated with nuclear motion or phase-transition after intense laser irradiation, provide valuable information on fundamental physical properties. These ultrafast dynamics can be mapped by the measurement of $E(k)$ as a function of time using femtosecond time-resolved ARPES. In particular, by recording the energy distribution as well as the momentum distribution of the photoemitted electrons, a complete characterization of the different steps involved in these processes becomes possible. To drive such an experiment, powerful femtosecond and attosecond light sources in the EUV-regime, such high-order harmonic generation, are required.

In the past, exclusively time-of-flight (TOF) electron analyzers have been used in photoemission spectroscopy (PES) experiments in combination with HHG, because they exhibit a relatively high detection efficiency [40, 50, 98, 122, 123]. The drawback of these types of analyzers is their restricted energy resolution for kinetic electron energies beyond 10 eV, which is the energy regime typically probed in conventional EUV-PES. Furthermore, in their conventional configuration, these analyzers are only efficient in terms of energy detection. With respect to mapping of angular distribution of photoemitted electrons, only very specific and complex TOF configurations (for instance multi anode-systems) can provide the required efficiency. In order to achieve reasonable time- and angle-resolved PES (TR-ARPES), a parallel detection for energy and momentum of the photoemitted electrons is indispensable. In recent years, hemispherical energy analyzers have been developed which are equipped for parallel (and therefore efficient) detection of a multitude of energy channels, as well as momentum channels, of photoemitted electrons. This development has enabled an electron analyzer system for angle-resolved photoemission spectroscopy using a low-repetitive, low-intensity, HHG light source with high-energy and high-angular resolution independent of the electron kinetic energy.

The main challenge for this experiment is to show that ARPES at a reasonable count rate can be performed using a kHz fs-HHG source. This section, presents the first ARPES data achieved using a 1 kHz HHG light source and a hemispherical energy analyzer, equipped with a 2D-detector for parallel energy and momentum detection [124]. The results show that ARPES using high harmonic light at a photon energy of 41.85 eV can be performed with an angular resolution better than 0.6° (corresponding to 0.03 Å^{-1} at $E_{\text{kin}} = 36$ eV). A comparison of the HHG PES-spectra with corresponding data recorded with a conventional He discharge lamp ($h\nu = 40.81$ eV) allows us to determine that the total bandwidth of the HHG-light transmitted by the non-dispersive monochromator is 801 ± 10 meV, which is capable of supporting EUV pulses as short as 3 fs.

In comparison with femtosecond light sources in the visible or VUV regime, the use of high-harmonic light for time-resolved experiments has three main advantages:

- The high photon energies delivered by the HHG source extend the information accessible by time-resolved photoemission experiments to deeper-lying electronic states, even into the regime of classical core-level spectroscopy.

- The use of intense femtosecond pump-pulses in time-resolved photoemission experiments often gives rise to a parasitic electron background in the kinetic energy range of up to about 10 eV, resulting from multiphoton photoemission processes [63,98]. Therefore, to extract the relevant primary (probe) photoemission signal out of this background, the significantly higher photon energy (and consequently electron kinetic energy) delivered by a HHG source is desirable.

- Finally, for a given acceptance angle of the energy analyzer, the use of high photon energies significantly extends the accessible momentum range of the photoemitted electrons.

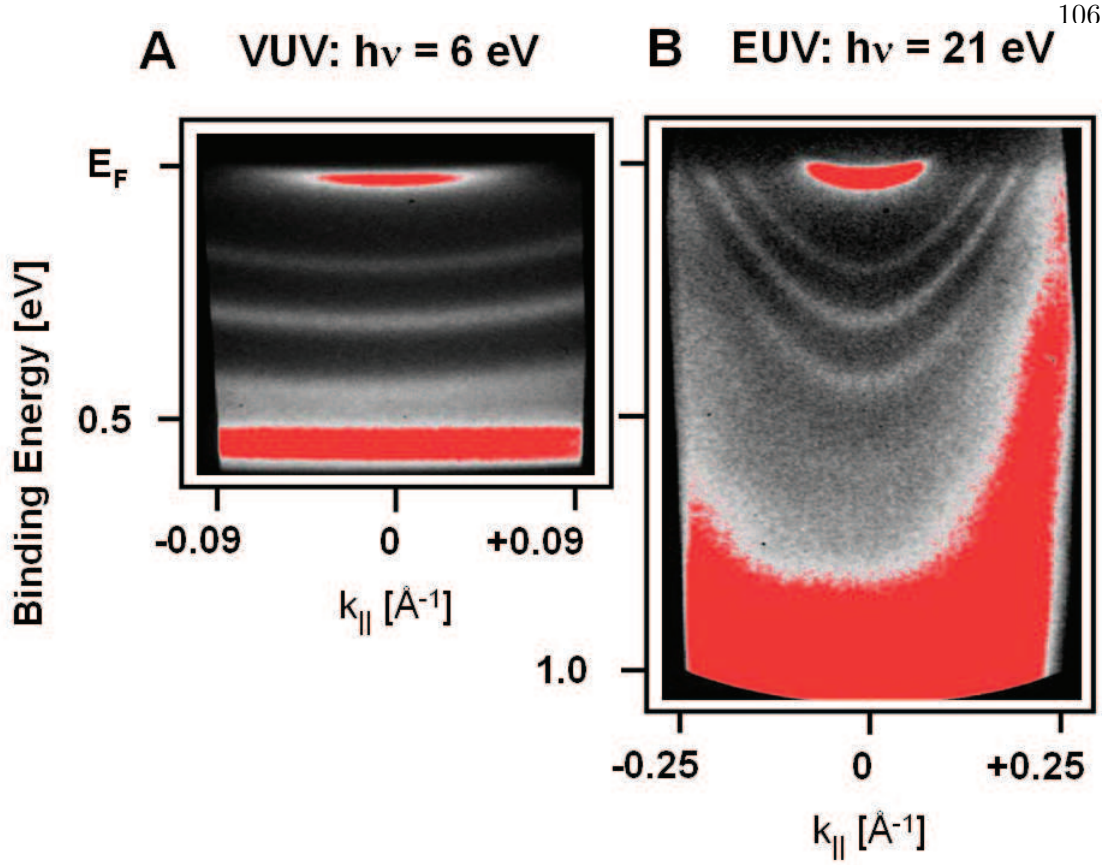

Figure 7.1: Angle resolved PE-spectra of the Shockley surface state and a series of quantum-well states of 40 ML Ag/Cu(111) recorded at photon energies of (a) 6 eV (4^{th} harmonic of the Ti:Sapphire oscillator) and (b) 21.22 eV (He I line of the discharge VUV-lamp). An increase in photon energy enables access to electronic states at higher binding energies and extends the experimentally accessible momentum space.

This last issue is highlighted in figure 7.1, which displays angle-resolved photoemission data of ultrathin silver films (40 ML) on Cu(111), recorded at photon energies of 6 eV (fourth harmonic of the Ti:Sapphire oscillator, figure 7.1a) and 21.22 eV (He I line of the discharge VUV-lamp, figure 7.1b). The plots map the kinetic energy distribution of the photoemitted electrons as a function of the emission angle θ. The series of dispersive states visible in both maps are due to the Shockley surface state (top-most feature) and quantum well states (higher binding energy states), the latter ones localized within the silver film [125,126]. The component of the electron momentum parallel

to the surface, $k_{\|}$, is conserved in the photoemission process. For a given emission angle θ and kinetic energy E_{kin}, its absolute value can be calculated to:

$$k_{\|} = \sqrt{\frac{2m_e}{\hbar^2} E_{\mathrm{kin}}} \sin\theta. \tag{7.1}$$

This equation directly implies that for a given analyzer acceptance angle, a higher electron kinetic energy allows for a deeper view into momentum-space. The apparent difference in the dispersion of the quantum well states as a function of the emission angle between figure 7.1a and figure 7.1b is a direct consequence of this property. The constant acceptance angle of ± 7° for both measurements transforms into a $k_{\|}$ interval of about ± 0.09 $\mathrm{Å}^{-1}$ for initial state energies close to the Fermi edge at 6 eV excitation ($E_{kin} \approx 2$ eV), and into a $k_{\|}$ interval of about ± 0.25 $\mathrm{Å}^{-1}$ for the same initial states but for excitation energies of 21 eV ($E_{kin} \approx 16$ eV). In terms of probing transient changes in $E(k)$ within time-resolved photoemission experiments, the use of ultrashort EUV pulses instead of UV-pulses will obviously extend the accessible states not only with respect to energy but also with respect to momentum.

7.1.3 ARPES using femtosecond high harmonic light

Figure 7.2 shows two photoemission maps of the Cu(111) surface for momentum values between 0.7 $\mathrm{Å}^{-1}$ and 1.52 $\mathrm{Å}^{-1}$ (corresponding to electron emission angles between 13.3° and 28.3°). The left spectrum (figure 7.2a) has been recorded with the He II line of the gas-discharge lamp with a photon energy of $h\nu = 40.81$ eV. The right spectrum (figure 7.2b) is the corresponding photoemission map recorded with the 27^{th} harmonic of a Ti:sapphire laser system, corresponding to an energy of $h\nu = 41.85$ eV. For both maps, identical analyzer settings have been used, corresponding to an energy resolution of 200 meV. Two dominant features can be identified in the two spectra: the barely dispersive copper 3*d*-bands between 2 eV and 4 eV binding energy, and the *sp*-band which splits off the *d*-band at about 0.85 $\mathrm{Å}^{-1}$. The *sp*-band is characterized by its

distinct parabolic dispersion. Contributions to the HHG-spectrum due to lower and higher order harmonics are not visible in the spectrum. The upper limit of such a contribution can be deduced from the intensity ratio between the dominant *d*-band feature at 3 eV binding energy and the signal from the adjacent harmonics located at ± 3.1 eV from this feature (see figure 7.3a).

This estimation shows that any contribution from the 29^{th} harmonic is suppressed by a ratio of better than 1:25, while the corresponding value for the 25^{th} harmonic is better than 1:7. The increased suppression of the 29^{th} harmonic in comparison to the measured/calculated multilayer mirror reflectivity is achieved by tuning the high-energy cutoff of the harmonic generation process right above the 27^{th} order. The residual photon flux of the 27^{th} harmonic available for photoemission spectroscopy after the aluminium filter and the monochromator is $\sim 8 \times 10^3$ photons/pulse compared to $\sim 10^7$ photons/pulse delivered by the HHG lightsource. Therefore, the integration time for the HHG-spectrum is raised to about 50 minutes in comparison to 10 seconds for the conventional He II spectrum. Nevertheless, these spectra show that the high harmonic light source is suitable for reasonable mapping of the electronic band structure of a surface.

Evident however, is an overall energy broadening of the photoemission features in the HHG spectrum in comparison to the He II spectrum. Due to the rather low HHG-light intensity after the monochromator, the broadening cannot be attributed to space-charge effects, as will be discussed in the following subsection. Therefore, the broadening only reflects the intrinsic bandwidth of the femtosecond HHG light pulses (time-bandwidth product for Gaussian-shaped and bandwidth-limited pulses ≈ 0.44). The achievable time-resolution of a time-resolved ARPES experiment will be discussed in the following subsection. Furthermore, it will be demonstrated that in comparison to the results obtained with the He II light source, the momentum resolution is not affected by the excitation with the HHG light.

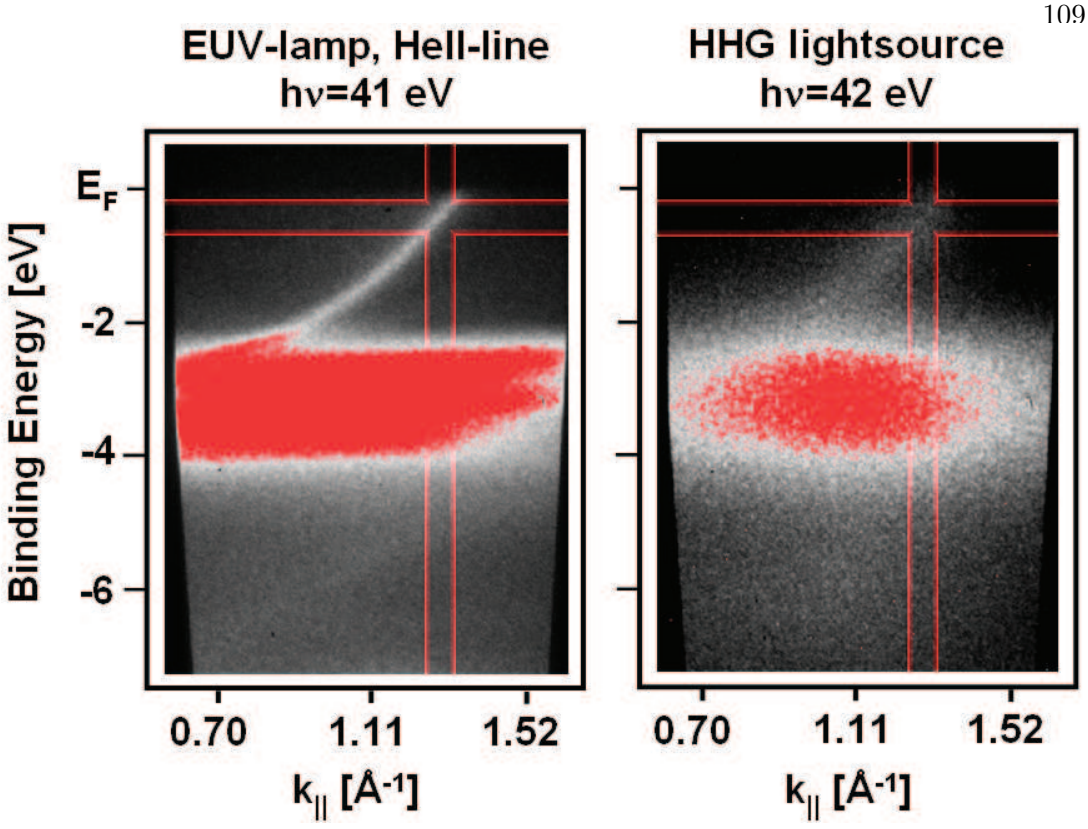

Figure 7.2: Photoemission maps of the Cu(111) *sp*-band at finite angle with (a) the He II line and (b) the HHG light source, after selecting the 27^{th} harmonic. The analyzer resolution was set to 200 meV. The HHG-spectrum is broadened due to the energy bandwidth of 801 ± 10 meV of the fs-HHG pulses. The red lines mark the integration areas for the energy and momentum distribution curves as shown in figures 7.3 and 7.4. Note that there are no harmonic sidebands observable.

7.1.4 Energy distribution curves

Energy distribution curves (EDC) from the He II data and the HHG data, as shown in figure 7.3a, have been derived from the PE-maps (figure 7.2) by a signal integration along $k_{\|}$, as indicated by the red marked area centred around $k_{\|} = 1.15$ Å^{-1}. Both *d*-bands and *sp*-bands are clearly resolved as peaks at about 3 eV binding energy and right at the Fermi-level, respectively. All spectral features, *d*-bands, *sp*-band peak, and Fermi edge, are strongly broadened in the HHG-spectrum in comparison to the He II spectrum.

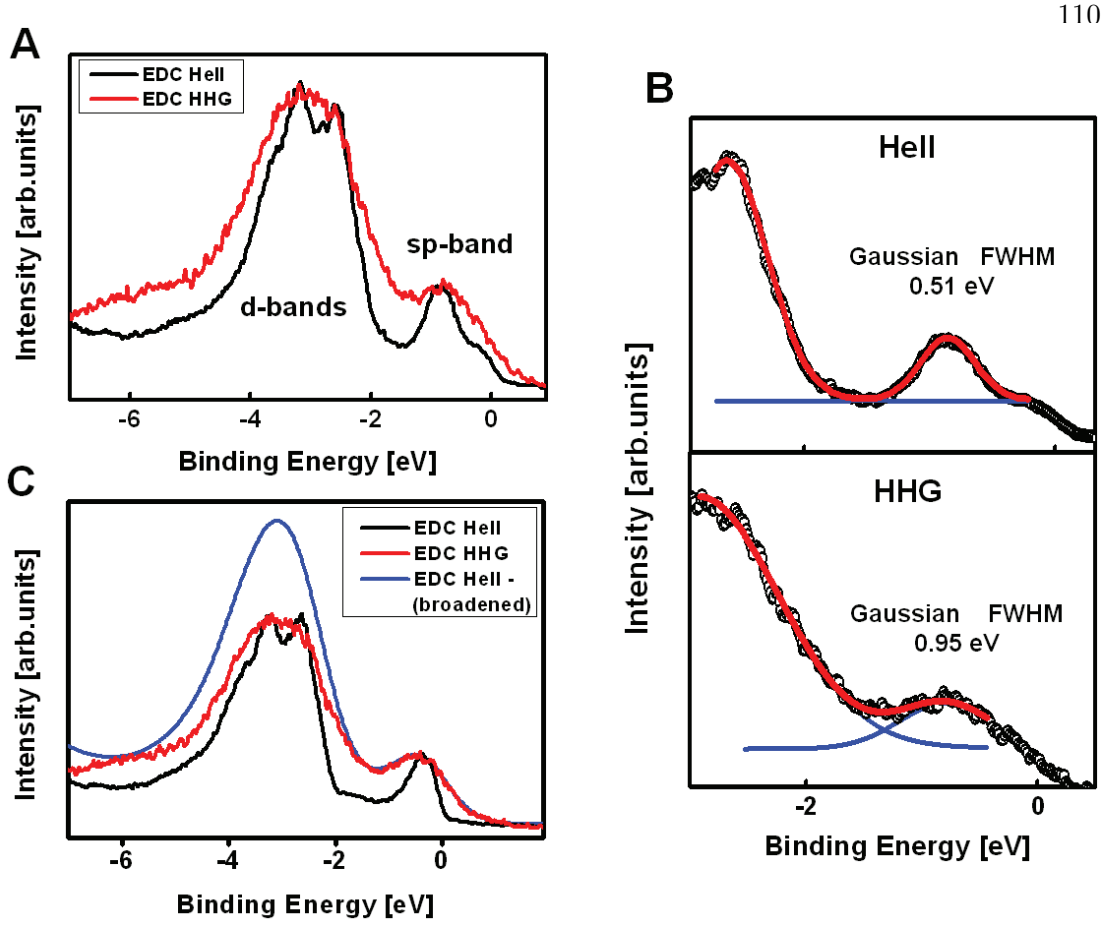

Figure 7.3: (a) Electron distribution curves EDC extracted from the photoemission maps in figure 7.2 ($k_{\|} = 1.15$ Å^{-1}). (b) Gaussian fits of the *sp*-band peak. The deconvolution of the Gaussian of the *sp*-band peak in the HHG-spectrum with the Gaussian linewidth of the *sp*-band peak in the He II spectrum gives a Gaussian bandwidth of 801 $\pm$ 10 meV for the HHG-light. (c) EDC extracted from the photoemission maps in figure 7.2 at a different $k_{\|}$ value ($k_{\|} = 1.25$ Å^{-1}). The blue EDC is derived by convoluting the original He II spectrum with a Gaussian of 801 meV to mimic the broadening due to the bandwidth of the HHG light.

With the use of a low-repetition, high-intensity light source for photoemission spectroscopy, one must be aware of space-charge effects leading to distortions in the photoemission spectrum. As a consequence of using pulsed radiation with high fluencies, the photomitted electrons leave the surface in short pulses with a fairly high electron density. Space-charge effects due to the Coulomb repulsion between the electrons within such a pulse distort the spectral distribution of these electrons and result

in a considerable loss in both energy resolution and angular resolution [35, 127]. The strength of these distortions is governed by the number of photoemitted electrons and the kinetic energy of the electrons.

A comparison of photoemission spectra recorded with different incident photon yields enables the quantification of space-charge effects. The number N of photoemitted electrons per pulse and area A in this experiment is about 2 orders of magnitude larger than in the experiments done with the monochromator (see figure 7.3). The difference (quadratic subtraction) of the width of the *d*-band feature in both spectra is, however, less than 500 meV. Based on this result, an upper value can be given for the space-charge broadening in the spectra recorded with the monochromator following the $\sqrt{N/\sqrt{A}}$ dependence, as given in reference [35]. This shows that the maximum contribution to the energy broadening for the experiments with a single harmonic is 56 meV. The quadratic addition of this value to the intrinsic linewidth of *d*-band and *sp*-band feature as deduced from the He II spectrum results in a line broadening of the peak FWHM well below 5 meV, a value that cannot be resolved with the analyzer settings (pass energy) used in the experiments.

The comparison of the *sp*-band peak width of the He II and the HHG spectrum can therefore be used to determine the bandwidth of the EUV-pulse. For both spectra, gaussian fits were performed to the *sp*-band peak and the corresponding peak FWHM (see figure 7.3b) was determined. Quadratic subtraction of the He II-spectrum FWHM from the HHG-spectrum FWHM gives the lower limit for the spectral bandwidth of the HHG radiation. This value is equal to the HHG bandwidth, since the contribution of the He II light linewidth to the spectral broadening of the EDC is negligible. For the He II *sp*-band peak, a FWHM of 0.51 eV was measured in comparison to 0.95 eV derived from the HHG-spectrum. This gives a bandwidth-value for the HHG radiation of 0.801 $\pm$ 10 eV. To verify the validity of this approach we convolved the He II EDC at a different $k_{\parallel}$ ($k_{\parallel} = 1.25$ Å^{-1}) with a Gaussian representing the HHG spectra distribution

with the derived bandwidth of 801 meV. A comparison of the resulting EDC with the corresponding HHG EDC is shown in figure 7.3c. The convolution result matches perfectly with the measured Fermi-edge distribution and the *sp*-band peak (blue line in (c)). The differences in the *d*-band peak between convolved EDC and the measured HHG-EDC can be assigned to the different polarizations of the two light sources used in the experiment (unpolarized for the discharge lamp and p-polarized for the HHG-light) due to polarization and state sensitive transition matrix elements.

The bandwidth of the EUV-HHG pulses of 801 $\pm$ 10 meV is capable of supporting a temporal pulse width of 3 fs. This value is the upper limit of time-resolution achievable in a pump-probe experiment using the described HHG beamline. Since there are no further dispersive elements in the beamline, it can be assumed (without measurement) that this pulse length is actually operative in our experiment. Using chirped or shaped laser pulses should further narrow the HHG bandwidth in the future [128].

7.1.5 Momentum distribution curves

Figure 7.4 shows the momentum distribution curves (MDCs) derived from the red-lined areas of figure 7.2 at an energy just below the Fermi-level. As was the case for the EDC, a clear broadening in comparison to the He II-MDC was observed. In the following, it will be shown that this broadening is related to the energy broadening of the PE-spectrum by the bandwidth of the HHG radiation and that the momentum resolution is not affected by the use of the femtosecond HHG pulse. Let us first consider the momentum spread in the PE spectrum due the momentum vector of the HHG-light itself. The total momentum added by the absorption of a 42 eV photon to an electron is about 0.02 Å^{-1}. The momentum spread delivered by the different frequency components contributing to the selected harmonic is consequently much smaller (0.0004 Å^{-1} for 801 meV bandwidth) and therefore cannot account for the observed broadening of the HHG-MDC.

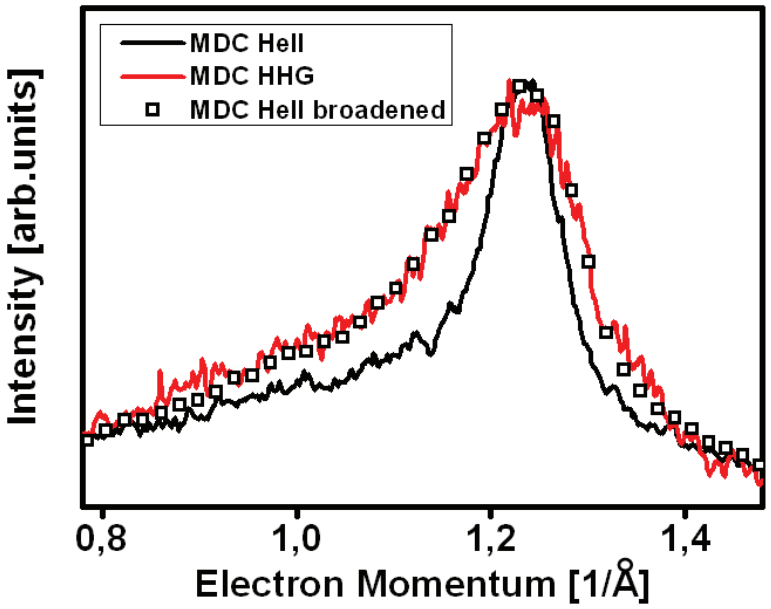

Figure 7.4: Momentum distribution curves (MDCs) extracted from the photoemission maps in figure 7.2. The MDC marked by open squares was derived after convoluting the He II EDCs with the HHG bandwidth of 801 meV for all different $k_{\|}$ values.

Another point to consider with respect to momentum resolution is the spot size of the EUV light at the surface, which determines the source diameter for photoemitted electrons. In our setup, the HHG-light is focused by the second mirror of the monochromator to a spot-size of about 100 μm to guarantee a high angular resolution. By comparison, the He II light is not focused onto the sample and exhibits a beam diameter of 600 μm. Therefore, the spot size cannot account for the broadening of the MDC trace, either. To check to what extent the spectral energy broadening due to the finite bandwidth of the HHG affects the MDC, the following convolution procedure was performed. EDCs for a series of $k_{\|}$ values measured with the He II lamp were convolved with a 801 meV Gaussian to again mimic the energy broadening of the HHG EDCs. From these EDC-series, we then extract a purely "energy broadened" MDC and compare this spectrum with the measured HHG-MDC (see figure 7.4). Evidently, the simulated and measured MDC agree almost perfectly. Therefore, it can be concluded

that the use of the HHG-light source does not degrade the momentum resolution of the ARPES experiment.

A detailed specification of the analyzer's momentum resolution using the He discharge lamp (beam diameter of 600 μm) shows an effective angle resolution of 0.6°, corresponding to a momentum resolution of 0.03 Å^{-1} at a kinetic energy of 36 eV. Due to the smaller HHG spot size in comparison to the He II light, we expect that the angular resolution in the HHG experiment even exceeds this value.

7.1.6 Conclusions

This section presented angle-resolved photoemission spectra recorded by excitation with femtosecond high harmonic light using a 2D imaging energy analyzer for parallel energy and momentum detection. The bandwidth of the transmitted EUV light is 801 ± 10 meV, and thus broad enough to support pulses as short as 3 fs. By these means, an angular resolution in the HHG photoemission experiment of better than $< 0.03\text{Å}^{-1}$ could be achieved. Yet, the relatively long integration times required to record a complete photoemission map are somewhat unsatisfactory. This constraint can, however, be overcome by some modifications to the experimental setup. Femtosecond amplifier systems with equivalent pulse specifications as the system used in this work but driven at repetition rates as high as 20 kHz are commercially available and will reduce typical measurement times by a factor of 20.

Finally, at the Kapteyn/Murnane group we have acquired a 2D imaging energy analyzer similar to the one described in this section, and will install it in the next few months. Besides reproducing these results, future prospects of time-resolved ARPES include studies of ultrafast processes of systems characterized by transient changes in the electronic structure $E(k)$. This may include, for instance, the ultrafast dynamics associated with highly correlated systems such as high-temperature superconductors, the interaction of adsorbates and surfaces, or the dynamics of phase transitions such as

laser-induced melting processes in conventional metals.

7.2 Chemisorbed System

As was shown in chapter 5, the dynamics of the excitation and decay of a core electron of an adsorbed atom or molecule are still poorly understood. The core-photoionization process is accompanied by vibrational or electronic excitation, charge-transfer from the substrate, and internal rearrangement. This process can leave the adsorbate-substrate complex in a variety of possible excited states immediately after ionization. The lifetime of these excited states compared to the lifetime of the core hole will dictate the nature of the radiationless decay spectra.

In chapter 5 a proof of principle experiment was performed to show that the core-hole lifetime of an adsorbate on a substrate can be directly measured. In the immediate future, we want to expand this study to more tightly bonded chemisorbed systems. In these systems, the stronger chemical bond (and hence enhanced charge-transfer) between substrate and adsorbate is known to influence the linewidth broadening compared with an isolated atom. The two systems that we are contemplating are Cs/Pt(111) [9] and CO/Pt(111) [10]. Cs adsorbed on Pt(111) (figure 7.5(a)) is the experimentally simplest system to study. In this case, we will use 91 eV photons to create a core hole and follow its dynamics through surface LAPE, just as we did with Xe/Pt(111). Carbon monoxide adsorbed onto Pt(111) (figure 7.5(b)) is an interesting system to study; however, it is experimentally harder. Two reasons why CO/Pt(111) is a more complex system to study are: 1) The photon energy necessary for the generation of a core hole is around 300eV, and 2) the estimated core-hole lifetime is about 1 - 2 fs, which means that in order to time-resolve this process we would need IR pulses shorter than 30 fs. This would require the use of self-phase modulation fibers to compress the IR pulse duration to < 10 fs.

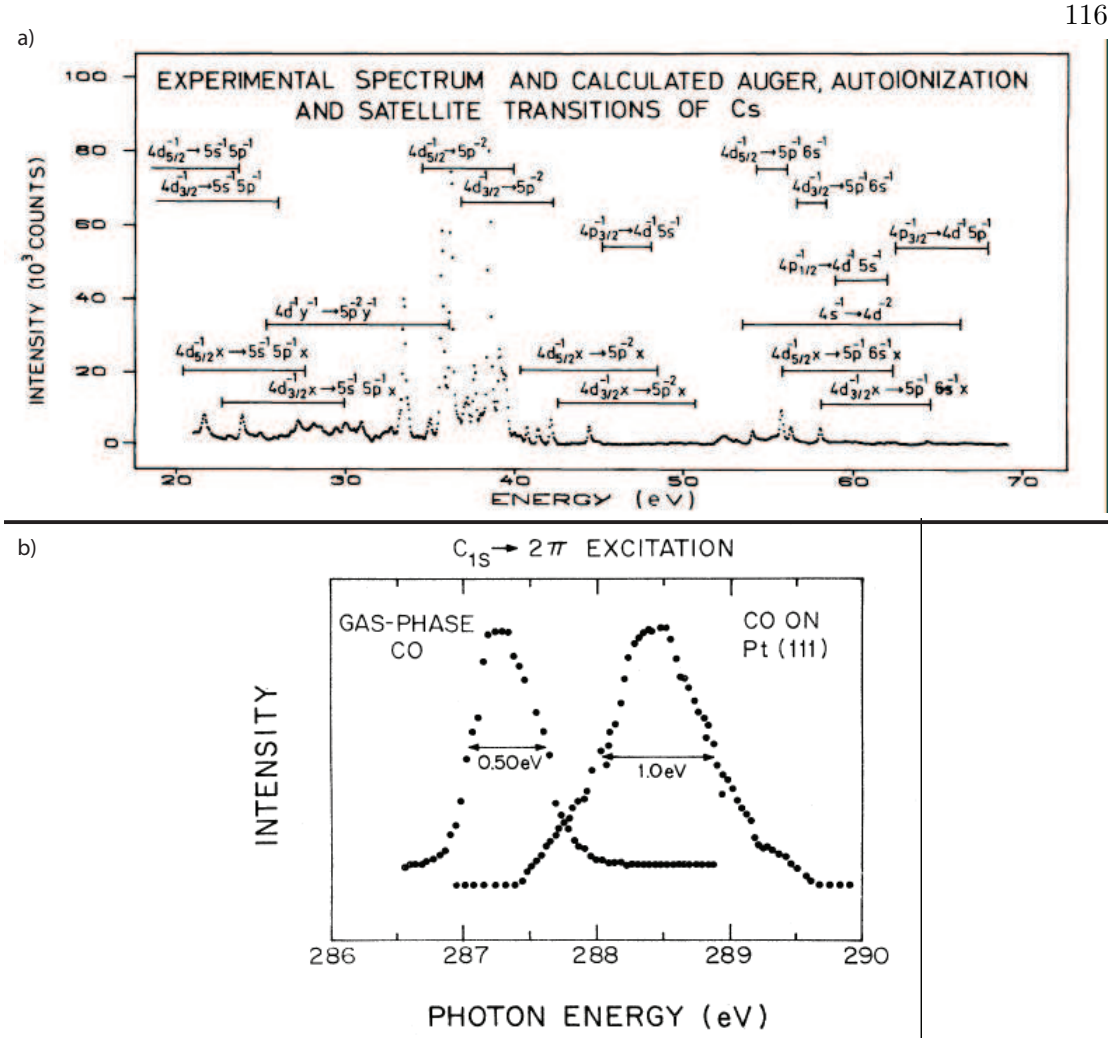

Figure 7.5: a) Experimental Auger-electron spectrum of atomic cesium after background substraction (from reference [9]). b) Photoabsorption spectra of the C $1s \rightarrow 2\pi$ transition for gas-phase CO and CO adsorbed on Pt(111) (from reference [10]).

7.3 Interatomic Coulombic Decay

The Interatomic Coulombic Decay (ICD) process with its underlying dynamics was theoretically predicted over a decade ago [112]. Recently, its occurrence was experimentally confirmed in large Ne clusters [129] as well as in Ne_2 [130]. The Interatomic Coulombic Decay is a fast decay process occurring via electron emission in loosely bound inner valence ionized atomic or molecular clusters. The mechanism that is the basis of

the ICD is an efficient energy transfer between neighboring monomers. The theoretical approach from Cederbaum predicts that after excitation the inner valence hole localized in one of the monomers is filled by an outer valence electron of the same monomer. The energy gained in this transition is transferred to a neighboring monomer, which uses it to emit one of its outer valence electrons (see figure 7.6). ICD is different from Auger decay since the electron does not emerge from the excited particle, but from its neighbor. Furthermore, this emission is not mediated by the overlap of the participating waves functions but rather by an energy transfer via a virtual photon.

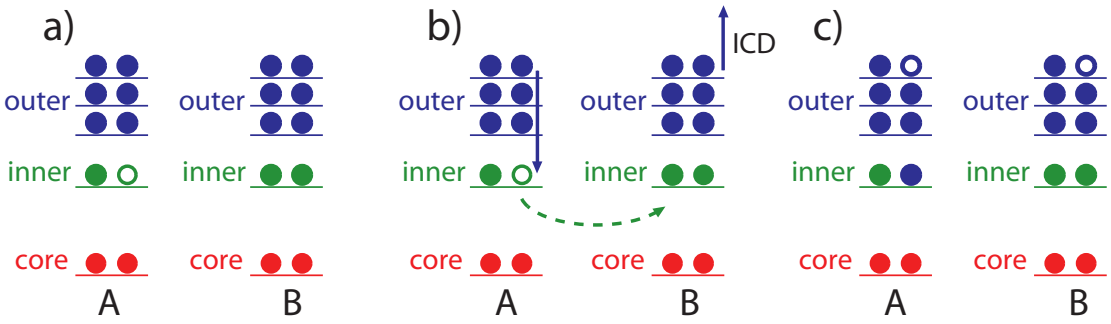

Figure 7.6: a) After excitation, the inner valence (inner) hole is localized in monomer A. b) Emission of an outer valence (outer) electron from monomer B after the transition of energy from the neighboring monomer A. c) Doubly ionized cluster with two outer valence holes localized in two different but neighboring monomers. Adapted from reference [11].

The efficiency of the energy transfer mechanism on which the ICD is based is strongly dependent on the nuclear distance between monomers, so that basically only neighboring monomers are involved in the process. In particular, if the monomers are very close to each other, the double ionization potential is too high and the ICD is energetically forbidden; if they are too far apart the energy transfer mechanism is not effective. Through energy domain measurements, the lifetime of the inner valence ionized state has been assumed to be on the order of a few to one hundred fs. Consequently, nuclear dynamics and electronic decay can occur on comparable time scales

and interplay significantly.

Because there is an interest in obtaining a value for the lifetime of the inner valence ionized state, we propose the time-resolved study of the electron dynamics involved in the interatomic Coulombic decay using laser-assisted photoemission. This experiment would be similar to the one presented in chapter 5, with the difference being we would have to dose Ne onto the Pt(111) surface. We would follow the temporal behavior of the sideband heights for the Pt *d*-band and the ICD electrons; thus, obtaining a value for the lifetime of the ICD process. However, this experiment presents certain difficulties: 1) In order to dose Ne onto the Pt(111) surface, we would need to cool down the sample to $\approx$ 14 °K, which is something that we cannot do at the moment. 2) The characteristic energies of the ICD electrons are a few eV, which means that in order to see the appearance of sidebands we would have to be careful that ATP does not mask the LAPE signal. As was demonstrated in chapter 6 by using longer-wavelength light the ATP signal can be reduced; thus, we might need to use IR wavelengths longer than 2000 μm. Although we have encountered the above mentioned difficulties, we have been working on the required changes to the experimental setup for the temporal study of ICD.

7.4 Double Auger Decay

As was discussed in chapter 5, deep inner shells are known to decay by cascade emission of Auger electrons, corresponding to transitions between successive inner-shell levels. The first accessible inner shell, on the other hand, is expected to decay by emission of a single Auger electron only. However, a weaker channel was discovered in noble gases, with emission of two electrons, known as the double Auger process [131]. Its interest lies in the strong electron correlation from which it originates. One important question concerns its dynamics: is it a direct double Auger process where both Auger electrons are emitted simultaneously, or is it a cascade process with subsequent emission

of electrons?

This question could be answered by studying the temporal evolution of the LAPE signal from the Auger and double Auger electrons. This experiment would be similar to the one presented in chapter 5, except that in this case we need to be concerned with the signal from the ATP electrons. The kinetic energy of the double Auger electrons is in the order of a few eV. Therefore, in order to study the dynamics of the double Auger decay we would have to combine our results from chapters 5 and 6. Current studies of this effect in Xe atoms suggest that the dominant path is a cascade process with a rapid (6 fs) ejection of a first Auger electron followed by the slower ($>$ 23 fs) emission of a second Auger electron [132].

Chapter 8

Conclusion

This thesis reports the first experimental observation of laser-assisted photoemission from a surface, its potential for the study of charge transfer in adsorbate-substrate systems, and a full comparison of surface LAPE with an atomic-based theoretical approach.

The observation of surface laser-assisted photoemission is significant for three reasons. First, it represents new physics - the extension of atomic dressed states to surface dressed states is not obvious, because of complex spatially-dependent laser electric fields present at the surface. Second, surface LAPE will make it possible to characterize lower-flux and higher-energy XUV pulses, since the target atoms are orders of magnitude more dense on a surface compared to a gas. Finally, surface LAPE has the potential to study ultrafast, femtosecond-to-attosecond time-scale electron dynamics in solids and in surface-adsorbate systems. This is in contrast with measurements to date in atomic systems, where dynamics are generally only homogeneously broadened and where time-domain studies have duplicated information that can be obtained from spectroscopic studies.

This work also presents the first direct time-resolved observation of the lifetime of core-excited states of an atom adsorbed onto a surface. The ability to directly measure the core-hole lifetime of an adsorbate on a substrate is of utmost importance for spectroscopic techniques such as core-hole clock spectroscopy, which use this value as a

reference for investigating fast electron relaxation dynamics. Our results demonstrate that time-resolved measurements that can identify the nature of any spectral broadening in more tightly bound systems, such as chemisorbed systems, are possible.

Furthermore, the results shown in this thesis agree with a simple atomic-based theoretical model. Surface LAPE can be distinguished from other laser-surface interaction phenomena, such as hot electron excitation, above-threshold photoemission, and space-charge acceleration. By using longer-wavelength IR pulses it has been possible to simultaneously increase the surface LAPE signal and suppress the undesirable processes of above-threshold photoemission, therefore enabling ultrafast studies of surface-adsorbate systems and attosecond electron dynamics over a wider energy range.

Bibliography

[1] M. Weinelt, "Time-resolved two-photon photoemission from metal surfaces," Journal of Physics: Condensed Matter, vol. 14, no. 43, pp. R1099–R1141, 2002.

[2] T. E. Glover, R. W. Schoenlein, A. H. Chin, and C. V. Shank, "Observation of laser assisted photoelectric effect and femtosecond high order harmonic radiation," Physical Review Letters, vol. 76, no. 14, pp. 2468–2471, 1996.

[3] M. Drescher, M. Hentschel, R. Kienberger, M. Uiberacker, V. Yakovlev, A. Scrinzi, T. Westerwalbesloh, U. Kleineberg, U. Heinzmann, and F. Krausz, "Time-resolved atomic inner-shell spectroscopy," Nature, vol. 419, pp. 803–807, 2002.

[4] M. Meyer, D. Cubaynes, P. O'Keeffe, H. Luna, P. Yeates, E. T. Kennedy, J. T. Costello, P. Orr, R. Taieb, A. Maquet, S. Dusterer, P. Radcliffe, H. Redlin, A. Azima, E. Plonjes, and J. Feldhaus, "Two-color photoionization in xuv free-electron and visible laser fields," Physical Review A (Atomic, Molecular, and Optical Physics), vol. 74, no. 1, p. 011401, 2006.

[5] H. C. Kapteyn, M. M. Murnane, and I. P. Christov, "Extreme nonlinear optics: Coherent x rays from lasers," Physics Today, vol. 58, no. 3, pp. 39–44, 2005.

[6] A. L. Lytle, "Phase matching and coherence of high-order harmonic generation in hollow waveguides," Ph.D. dissertation, University of Colorado, 2008.

[7] D. M. Gaudiosi, "High power ultrafast laser design and high-order harmonic generation in capillary discharge plasmas," Ph.D. dissertation, University of Colorado, 2007.

[8] M. Jurvansuu, A. Kivimki, and S. Aksela, "Inherent lifetime widths of ar 2p-1, kr 3d-1, xe 3d-1, and xe 4d-1 states," Physical Review A, vol. 64, no. 1, p. 12502, 2001.

[9] H. Aksela and S. Aksela, "Auger-electron spectrum of atomic cesium in the 15-75-ev energy range," Phys. Rev. A, vol. 28, no. 5, pp. 2851–2858, 1983.

[10] R. Murphy, E. W. Plummer, C. T. Chen, W. Eberhardt, and R. Carr, "Dynamics of adsorbate core-hole decay. ii. lifetimes," Physical Review B, vol. 39, no. 11, p. 7517, 1989.

[11] S. Scheit, H.-D. Meyer, and L. S. Cederbaum, "The interatomic coulombic decay in ne2," Journal of Physics: Conference Series, vol. 4, p. 277, 2005.

[12] M. P. Seah and W. A. Dench, "Quantitative electron spectroscopy of surfaces: A standard data base for electron inelastic mean free paths in solids," Surface and Interface Analysis, vol. 1, pp. 2–11, 1979.

[13] K. Giesen, F. Hage, F. J. Himpsel, H. J. Riess, and W. Steinmann, "Two-photon photoemission via image-potential states," Phys. Rev. Lett., vol. 55, no. 3, pp. 300–303, 1985.

[14] T. FAUSTER, "2-photon photoemission," PROGRESS IN SURFACE SCIENCE, vol. 46, no. 2-3, pp. 177–186, 1994.

[15] R. Yen, J. M. Liu, N. Bloembergen, T. K. Yee, J. G. Fujimoto, and M. M. Salour, "Picosecond laser interaction with metallic zirconium," Applied Physics Letters, vol. 40, no. 2, pp. 185–187, 1982.

[16] R. T. Williams, T. R. Royt, J. C. Rife, J. P. Long, and M. N. Kabler, "Picosecond time-resolved photoelectron spectroscopy of znte," Journal of Vacuum Science and Technology, vol. 21, no. 2, pp. 509–513, 1982.

[17] W. S. Fann, R. Storz, H. W. K. Tom, and J. Bokor, "Electron thermalization in gold," Phys. Rev. B, vol. 46, no. 20, pp. 13 592–13 595, 1992.

[18] C. A. Schmuttenmaer, M. Aeschlimann, H. E. Elsayed-Ali, R. J. D. Miller, D. A. Mantell, J. Cao, and Y. Gao, "Time-resolved two-photon photoemission from cu(100): Energy dependence of electron relaxation," Phys. Rev. B, vol. 50, no. 12, pp. 8957–8960, 1994.

[19] W. S. Fann, R. Storz, H. W. K. Tom, and J. Bokor, "Direct measurement of nonequilibrium electron-energy distributions in subpicosecond laser-heated gold films," Phys. Rev. Lett., vol. 68, no. 18, pp. 2834–2837, 1992.

[20] R. W. Schoenlein, J. G. Fujimoto, G. L. Eesley, and T. W. Capehart, "Femtosecond studies of image-potential dynamics in metals," Phys. Rev. Lett., vol. 61, no. 22, pp. 2596–2599, 1988.

[21] H. Petek, M. J. Weida, H. Nagano, and S. Ogawa, "Real-Time Observation of Adsorbate Atom Motion Above a Metal Surface," Science, vol. 288, no. 5470, pp. 1402–1404, 2000.

[22] A. G. Borisov, J. P. Gauyacq, A. K. Kazansky, E. V. Chulkov, V. M. Silkin, and P. M. Echenique, "Long-lived excited states at surfaces: $cs/cu(111)$ and $cs/cu(100)$ systems," Phys. Rev. Lett., vol. 86, no. 3, pp. 488–491, 2001.

[23] A. MCPHERSON, G. GIBSON, H. JARA, U. JOHANN, T. LUK, I. MCINTYRE, K. BOYER, and C. RHODES, "Studies of multiphoton production of vacuum ultraviolet-radiation in the rare-gases," JOURNAL OF THE OPTICAL SOCIETY OF AMERICA B-OPTICAL PHYSICS, vol. 4, no. 4, pp. 595–601, 1987.

[24] M. FERRAY, A. LHUILLIER, X. LI, L. LOMPRE, G. MAINFRAY, and C. MANUS, "Multiple-harmonic conversion of 1064-nm radiation in rare-gases," JOURNAL OF PHYSICS B-ATOMIC MOLECULAR AND OPTICAL PHYSICS, vol. 21, no. 3, pp. L31–L35, 1988.

[25] C. Spielmann, "Generation of coherent x-rays in the water window using 5-femtosecond laser pulses," Science, vol. 278, no. 5338, pp. 661–664, 1997.

[26] J. Zhou, J. Peatross, M. M. Murnane, H. C. Kapteyn, and I. P. Christov, "Enhanced high-harmonic generation using 25 fs laser pulses," Phys. Rev. Lett., vol. 76, no. 5, pp. 752–755, 1996.

[27] E. Seres, J. Seres, F. Krausz, and C. Spielmann, "Generation of coherent soft-x-ray radiation extending far beyond the titanium l edge," Phys. Rev. Lett., vol. 92, no. 16, p. 163002, 2004.

[28] J. Seres, E. Seres, A. Verhoef, G. Tempea, C. Strelill, P. Wobrauschek, V. Yakovlev, A. Scrinzi, C. Spielmann, and F. Krausz, "Source of coherent kilo-electronvolt x-rays," NATURE, vol. 433, no. 7026, p. 596, 2005.

[29] P. Paul, E. Toma, P. Breger, G. Mullot, F. Auge, P. Balcou, H. Muller, and P. Agostini, "Observation of a train of attosecond pulses from high harmonic generation," SCIENCE, vol. 292, no. 5522, pp. 1689–1692, 2001.

[30] M. Hentschel, R. Kienberger, C. Spielmann, G. Reider, N. Milosevic, T. Brabec, P. Corkum, U. Heinzmann, M. Drescher, and F. Krausz, "Attosecond metrology," NATURE, vol. 414, no. 6863, pp. 509–513, 2001.

[31] E. Goulielmakis, M. Schultze, M. Hofstetter, V. S. Yakovlev, J. Gagnon, M. Uiberacker, A. L. Aquila, E. M. Gullikson, D. T. Attwood, R. Kienberger, F. Krausz, and U. Kleineberg, "Single-cycle nonlinear optics," Science, vol. 320, no. 5883, pp. 1614–1617, 2008.

[32] R. HAIGHT and D. PEALE, "Tunable photoemission with harmonics of subpicosecond lasers," REVIEW OF SCIENTIFIC INSTRUMENTS, vol. 65, no. 6, pp. 1853–1857, 1994.

[33] F. Quere, S. Guizard, P. Martin, G. Petite, H. Merdji, B. Carré, J.-F. Hergott, and L. Le Déroff, "Hot-electron relaxation in quartz using high-order harmonics," Phys. Rev. B, vol. 61, no. 15, pp. 9883–9886, 2000.

[34] A. Rettenberger, P. Leiderer, M. Probst, and R. Haight, "Ultrafast electron transport in layered semiconductors studied with femtosecond-laser photoemission," Phys. Rev. B, vol. 56, no. 19, pp. 12 092–12 095, 1997.

[35] S. Passlack, S. Mathias, O. Andreyev, D. Mittnacht, M. Aeschlimann, and M. Bauer, "Space charge effects in photoemission with a low repetition, high intensity femtosecond laser source," Journal of Applied Physics, vol. 100, p. 024912, 2006.

[36] K. Read, H. Karlsson, M. Murnane, H. Kapteyn, and R. Haight, "Excitation dynamics of dye doped tris(8-hydroxy quinoline) aluminum films studied using time-resolved photoelectron spectroscopy," JOURNAL OF APPLIED PHYSICS, vol. 90, no. 1, pp. 294–300, 2001.

[37] M. Bauer, C. Lei, K. Read, R. Tobey, J. Gland, M. M. Murnane, and H. C. Kapteyn, "Direct observation of surface chemistry using ultrafast soft-x-ray pulses," Physical Review Letters, vol. 87, no. 2, p. 25501, 2001.

[38] C. Lei, M. Bauer, K. Read, R. Tobey, Y. Liu, T. Popmintchev, M. M. Murnane, and H. C. Kapteyn, "Hot-electron-driven charge transfer processes on $o2/pt(111)$ surface probed by ultrafast extreme-ultraviolet pulses," Phys. Rev. B, vol. 66, no. 24, p. 245420, 2002.

[39] R. I. Tobey, E. H. Gershgoren, M. E. Siemens, M. Murnane, H. Kapteyn, T. Feurer, and K. A. Nelson, Probing of thermal acoustic transients in materials using EUV radiation, in Ultrafast Phenomena XIV, edited by T. Kobayashi, T. Okada, T. Kobayashi, K. A. Nelson and S. D. Silvestri. Niigata, Japan: Springer-Verlag.

[40] L. Nugent-Glandorf, M. Scheer, D. Samuels, V. Bierbaum, and S. Leone, "Ultrafast photodissociation of br-2: Laser-generated high-harmonic soft x-ray probing of the transient photoelectron spectra and ionization cross sections," JOURNAL OF CHEMICAL PHYSICS, vol. 117, no. 13, pp. 6108–6116, 2002.

[41] E. Gagnon, P. Ranitovic, X.-M. Tong, C. L. Cocke, M. M. Murnane, H. C. Kapteyn, and A. S. Sandhu, "Soft x-ray-driven femtosecond molecular dynamics," SCIENCE, vol. 317, no. 5843, pp. 1374–1378, 2007.

[42] A. Weingartshofer, J. K. Holmes, G. Caudle, E. M. Clarke, and H. Krüger, "Direct observation of multiphoton processes in laser-induced free-free transitions," Phys. Rev. Lett., vol. 39, no. 5, pp. 269–270, 1977.

[43] J. M. Schins, P. Breger, P. Agostini, R. C. Constantinescu, H. G. Muller, G. Grillon, A. Antonetti, and A. Mysyrowicz, "Observation of laser-assisted auger decay in argon," Physical Review Letters, vol. 73, no. 16, pp. 2180–2183, 1994.

[44] M. M. Murnane, H. C. Kapteyn, and R. W. Falcone, "High-density plasmas produced by ultrafast laser pulses," Phys. Rev. Lett., vol. 62, no. 2, pp. 155–158, 1989.

[45] A. Baltuska, T. Udem, M. Uiberacker, M. Hentschel, E. Goulielmakis, H. R. Gohle Ch, V. S. Yakovlev, A. Scrinzi, T. W. Hansch, and F. Krausz, "Attosecond control of electronic processes by intense light fields," Nature, vol. 421, no. 6923, pp. 611–5, 2003.

[46] R. Kienberger, E. Goulielmakis, M. Uiberacker, A. Baltuska, V. Yakovlev, F. Bammer, A. Scrinzi, T. Westerwalbesloh, U. Kleineberg, and U. Heinzmann, "Atomic transient recorder," Nature, vol. 427, pp. 817–821, 2004.

[47] J. Itatani, F. Quéré, G. L. Yudin, M. Y. Ivanov, F. Krausz, and P. B. Corkum, "Attosecond streak camera," Phys. Rev. Lett., vol. 88, no. 17, p. 173903, 2002.

[48] T. Sekikawa, A. Kosuge, T. Kanai, and S. Watanabe, "Nonlinear optics in the extreme ultraviolet," NATURE, vol. 432, no. 7017, pp. 605–608, 2004.

[49] P. Tzallas, D. Charalambidis, N. Papadogiannis, K. Witte, and G. Tsakiris, "Direct observation of attosecond light bunching," NATURE, vol. 426, no. 6964, pp. 267–271, 2003.

[50] L. Miaja-Avila, C. Lei, M. Aeschlimann, J. L. Gland, M. M. Murnane, H. C. Kapteyn, and G. Saathoff, "Laser-assisted photoelectric effect from surfaces," Physical Review Letters, vol. 97, no. 11, p. 113604, 2006.

[51] A. L. Cavalieri, N. Muller, T. Uphues, V. S. Yakovlev, A. Baltuska, B. Horvath, B. Schmidt, L. Blumel, R. Holzwarth, and S. Hendel, "Attosecond spectroscopy in condensed matter," Nature, vol. 449, no. 7165, pp. 1029–32, 2007.

[52] A. Pietzsch, F. A, hlisch, M. Beye, M. Deppe, F. Hennies, M. Nagasono, E. Suljoti, W. Wurth, C. Gahl, D. K, brich, and A. Melnikov, "Towards time resolved core level photoelectron spectroscopy with femtosecond x-ray free-electron lasers," New Journal of Physics, no. 10, p. 033004, 2008.

[53] L. Miaja-Avila, G. Saathoff, S. Mathias, J. Yin, C. L. o vorakiat, M. Bauer, M. Aeschlimann, M. M. Murnane, and H. C. Kapteyn, "Direct measurement of core-level relaxation dynamics on a surface-adsorbate system," Physical Review Letters, vol. 101, p. 046101, 2008.

[54] S. Backus, C. Durfee, M. Murnane, and H. Kapteyn, "High power ultrafast lasers," REVIEW OF SCIENTIFIC INSTRUMENTS, vol. 69, no. 3, pp. 1207–1223, 1998.

[55] I. Walmsley, L. Waxer, and C. Dorrer, "The role of dispersion in ultrafast optics," REVIEW OF SCIENTIFIC INSTRUMENTS, vol. 72, no. 1, pp. 1–29, 2001.

[56] R. L. Sandberg, A. Paul, D. A. Raymondson, S. Haedrich, D. M. Gaudiosi, J. Holtsnider, R. I. Tobey, O. Cohen, M. M. Murnane, and H. C. Kapteyn, "Lensless diffractive imaging using tabletop coherent high-harmonic soft-x-ray beams," PHYSICAL REVIEW LETTERS, vol. 99, no. 9, 2007.

[57] R. Tobey, E. Gershgoren, M. Siemens, M. Murnane, H. Kapteyn, T. Feurer, and K. Nelson, "Nanoscale photothermal and photoacoustic transients probed with extreme ultraviolet radiation," APPLIED PHYSICS LETTERS, vol. 85, no. 4, pp. 564–566, 2004.

[58] K. C. Kulander, K. J. Schafer, and J. L. Krause, "Dynamics of short-pulse exicitation, ionization and harmonic conversion, in Super-Intense Laser-Atom Physics, B. Piraux, A. LHuillier, and K. Rzazewski, Eds. New York: Plenum.

[59] P. Corkum, "Plasma perspective on strong-field multiphoton ionization," Physical Review Letters, vol. 71, no. 13, pp. 1994–1997, 1993.

[60] L. KELDYSH, "Ionization in field of a strong electromagnetic wave," SOVIET PHYSICS JETP-USSR, vol. 20, no. 5, p. 1307, 1965.

[61] M. V. Ammosov, N. B. Delone, and V. P. Krainov, "Tunnel ionization of complex atoms and of atomic ions in an alternating electromagnetic field," Sov. Phys. JETP, vol. 64, no. 6, pp. 1191–1194, 1986.

[62] M. Lewenstein, P. Salières, and A. L'Huillier, "Phase of the atomic polarization in high-order harmonic generation," Phys. Rev. A, vol. 52, pp. 4747–4754, 1995.

[63] M. Bauer, "Femtosecond ultraviolet photoelectron spectroscopy of ultra-fast surface processes," Journal of Physics D: Applied Physics, vol. 38, no. 16, pp. R253–R267, 2005.

[64] T. Brabec and F. Krausz, "Intense few-cycle laser fields: Frontiers of nonlinear optics," Reviews of Modern Physics, vol. 72, no. 2, pp. 545–591, 2000.

[65] P. Balcou and A. L'Huillier, "Phase-matching effects in strong-field harmonic generation," Phys. Rev. A, vol. 47, no. 2, pp. 1447–1459, 1993.

[66] A. Rundquist, C. Durfee, Z. Chang, C. Herne, S. Backus, M. Murnane, and H. Kapteyn, "Phase-matched generation of coherent soft x-rays," SCIENCE, vol. 280, no. 5368, pp. 1412–1415, 1998.

[67] C. G. Durfee, A. R. Rundquist, S. Backus, C. Herne, M. M. Murnane, and H. C. Kapteyn, "Phase matching of high-order harmonics in hollow waveguides," Phys. Rev. Lett., vol. 83, no. 11, pp. 2187–2190, 1999.

[68] E. A. Gibson, A.Paul, N. Wagner, R. Tobey, D. Gaudiosi, S. Backus, I. P. Christov, A. Aquila, E. M. Gullikson, D. T. Attwood, M. M. Murnane, and H. C. Kapteyn, "Coherent soft x-ray generation in the water window with quasi-phase matching," Science, vol. 302, no. 5642, pp. 95–98, 2003.

[69] A. Paul, R. Bartels, R. Tobey, H. Green, S. Weiman, I. Christov, M. Murnane, H. Kapteyn, and S. Backus, "Quasi-phase-matched generation of coherent extreme-ultraviolet light," Nature, vol. 421, no. 6918, pp. 51–54, 2003.

[70] L. B. Madsen, "Strong-field approximation in laser-assisted dynamics," American Journal of Physics, vol. 73, p. 57, 2005.

[71] K. Rzazewski and K. Wdkiewicz, "Gauge-independent canonical formalism for nonrelativistic electrodynamics," Annals of Physics, vol. 130, pp. 1–13, 1980.

[72] L. B. Madsen, "Gauge invariance in the interaction between atoms and few-cycle laser pulses," Phys. Rev. A, vol. 65, no. 5, p. 053417, May 2002.

[73] D. Wolkov, "ber eine klasse von lsungen der diracschen gleichung," Z. Phys., vol. 94, pp. 250–260, 1935.

[74] H. R. Reiss, "Effect of an intense electromagnetic field on a weakly bound system," Phys. Rev. A, vol. 22, no. 5, pp. 1786–1813, 1980.

[75] M. R. Spiegel, Mathematical Handbook of Formulas and Tables. New York: McGraw-Hill.

[76] F. Ehlotzsky, A. Jaron, and J. Z. Kaminski, "Electron-atom collisions in a laser field," Phys Rep, vol. 297, pp. 63–153, 1998.

[77] C. J. Joachain, Quantum Collision Theory. Amsterdam: North-Holland/Elsevier, 1975.

[78] N. M. Kroll and K. M. Watson, "Charged-particle scattering in the presence of a strong electromagnetic wave," Phys. Rev. A, vol. 8, no. 2, pp. 804–809, Aug 1973.

[79] G. Cerullo and S. D. Silvestri, "Ultrafast optical parametric amplifiers," Review of Scientific Instruments, vol. 74, no. 1, pp. 1–18, 2003.

[80] D. Attwood, Soft X-Rays and Extreme Ultraviolet Radiation: Principles and Applications. New York: Cambridge University Press, 1999.

[81] A. Stolow, "Gigahertz bandwidth ultrahigh vacuum 50 omega coaxial high-voltage coupling capacitor for photoelectron spectroscopy," REVIEW OF SCIENTIFIC INSTRUMENTS, vol. 67, no. 5, pp. 1777–1780, 1996.

[82] P. Redhead, "Thermal desorption of gases," VACUUM, vol. 12, no. 4, pp. 203–211, 1962.

[83] G. Fowles, Introduction to Modern Optics. New York: Dover Publication, 1989.

[84] S. Tanuma, T. Shiratori, T. Kimura, K. Goto, S. Ichimura, and C. Powell, "Experimental determination of electron inelastic mean free paths in 13 elemental solids in the 50 to 5000 ev energy range by elastic-peak electron spectroscopy," SURFACE AND INTERFACE ANALYSIS, vol. 37, no. 11, pp. 833–845, 2005.

[85] B. FEUERBACHER and R. WILLIS, "Photoemission and electron states at clean surfaces," JOURNAL OF PHYSICS C-SOLID STATE PHYSICS, vol. 9, no. 2, pp. 169–216, 1976.

[86] R. HAYDOCK and M. KELLY, "Surface densities of states in tight-binding approximation," SURFACE SCIENCE, vol. 38, no. 1, pp. 139–148, 1973.

[87] A. Cionga, V. Florescu, A. Maquet, and R. Taïeb, "Target dressing effects in laser-assisted x-ray photoionization," Phys. Rev. A, vol. 47, no. 3, pp. 1830–1840, 1993.

[88] A. Mönnich, J. Lange, M. Bauer, M. Aeschlimann, I. A. Nechaev, V. P. Zhukov, P. M. Echenique, and E. V. Chulkov, "Experimental time-resolved photoemission and ab initio study of lifetimes of excited electrons in mo and rh," Physical Review B (Condensed Matter and Materials Physics), vol. 74, no. 3, p. 035102, 2006.

[89] J. E. Bayfield, L. D. Gardner, Y. Z. Gulkok, and S. D. Sharma, "Spectroscopic study of nonresonant photon absorption by highly excited hydrogen atoms in a strong microwave field," Phys. Rev. A, vol. 24, no. 1, pp. 138–143, 1981.

[90] H. R. Reiss, "Analytically simple dressing of bound-state wave functions," Phys. Rev. A, vol. 39, no. 5, pp. 2449–2455, 1989.

[91] N. Tzoar and J. I. Gersten, "Theory of electronic band structure in intense laser fields," Phys. Rev. B, vol. 12, no. 4, pp. 1132–1139, 1975.

[92] F. H. M. Faisal and J. Z. Kamiński, "Floquet-bloch theory of high-harmonic generation in periodic structures," Phys. Rev. A, vol. 56, no. 1, pp. 748–762, 1997.

[93] S. H. Autler and C. H. Townes, "Stark effect in rapidly varying fields," Phys. Rev., vol. 100, no. 2, pp. 703–722, 1955.

[94] G. LESCHIK, R. COURTHS, H. WERN, S. HUFNER, H. ECKARDT, and J. NOFFKE, "Band-structure of platinum from angle resolved photoemission experiments," SOLID STATE COMMUNICATIONS, vol. 52, no. 2, pp. 221–225, 1984.

[95] M. Aeschlimann, "Observation of surface enhanced multiphoton photoemission from metal surfaces in the short pulse limit," The Journal of Chemical Physics, vol. 102, no. 21, p. 8606, 1995.

[96] H. G. Muller, H. B. L. van den Heuvell, and M. J. van der Wiel, "Dressing of continuum states after mpi of xe in a two-colour experiment," Journal of physics. B. Atomic and molecular physics, vol. 19, no. 21, pp. L733–L739, 1986.

[97] G. Petite, P. Agostini, R. Trainham, E. Mevel, and P. Martin, "Origin of the high-energy electron emission from metals under laser irradiation," Physical Review B, vol. 45, no. 21, p. 12210, 1992.

[98] P. Siffalovic, M. Drescher, M. Spieweck, T. Wiesenthal, Y. C. Lim, R. Weidner, A. Elizarov, and U. Heinzmann, "Laser-based apparatus for extended ultraviolet femtosecond time-resolved photoemission spectroscopy," Review of Scientific Instruments, vol. 72, p. 30, 2001.

[99] G. Saathoff, L. Miaja-Avila, M. Aeschlimann, M. M. Murnane, and H. C. Kapteyn, "Laser-assisted photoemission from surfaces," Physical Review A, vol. 77, p. 022903, 2008.

[100] P. A. Brhwiler, O. Karis, and N. Mrtensson, "Charge-transfer dynamics studied using resonant core spectroscopies," Reviews of Modern Physics, vol. 74, no. 3, p. 703, 2002.

[101] T. Fauster and W. Steinmann, In Photonic Probes of Surfaces, ser. Electromagnetic Waves: Recent Developments in Research. Amsterdam: North-Holland, 1995, vol. 2.

[102] C. Keller, M. Stichler, G. Comelli, F. Esch, S. Lizzit, D. Menzel, and W. Wurth, "Femtosecond dynamics of adsorbate charge-transfer processes as probed by high-resolution core-level spectroscopy," Physical Review B, vol. 57, no. 19, pp. 11 951–11 954, 1998.

[103] A. Fhlisch, P. Feulner, F. Hennies, A. Fink, D. Menzel, D. Sanchez-Portal, P. M. Echenique, and W. Wurth, "Direct observation of electron dynamics in the attosecond domain," Nature, vol. 436, no. 7049, pp. 373–376, 2005.

[104] M. Wolf, "Femtosecond dynamics of electronic excitations at metal surfaces," Surface Science(Netherlands), vol. 377, pp. 343–349, 1997.

[105] M. Bauer, S. Pawlik, and M. Aeschlimann, "Femtosecond lifetime investigations of excited adsorbate states: atomic oxygen on cu (111)," Surf. Sci, vol. 377, p. 350354, 1997.

[106] L. Bartels, G. Meyer, K. H. Rieder, D. Velic, E. Knoesel, A. Hotzel, M. Wolf, and G. Ertl, "Dynamics of electron-induced manipulation of individual co molecules on cu(111)," Physical Review Letters, vol. 80, no. 9, p. 2004, 1998.

[107] M. Bauer, S. Pawlik, and M. Aeschlimann, "Resonance lifetime and energy of an excited cs state on cu(111)," Physical Review B, vol. 55, no. 15, p. 10040, 1997.

[108] A. Hotzel, K. Ishioka, E. Knoesel, M. Wolf, and G. Ertl, "Can we control lifetimes of electronic states at surfaces by adsorbate resonances?" Chemical Physics Letters, vol. 285, no. 3-4, pp. 271–277, 1998.

[109] G. Kaindl, T. C. Chiang, and T. Mandel, "Surface effects on energies of auger electrons from xe (111)," Physical Review B, vol. 28, no. 6, pp. 3612–3614, 1983.

[110] Z. Chang, A. Rundquist, H. Wang, M. M. Murnane, and H. C. Kapteyn, "Generation of coherent soft x rays at 2.7 nm using high harmonics," Physical Review Letters, vol. 79, no. 16, pp. 2967–2970, 1997.

[111] R. Trebino, Frequency-Resolved Optical Gating: The Measurement of Ultrashort Laser Pulses. Kluwer Academic Publishers, 2002.

[112] L. S. Cederbaum, J. Zobeley, and F. Tarantelli, "Giant intermolecular decay and fragmentation of clusters," Phys. Rev. Lett., vol. 79, no. 24, pp. 4778–4781, 1997.

[113] G. Ohrwall, M. Tchaplyguine, M. Lundwall, R. Feifel, H. Bergersen, T. Rander, A. Lindblad, J. Schulz, S. Peredkov, S. Barth, S. Marburger, U. Hergenhahn, S. Svensson, and O. Bjorneholm, "Femtosecond interatomic coulombic decay in free neon clusters: Large lifetime differences between surface and bulk," Physical Review Letters, vol. 93, no. 17, 2004, 173401.

[114] L. Miaja-Avila, J. Yin, S. Backus, G. Saathoff, M. Aeschlimann, M. M. Murnane, and H. C. Kapteyn, "Ultrafast studies of electronic processes at surfaces using the laser-assisted photoelectric effect with long-wavelength dressing light," Physical Review A (Atomic, Molecular, and Optical Physics), vol. 79, no. 3, p. 030901, 2009.

[115] J. P. Girardeau-Montaut and C. Girardeau-Montaut, "Theory of ultrashort nonlinear multiphoton photoelectric emission from metals," Physical Review B, vol. 51, no. 19, p. 13560, 1995.

[116] R. Daniele, G. Ferrante, E. Fiordilino, and S. Varro, "Photoelectric effect from a metal-surface - a revisited theoretical-model," Journal of the Optical Society of America B-Optical Physics, vol. 9, no. 10, pp. 1916–1921, 1992.

[117] S. Varro and F. Ehlotzky, "The multiphoton photo-effect and harmonic generation at metal surfaces," Journal of Physics D-Applied Physics, vol. 30, no. 22, pp. 3071–3078, 1997.

[118] F. Bisio, M. Nyvlt, J. Franta, H. Petek, and J. Kirschner, "Mechanisms of high-order perturbative photoemission from cu(001)," Physical Review Letters, vol. 96, no. 8, p. 087601, 2006.

[119] J. C. Baggesen and L. B. Madsen, "Theory for time-resolved measurements of laser-induced electron emission from metal surfaces," Physical Review A (Atomic, Molecular, and Optical Physics), vol. 78, no. 3, p. 032903, 2008.

[120] H. Steinruck, "Angle-resolved photoemission studies of adsorbed hydrocarbons," JOURNAL OF PHYSICS-CONDENSED MATTER, vol. 8, no. 36, pp. 6465–6509, 1996.

[121] A. Damascelli, Z. Hussain, and Z. Shen, "Angle-resolved photoemission studies of the cuprate superconductors," REVIEWS OF MODERN PHYSICS, vol. 75, no. 2, pp. 473–541, 2003.

[122] M. Bauer, C. Lei, R. Tobey, M. Murnane, and H. Kapteyn, "Time-resolved ups: a new experimental technique for the study of surface chemical reactions on femtosecond time-scales," SURFACE SCIENCE, vol. 532, pp. 1159–1165, 2003.

[123] G. Tsilimis, J. Kutzner, and H. Zacharias, "Photoemission study of clean and c(4 x 2)-2co-covered pt (111) using high-harmonic radiation," APPLIED PHYSICS A-MATERIALS SCIENCE & PROCESSING, vol. 76, no. 5, pp. 743–749, 2003.

[124] S. Mathias, L. Miaja-Avila, M. M. Murnane, H. Kapteyn, M. Aeschlimann, and M. Bauer, "Angle-resolved photoemission spectroscopy with a femtosecond high harmonic light source using a two-dimensional imaging electron analyzer," REVIEW OF SCIENTIFIC INSTRUMENTS, vol. 78, no. 8, p. 083105, 2007.

[125] T. Chiang, "Photoemission studies of quantum well states in thin films," SURFACE SCIENCE REPORTS, vol. 39, no. 7-8, pp. 181–235, 2000.

[126] S. Mathias, M. Wiesenmayer, M. Aeschlimann, and M. Bauer, "Quantum-well wave-function localization and the electron-phonon interaction in thin ag nanofilms," PHYSICAL REVIEW LETTERS, vol. 97, no. 23, p. 236809, 2006.

[127] X. Zhou, B. Wannberg, W. Yang, V. Brouet, Z. Sun, J. Douglas, D. Dessau, Z. Hussain, and Z. Shen, "Space charge effect and mirror charge effect in photoemission spectroscopy," JOURNAL OF ELECTRON SPECTROSCOPY AND RELATED PHENOMENA, vol. 142, no. 1, pp. 27–38, 2005.

[128] R. Bartels, S. Backus, I. Christov, H. Kapteyn, and M. Murnane, "Attosecond time-scale feedback control of coherent x-ray generation," CHEMICAL PHYSICS, vol. 267, no. 1-3, pp. 277–289, 2001.

[129] S. Marburger, O. Kugeler, U. Hergenhahn, and T. Möller, "Experimental evidence for interatomic coulombic decay in ne clusters," Phys. Rev. Lett., vol. 90, no. 20, p. 203401, 2003.

[130] T. Jahnke, A. Czasch, M. S. Schöffler, S. Schössler, A. Knapp, M. Käsz, J. Titze, C. Wimmer, K. Kreidi, R. E. Grisenti, A. Staudte, O. Jagutzki, U. Hergenhahn, H. Schmidt-Böcking, and R. Dörner, "Experimental observation of interatomic coulombic decay in neon dimers," Phys. Rev. Lett., vol. 93, no. 16, p. 163401, 2004.

[131] T. A. Carlson and M. O. Krause, "Experimental evidence for double electron emission in an auger process," Phys. Rev. Lett., vol. 14, no. 11, pp. 390–392, 1965.

[132] F. Penent, J. Palaudoux, P. Lablanquie, L. Andric, R. Feifel, and J. H. D. Eland, "Multielectron spectroscopy: The xenon $4d$ hole double auger decay," Phys. Rev. Lett., vol. 95, no. 8, p. 083002, 2005.

Appendix A

Laser-Assisted Dynamics

A.1 Ponderomotive Potential and Maximal Classical Excursion

The ponderomotive potential U_p is defined as the kinetic energy of an electron in the E field, averaged over an optical cycle. Using Newton's second law (in atomic units), $\boldsymbol{F} = \ddot{\boldsymbol{r}}$, where $\boldsymbol{F} = \boldsymbol{E}$, we can extract $\dot{\boldsymbol{r}}$ by

$$\dot{\boldsymbol{r}} = \int dt \boldsymbol{E}, \tag{A.1}$$

where the electric field E is given by

$$\boldsymbol{E} = -\frac{\partial}{\partial t}\boldsymbol{A}, \tag{A.2}$$

therefore,

$$\dot{\boldsymbol{r}} = -\boldsymbol{A} \tag{A.3}$$

Now we can calculate the averaged kinetic energy of the electron

$$
\begin{aligned}
\langle KE \rangle &= \left\langle \frac{1}{2}\dot{\boldsymbol{r}}^2 \right\rangle \\
&= \left\langle \frac{1}{2}\Big[-\boldsymbol{A}_0 \cos(\omega t - \boldsymbol{k}\cdot\boldsymbol{r})\Big]^2 \right\rangle \\
&= \left\langle \frac{1}{2} A_0^2 \cos^2(\omega t - \boldsymbol{k}\cdot\boldsymbol{r}) \right\rangle \\
&= \frac{1}{2} A_0^2 \left\langle \cos^2(\omega t - \boldsymbol{k}\cdot\boldsymbol{r}) \right\rangle \\
\langle KE \rangle &= \frac{A_0^2}{4} = \frac{E_0^2}{4\omega^2} = U_p \ . \qquad \text{(A.4)}
\end{aligned}
$$

From Newton's second law we can also obtain the maximal classical excursion $\boldsymbol{\alpha}_0$ of the electron in its oscillatory motion in the field. Starting from equation A.3

$$
\begin{aligned}
\dot{\boldsymbol{r}} &= -\boldsymbol{A} \\
\dot{\boldsymbol{r}} &= -\boldsymbol{A}_0 \int_0^t dt' \cos(\omega t' - \boldsymbol{k}\cdot\boldsymbol{r}) \\
\boldsymbol{r} &= -\frac{\boldsymbol{A}_0}{\omega} \sin(\omega t - \boldsymbol{k}\cdot\boldsymbol{r}),
\end{aligned}
\qquad \text{(A.5)}
$$

where the maximum value of $\sin(\omega t - \boldsymbol{k}\cdot\boldsymbol{r}) = 1$. Thus, the maximal classical excursion $\boldsymbol{\alpha}_0$ is

$$
\boldsymbol{\alpha}_0 = \frac{\boldsymbol{A}_0}{\omega} = -\frac{\boldsymbol{E}_0}{\omega^2} \ . \qquad \text{(A.6)}
$$

A.2 Volkov Wave Function

In this section we will derive the Volkov wave as a function of generalized Bessel functions. We will start from equation 2.20 and solve the integrals

$$
\psi_V(\boldsymbol{r}, t) = \frac{1}{(2\pi)^{3/2}} \exp i \left[\boldsymbol{q}\cdot\boldsymbol{r} - \int_0^t dt' \left(\frac{q^2}{2} + \boldsymbol{A}(t')\cdot\boldsymbol{q} + \frac{\boldsymbol{A}(t')^2}{2} \right) \right]. \qquad \text{(A.7)}
$$

First integral:

$$\int_0^t dt' \frac{q^2}{2} = \frac{q^2}{2} t. \tag{A.8}$$

Second integral:

$$\begin{aligned} \int_0^t dt' \, \boldsymbol{A}(t') \cdot \boldsymbol{q} &= \int_0^t dt' \boldsymbol{q} \cdot \boldsymbol{A}_0 \cos(\omega t') \\ &= \boldsymbol{q} \cdot \frac{\boldsymbol{A}_0}{\omega} \sin(\omega t) \\ &= \boldsymbol{q} \cdot \boldsymbol{\alpha}_0 \sin(\omega t). \end{aligned} \tag{A.9}$$

Third integral:

$$\begin{aligned} \int_0^t dt' \frac{\boldsymbol{A}(t')^2}{2} &= \int_0^t dt' \frac{A_0^2}{2} \cos^2(\omega t') \\ &= \frac{A_0^2}{2} \int_0^t dt' \cos^2(\omega t') \\ &= \frac{A_0^2}{4} \int_0^t dt' \Big[1 + \cos(2\omega t') \Big] \\ &= \frac{A_0^2}{4} \left(t + \frac{\sin(2\omega t)}{2\omega} \right) \\ &= U_p \left(t + \frac{\sin(2\omega t)}{2\omega} \right). \end{aligned} \tag{A.10}$$

By inserting the solved integrals A.8-A.10 into equation A.7, the Volkov wave function is given by

$$\psi_V(\boldsymbol{r}, t) = \frac{1}{(2\pi)^{3/2}} \exp i \left[\boldsymbol{q} \cdot \boldsymbol{r} - \boldsymbol{q} \cdot \boldsymbol{\alpha}_0 \sin(\omega t) - \frac{U_p}{2\omega} \sin(2\omega t) - \left(\frac{q^2}{2} + U_p \right) t \right], \tag{A.11}$$

which is the same as equation 2.23. We can now make use of equation 2.24 to rewrite the Volkov wave function in terms of generalized Bessel functions

$$\begin{aligned}
\psi_V(\boldsymbol{r},t) &= \frac{1}{(2\pi)^{3/2}} e^{i\boldsymbol{q}\cdot\boldsymbol{r}} \exp(-i)\left[\boldsymbol{q}\cdot\boldsymbol{\alpha}_0 \sin(\omega t) + \frac{U_p}{2\omega}\sin(2\omega t)\right] e^{-i\left(\frac{q^2}{2}+U_p\right)t} \\
&= \frac{1}{(2\pi)^{3/2}} e^{i\boldsymbol{q}\cdot\boldsymbol{r}} \sum_{n=-\infty}^{\infty} e^{-in\omega t} J_n\left(\boldsymbol{q}\cdot\boldsymbol{\alpha}_0, \frac{U_p}{2\omega}\right) e^{-i\left(\frac{q^2}{2}+U_p\right)t} \\
\psi_V(\boldsymbol{r},t) &= \frac{1}{(2\pi)^{3/2}} e^{i\boldsymbol{q}\cdot\boldsymbol{r}} \sum_{n=-\infty}^{\infty} e^{-i\left(\frac{q^2}{2}+U_p+n\omega\right)t} J_n\left(\boldsymbol{q}\cdot\boldsymbol{\alpha}_0, \frac{U_p}{2\omega}\right). \qquad \text{(A.12)}
\end{aligned}$$

A.3 S-Matrix Element in Laser-Assisted Scattering

Here we will derive the S-Matrix element in the case of laser-assisted scattering. If we substitute the initial and final Volkov wave functions of equation 2.25 into equation 2.29 we obtain

$$\begin{aligned}
(S-1)^B_{fi} &= -i\int_{-\infty}^{\infty} dt \langle \psi_V^{(f)} \mid V \mid \psi_V^{(i)} \rangle \\
&= -i\int_{\infty}^{\infty} dt \sum_{n,m} J_n\left(\boldsymbol{q}_f\cdot\boldsymbol{\alpha}_0, \frac{U_p}{2\omega}\right) J_m\left(\boldsymbol{q}_i\cdot\boldsymbol{\alpha}_0, \frac{U_p}{2\omega}\right) e^{i\left(\frac{q_f^2}{2}-\frac{q_i^2}{2}+(n-m)\omega\right)t} \\
&\quad \times \left\langle \frac{1}{(2\pi)^{3/2}} e^{i\boldsymbol{q}_f\cdot\boldsymbol{r}} \middle| V \middle| \frac{1}{(2\pi)^{3/2}} e^{i\boldsymbol{q}_i\cdot\boldsymbol{r}} \right\rangle. \qquad \text{(A.13)}
\end{aligned}$$

If we introduce the momentum transfer $\boldsymbol{q}_f = \boldsymbol{q}_i + Q$, the last factor of equation A.13 can be identified as the Fourier transform $\tilde{V}(\boldsymbol{Q})$ defined in equation 2.33:

$$\begin{aligned}
\tilde{V}(\boldsymbol{Q}) &= \left\langle \frac{1}{(2\pi)^{3/2}} e^{i\boldsymbol{q}_f\cdot\boldsymbol{r}} \middle| V \middle| \frac{1}{(2\pi)^{3/2}} e^{i\boldsymbol{q}_i\cdot\boldsymbol{r}} \right\rangle \\
&= \frac{1}{(2\pi)^3}\int d^3r V e^{i(\boldsymbol{q}_f-\boldsymbol{q}_i)\cdot\boldsymbol{r}} \\
\tilde{V}(\boldsymbol{Q}) &= \frac{1}{(2\pi)^3}\int d^3r V e^{i\boldsymbol{Q}\cdot\boldsymbol{r}}. \qquad \text{(A.14)}
\end{aligned}$$

Thus, the time integral in equation A.13 is readily evaluated

$$
\begin{aligned}
(S-1)^B_{fi} &= -i2\pi \sum_{n,m} \delta\left(\frac{q_f^2}{2} - \frac{q_i^2}{2} + (n-m)\omega\right) \\
&\quad \times J_n\left(\boldsymbol{q}_f \cdot \boldsymbol{\alpha}_0, \frac{U_p}{2\omega}\right) J_m\left(\boldsymbol{q}_i \cdot \boldsymbol{\alpha}_0, \frac{U_p}{2\omega}\right) \tilde{V}(\boldsymbol{Q}).
\end{aligned} \tag{A.15}
$$

We define the new summation index $\ell = m - n$, and equation A.15 reads

$$
\begin{aligned}
(S-1)^B_{fi} &= -i2\pi \sum_{n,\ell} \delta\left(\frac{q_f^2}{2} - \frac{q_i^2}{2} + \ell\omega\right) \\
&\quad \times J_n\left(\boldsymbol{q}_f \cdot \boldsymbol{\alpha}_0, \frac{U_p}{2\omega}\right) J_{\ell+n}\left(\boldsymbol{q}_i \cdot \boldsymbol{\alpha}_0, \frac{U_p}{2\omega}\right) \tilde{V}(\boldsymbol{Q}).
\end{aligned} \tag{A.16}
$$

The summation formula

$$
\sum_{k=-\infty}^{\infty} J_{n\mp k}(u,v) J_k(u',v') = J_n(u \pm u', v \pm v') \tag{A.17}
$$

may be applied to the product of generalized Bessel functions and the summation over n, and we obtain

$$
\begin{aligned}
(S-1)^B_{fi} &= -i2\pi \sum_{\ell} \delta\left(\frac{q_f^2}{2} - \frac{q_i^2}{2} + \ell\omega\right) J_\ell\left(\boldsymbol{\alpha}_0 \cdot \boldsymbol{q}_i - \boldsymbol{\alpha}_0 \cdot \boldsymbol{q}_f, \frac{U_p}{2\omega} - \frac{U_p}{2\omega}\right) \tilde{V}(\boldsymbol{Q}) \\
&= -i2\pi \sum_{\ell} \delta\left(\frac{q_f^2}{2} - \frac{q_i^2}{2} + \ell\omega\right) J_\ell\left(\boldsymbol{\alpha}_0 \cdot (\boldsymbol{q}_i - \boldsymbol{q}_f), 0\right) \tilde{V}(\boldsymbol{Q}) \\
(S-1)^B_{fi} &= -i2\pi \sum_{\ell} \delta\left(\frac{q_f^2}{2} - \frac{q_i^2}{2} + \ell\omega\right) J_\ell\left(-\boldsymbol{\alpha}_0 \cdot \boldsymbol{Q}\right) \tilde{V}(\boldsymbol{Q})
\end{aligned} \tag{A.18}
$$

where $J_n(u,0) = J_n(u)$ was used to relate the generalized Bessel function to the ordinary one.

Appendix B

Time-of-Flight Electron Analyzer

B.1 Electron Analyzer

When count rates are low, it is advantageous to try to detect every emitted electron within the energy range of interest. Using a pulsed photon source, the time-of-flight analyzer (TOF) can be employed (figure B.1), where in theory every single electron is counted.

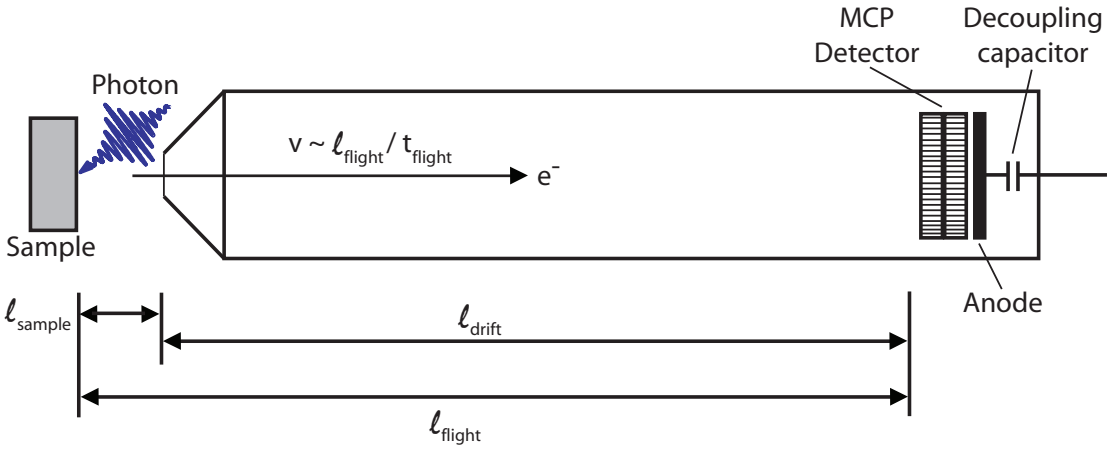

Figure B.1: Geometrical schematics of a Time-of-Flight (TOF) analyzer.

This is basically a stop watch technique triggered by a pulse from the light source and stopped when the photoelectron is detected after flying through a defined drift stretch. One of the limiting factors of such an analyzer is the restriction on the maximal count rate, since every single electron has to be registered and counted by the electronics.

The electronics have a certain dead time where they cannot register events.

B.2 Time to Energy Conversion

A time-of-flight analyzer physically measures the time of flight of a particle, i.e. electron, and not its energy E_{kin}. Therefore, the acquired data has to be normalized into an energy-dependent spectrum. The conversion from a time of flight distribution, to an energy-dependent spectrum is made by calculating the energy axis according to the kinetic energy. Here, each time bin t_i corresponds to a certain E_i width which varies in bin width according to a $1/t^2$ law (since $E_{\text{kin}} = m_e l^2/(2t^2)$). To obtain the number of events $N(E_i)$ per energy bin E_i as a function of the counts $N(t_i)$ in the corresponding time bin, the counts have to be renormalized (figure B.2).

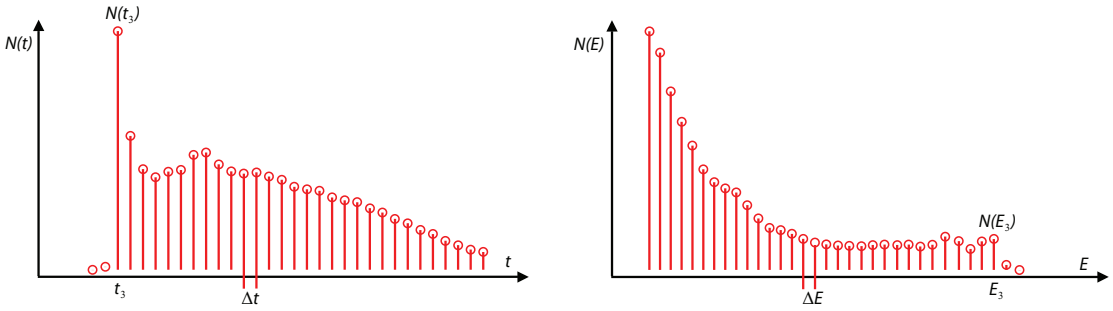

Figure B.2: Conversion from the acquired time of flight distribution $N(t)$ to an energy spectrum $N(E)$.

The total number of events, i.e. the surface under the spectral curves, is the same for the time and energy domain. For the counts N in every bin of width Δt or ΔE this is

$$\left| \sum_i N(t_i) \cdot \Delta t \right| = \left| \sum_i N(E_i) \cdot \Delta E \right| \tag{B.1}$$

and converting to infinitesimal notation,

$$\left| \int N(t) \cdot dt \right| = \left| \int N(E) \cdot dE \right|. \tag{B.2}$$

Differentiating both sides by dt,

$$N(t) = N(E) \cdot \left| \frac{dE}{dt} \right| = N(E) \cdot \frac{m_e}{e} \cdot \frac{l^2}{t^3} \tag{B.3}$$

gives a way to renormalize the counts $N(E_i)$ in every energy bin E_i

$$N(E_i^{kin}) = \frac{e}{m_e} \cdot \frac{t_i^3}{l^2} \cdot N(t_i) \tag{B.4}$$

with

$$E_i^{kin} = \frac{1}{2} \cdot \frac{m_e}{e} \cdot \frac{l^2}{t_i^2} \tag{B.5}$$

where

- $l = l_{drift} + l_{sample}$.
- $N(t_i)$: Measured counts in bin t_i.
- $N(E_i)$: Calculated number of counts in bin E_i.
- l: Total drift length of the electron.
- l_{drift}: Length of the TOF tube.
- l_{sample}: Distance from the sample to the entrance of the TOF.
- t_i: Time of flight of the electron over the drift stretch.
- $t_{stop-start}$: Elapsed time between the laser trigger and electron detection.
- $t_{optical\ start}$: Elapsed time between the laser trigger and the optical detection peak.

- m_e: Electron mass.
- e: Electron charge.

From equation B.5 it is clear that the bin width E_i^{kin} is not constant, but instead proportional to $-1/t^2$. This means that it decreases with an increase in flight time and binding energy.

The MCP detector can detect not only particles, but also photons. This is used to obtain the time zero (optical peak, see figure B.3) for calculating the time of flight t_i. The sensitivity of the MCP increases for shorter wavelengths, so that when using high order harmonics the optical back scattering from the harmonic beam on the sample is enough to induce a significant signal on the MCP. Thus, the time of flight t_i is the difference between the time evolved between the trigger and the detection $t_{stop-start}$ and the optical peak in the flight time spectrum $t_{optical\ start}$, which remains constant within an experiment:

$$t_i = t_{stop-start} - \left(t_{optical\ start} - \frac{l_{drift} + l_{sample}}{c} \right). \tag{B.6}$$

The last term in equation B.6 refers to the time correction due to the time elapsed between registering the optical peak at the MCO and its arrival at the sample surface. This time delay of a pulse traveling at the speed of light is in our case $\sim$ 2 ns and therefore virtually negligible compared with the electrons' flight time.

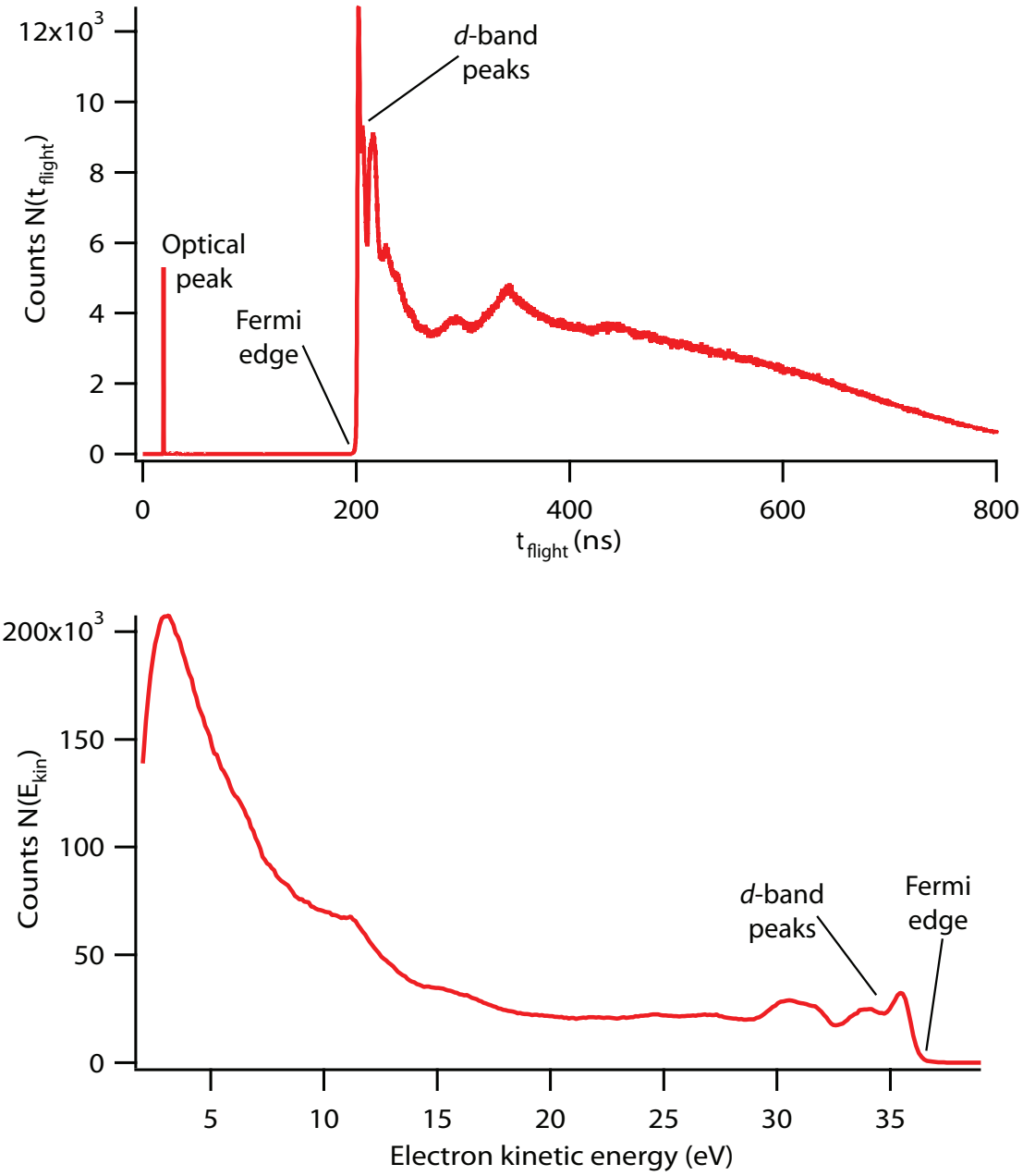

Figure B.3: Time of flight (top) to energy (bottom) conversion. The direct optical reflection of the sample induces the optical peak, which is used as time zero.